CHANGING GLACIERS IN THE BROOKS RANGE AND WESTERN CHUGACH MOUNTAINS, ALASKA: MASS LOSS, RUNOFF INCREASE, AND SUPRAGLACIAL VOLCANIC TEPHRA COVERAGE

By

Jason Geck, B.A., M.S.

A Dissertation Submitted in Partial Fulfillment of the Requirements

for the Degree of

Doctor of Philosophy

in

Geology

University of Alaska Fairbanks

December 2020

APPROVED:

Dr. Regine Hock, Committee Chair
Dr. Bernard Coakley, Committee Member
Dr. Roman Dial, Committee Member
Dr. Michael Loso, Committee Member
Dr. Paul McCarthy, Chair
Department of Geosciences
Dr. Kinchel Doerner, Dean
College of Natural Science and Mathematics
Dr. Richard Collins,
Director of the Graduate School

Abstract

Glaciers in Alaska cover over ~87,000 km^2 (~ 6 % of the state) with most glaciers thinning and retreating at an increasing rate. The thinning and retreating of glaciers worldwide can have an immediate socio-economic implication in addition to the longer-term glacier meltwater contribution to sea level rise. This dissertation investigated Alaskan glaciers in the Brooks Range for mass loss and area reductions over the period 1970–2001 (Chapter 2), historic mass balance and runoff for Eklutna Glacier, located in western Chugach Mountains, using a temperature index model over 1984-2019 period (Chapter 3), and the persistence of tephra from a volcanic eruption of Mt. Spurr in 1992 on seven western Chugach Mountain glaciers (Chapter 4).

Glaciers in the Brooks Range in Arctic Alaska (> 68° N) are important indicators of climate change and provide information on long-term climate variations in an area that has few high elevation meteorological stations. Digital elevation models (DEMs) reconstructed from topographic maps were differenced from an interferometric synthetic aperture radar DEM to calculate the volume and mass changes of 107 glaciers (42 km^2). Over the period 1970–2001, total ice volume loss was 0.69 ± 0.06 km^3 corresponding to a mean (area-weighted) specific mass balance rate of -0.54 ± 0.05 m w.e. a^{-1} (± uncertainty). The arithmetic mean of all glaciers' specific mass balance rates was -0.47 ± 0.27 m w.e. a^{-1} (± 1 std. dev.). A subsample of 36 glaciers found a 26 ± 16 % mean area reduction over ~35 years.

Alaska's largest city, Anchorage, is critically dependent upon the melt water of Eklutna Glacier (29 km^2) for both drinking water and hydropower generation; however, the glacier is rapidly retreating. We used a temperature index model to reconstruct the

glacier's mass balance for the period 1985-2019 and quantify the impacts of glacier change on runoff. Eklutna Glacier experienced a significant annual mean surface mass balance negative trend (-0.38 m w.e. decade^{-1}). Mean annual cumulative melt increased by 24 % between the 1985-93 and 2011-19 period. Additionally, the day of the year when 95 % of annual melt has occurred was eight days later in the later time period than in the earlier period, demonstrating a prolongation of the melt season. The modeled mean annual discharge increased at a rate of 0.2 m decade^{-1}. This indicates that peak water, i.e. the year when annual discharge starts decreasing as the glacier becomes smaller, has not been reached. The past increases in runoff quantity and melt season length provide opportunities for water resource managers that must be balanced against future decreased runoff as the glacier continues to shrink.

Volcanic eruptions deposit volcanic tephra on glaciers in Alaska, modifying surface albedo and glacier melt. We mapped the distribution of tephra originating from the eruption of Mt. Spurr in 1992 using aerial photos and satellite imagery on seven glaciers located approximately 180 km east of the volcano in western Chugach Mountains in southcentral Alaska. The glaciers were completely covered with ≥ 500 g m^{-2} tephra immediately after the event. Tephra deposits are still visible on all glaciers 26 years after the eruption. Using LandSat 8 surface reflectance bands, we quantified percentages of tephra glacier coverage. Results suggest an increasing tephra extent on five of the seven investigated glaciers over 2013-2018 period explained by firn line retreat. The mean percent increase for all glaciers was 4 % with Troublesome Glacier showing greatest increase (~ 7 %) and Finch Glacier showing a slight decrease (~ 1 %).

This long-term tephra persistence on glacier surfaces most likely enhanced melt although the precise effect remains unknown.

Table of Contents **Page**

List of Figures **Page**

List of Tables **Page**

Acknowledgements

I am thankful to my committee members, who share the common trait among them as hardworking, productive scientists. I am proud to call both colleagues and friends. Dr. Regine Hock 'adopted' me as an orphan graduate student many years ago. She always enthusiastically encouraged my progress, as I slowly prodded along my path. Her leaving UAF to return to Europe was a blessing in disguise as it forced me to complete my dissertation. Dr. Roman Dial acted as a mentor to me ever since my moving to Alaska over 24 years ago as my advisor for a master's degree at Alaska Pacific University. He taught me everything from adventurous travel to pack rafting in the back country to statistics, scientific writing, coding, in the front country. Dr. Michael Loso has always been an encouraging mentor and assisted me greatly through this whole process. I thank him for establishing the Eklutna Glacier Monitoring Program and passing the project on to me. Dr. Bernard Coakley supported my efforts even before joining my committee, I am thankful for all his assistance and advice along this path. I am thankful to Dr. Matt Nolan for taking a chance on me as a PhD student and for all he taught me about glaciers, expedition planning, and scientific field work.

I am thankful to the many administrations at Alaska Pacific University who supported my degree completion with sabbaticals and leave of absences requests granted. I am also extremely thankful to my friends (especially Emily Creely), fellow UAF graduate students, and past APU students for their support and patience. I am thankful to my parents, Jack and Joy Geck, who always encouraged my education from a Bachelor of Art, Master of Science, and a PhD. Your support both emotional and financial allowed my completion of all these educational goals.

Lastly, I am forever thankful to my wife, Joey Williams who tolerated my absence for field work and always accommodated my time to work on my dissertation. She is the love of my life. I am thankful to my kids, Tucker and Willa Geck, who served as daily motivation to complete this degree. Thanks to all those who are not mentioned here but helped out in small ways to allow me to reach this long-held goal of mine.

Chapter 1 Introduction

Alaska's temperatures are rising twice as fast as the global average (Gray and others, 2018) with direct impacts to both sea level rise and ocean currents (Hock and others, 2019; O'Neel and others, 2015) due to glacier wastage. Glaciers in Alaska cover over ~87,000 km^2 (~ 6 %) with most currently thinning and retreating (Hock and others, 2019). Zemp and others, (2019) found a -0.85 ± 0.19 m w.e. yr^{-1} specific mass change for Alaska glaciers over the period 2006-2016. Glaciers contribute significantly to runoff and water resources, including hydropower and water supplies. Alaska receives ~21 % of electrical production from hydroelectric projects, mostly fed by glacierized watersheds (US EIA, 2020). Presence of glaciers within a watershed influence both annual runoff totals and their seasonal distribution. These effects include 1) an increased contribution of melt water with negative glacier mass balance, 2) maximum melt water input in summer, 3) presence of diurnal fluctuations, and 4) a dampening of annual streamflow variation (Hock and others, 2005). A warming climate leads to a prolonged melt season where the seasonal runoff is concentrated within a shorter time span (Hock and Jansson, 2005).

This dissertation presents three topics organized as individual chapters: 1) determination of volume change of central Brooks Range glaciers, 2) temperature index modelling to calculate historic mass balance and runoff of Eklutna Glacier in the Chugach Mountains and 3) investigation of tephra persistence on western Chugach glaciers from the 1992 Mt. Spurr volcanic event. Background is provided on general methods involved for each topic, as well as the scientific objectives addressed.

A glacier's annual mass balance is the difference between mass gains by accumulation and mass loss, most importantly through melt over the course of one year. Various methods exist to monitor glacier mass change over time. These include direct in-situ observations and remote sensing methods (Kääb, 2005; Kaser and others, 2003). Mass balance calculations may occur via the glaciological or geodetic method (Cogley and others, 2011). The glaciological method measures surface mass balance using observations of accumulation through snow pits that record density depth profiles and ablation as measured by stakes embedded in the ice. These measures are then extrapolated across the entire glacier. The geodetic method measures glacier surface elevation differences over time and the volume change is converted to mass change using a suitable mean density.

Chapter 2

The most common geodetic technique differences digital elevation models (DEMs) over time. Historic DEMs are constructed by interpolating topographic maps drawn from aerial photography. Newer DEMs are constructed directly from lidar or structure from motion computational photogrammetry. The technique of calculating glacier mass balance change using topographic models is commonly referred as DEM differencing (Kääb, 2005).

Chapter 2 was published in the *Arctic, Antarctic, Alpine Research*[1], and determined the volume and mass change between 1970 and 2001 for ~100 small valley and cirque glaciers in the central Brooks Range, Arctic Alaska. The objectives included:

- Determining the glacier volume changes using DEMs derived from United States Geological Survey (USGS) topographic maps and airborne interferometric synthetic aperture radar (IfSAR).
- Exploring the effect of mis-registration of DEMs using multiple co-registration methods.
- Updating the original USGS 1970/1973 glacier outlines using optical satellite imagery (Quickbird) to determine area change rates.
- Examining the dependence of small glacier response to topography during climatic change based on topographic and geometric indices.

Chapter 3

Mass balance models are a key component of modeling glacier hydrology. Mass balance models vary in degree of complexity based on necessary input data. These vary from detailed energy-balance to simple temperature-index models (Hock and Jansson, 2005). Energy-balance models require data for air temperature, humidity, wind speed, and radiation. Temperature index models are based solely on air temperature and the proportional relationship of temperatures to melting (Ohmura, 2001). Only temperature and precipitation data are needed for temperature-index based mass balance modeling efforts.

[1] Geck, J., R. Hock & M. Nolan (2013) Geodetic Mass Balance of Glaciers in the Central Brooks Range, Alaska, U.S.A., from 1970 to 2001, Arctic, Antarctic, and Alpine Research, 45:1, 29-38, DOI: 10.1657/1938-4246-45.1.29

Chapter 3, which was submitted for publication to the *Journal of Glaciology*, is based on an enhanced temperature-index model used to hindcast mass balance and runoff over 1984-2019 period. The objectives for this paper included:

- Parameterizing a temperature index model with observations from 2011-15 combining in-situ mass-balance measurements and observed snow lines from satellite imagery.
- Reconstructing the glacier's mass balance and discharge over the period 1985–2019.
- Quantifying the impacts of glacier change on runoff patterns.

Chapter 4

Alaska's glaciers are subject to volcanic events that deposit tephra on their surfaces, potentially changing their albedo, impacting surface energy balance. Worden and others' (2018) historical tephra deposition maps show the greatest number of events over the western Chugach Mountains, including five specific documented events of the past 60 years. Depending on the thickness of tephra deposition, melt may be enhanced, potentially increasing glacier mass wastage, or, with thicker deposition, snow/ice surfaces may be insulated reducing melt. Field experiments on glacier surfaces have found maximum glacier melt occurs with a 1-3.5 mm layer of tephra (Dragosics and others, 2016), which--depending on the density of tephra--is equivalent to about 1-3.5 kg m^{-2}. Mt. Spurr located 125 km west of Anchorage, Alaska, erupted from 27 June to 17 September 1992. An 18 August 1992 event deposited 0.5-1.0 kg m^{-2} of tephra on multiple glacier surfaces in the Western Chugach Mountains (McGimsey and others, 2001). Chapter 4 examines these tephra deposits on seven western

Chugach Mountain glaciers using remote sensing methods. The objectives for this paper included:

- Investigating the temporal evolution of tephra deposits at the glacier surfaces.
- Mapping the end-of-summer extent of tephra exposed at the glacier surfaces between initial deposition on 19 August 1992 and 2018 using aerial photos and satellite imagery.
- Using LandSat 8 surface reflectance bands to quantify tephra presence.

References

Administration USEI (2020) Alaska Net Energy Production. https://www.eia.gov/state/?sid=AK#tabs-4

Cogley, J.G., R. Hock, L.A. Rasmussen, A.A. Arendt, A. Bauder, R.J. Braithwaite, P. Jansson, G. Kaser, M. Möller LN and MZ (2011) Glossary of Glacier Mass Balance and Related Terms. *IHP-VII Tech. Doc. Hydrol.* **No. 86**(IACS Contribution No. 2,) https://wgms.ch/downloads/Cogley_etal_2011.pdf

Dragosics M, Meinander O, Jónsdóttír T, Dürig T, De Leeuw G, Pálsson F, Dagsson-Waldhauserová P and Thorsteinsson T (2016) Insulation effects of Icelandic dust and volcanic ash on snow and ice. *Arab. J. Geosci.* **9**(2), 1–10 (doi:10.1007/s12517-015-2224-6)

Gaudard L, Gilli M and Romerio F (2013) Climate Change Impacts on Hydropower Management. *Water Resour. Manag.* **27**(15), 5143–5156 (doi:10.1007/s11269-013-0458-1)

Gray ST, Berman M, Eerkes-medrano L, Hennessy T, Huntington HP, Littell J, Mccammon M, Trainor S and Herrmann V (2018) Technical Contributors are listed at the end of the chapter. **II**, 1185–1241 (doi:10.7930/NCA4.2018.CH26)

Hock, R., G. Rasul, C. Adler, B. Cáceres, S. Gruber, Y. Hirabayashi, M. Jackson, A. Kääb, S. Kang, S. Kutuzov, Al. Milner, U. Molau, S. Morin, B. Orlove, and H. Steltzer 2019 (2019) High Mountain Areas. In: IPCC Special Report on the Ocean and Cryosphere in a Changing Climate. *Press.* **4**(vii, 973), 7–22 (doi:http://www.ipcc.ch/publications_and_data/ar4/wg2/en/spm.html)

Hock R and Jansson P (2005) Modelling Glacier Hydrology. *Encyclopedia of Hydrological Sciences*, 2647–2655

Hock R, Jansson P and Braun LN (2005) Modelling the Response of Mountain Glacier Discharge to Climate Warming. (Ipcc 2001), 243–252 (doi:10.1007/1-4020-3508-x_25)

Kääb A (2005) *Remote Sensing of Mountain Glaciers and Permafrost Creep.* http://scholar.google.com/scholar?hl=en&btnG=Search&q=intitle:Remote+Sensing+of+Mountain+Glaciers+and+Permafrost+Creep#0

Kaser G, Fountain AG and Jansson P (2003) A Manual for monitoring the mass balance of mountain glaciers with particular attention to low latitude characteristics; Technical documents in hydrology. *IHPVI Tech. Doc. Hydrol.* **2003**(59), 1–137 papers2://publication/uuid/C48874AD-97E5-4178-BEF3-E35CD400C043

Mauro B Di, Fava F, Ferrero L, Garzonio R, Baccolo G, Delmonte B and Colombo R (2015) Journal of geophysical research. *Nature* **175**(4449), 238 (doi:10.1038/175238c0)

McGimsey RG, Neal CA and Riley CM (2001) Areal distribution, thickness, mass, volume, and grain size of tephra-fall deposits from the 1992 eruptions of Crater Peak vent, Mt. Spurr Volcano, Alaska. *USGS Open-File Rep. 01–370*

O'Neel S, Hood E, Bidlack AL, Fleming SW, Arimitsu ML, Arendt A, Burgess E, Sergeant CJ, Beaudreau AH, Timm K, Hayward GD, Reynolds JH and Pyare S (2015) Icefield-to-ocean linkages across the northern pacific coastal temperate rainforest ecosystem. *Bioscience* **65**(5), 499–512 (doi:10.1093/biosci/biv027)

Ohmura A (2001) Physical basis for the temperature-based melt-index method. *J. Appl. Meteorol.* **40**(4), 753–761 (doi:10.1175/1520-0450(2001)040<0753:PBFTTB>2.0.CO;2)

Worden, A.K., Schaefer, J.R., and Mulliken KM (2018) ephra occurrence in Alaska: a map-based compilation of stratigraphic tephra data: Alaska Division of Geological & Geophysical Surveys Miscellaneous Publication 165. (doi:http://doi.org/10.14509/30059)

Zemp M, Huss M, Thibert E, Eckert N, McNabb R, Huber J, Barandun M, Machguth H, Nussbaumer SU, Gärtner-Roer I, Thomson L, Paul F, Maussion F, Kutuzov S and Cogley JG (2019) Global glacier mass changes and their contributions to sea-level rise from 1961 to 2016. *Nature* **568**(7752), 382–386 (doi:10.1038/s41586-019-1071-0)

Chapter 2 Geodetic Mass Balance of Glaciers in the Central Brooks Range, Alaska, U.S.A., from 1970 to 2001[1]

2.1 Abstract

Alaska's arctic glaciers have retreated and thinned during recent decades, and glaciers in the central Brooks Range are no exception. Digital elevation models (DEMs) reconstructed from topographic maps (from 1970 and 1973) were differenced from a 2001 interferometric synthetic aperture radar DEM to calculate the volume and mass changes of 107 glaciers covering 42 km^2 (1970/1973) in the central Brooks Range, Alaska, U.S.A. For each glacier, the 1970/1973 DEM was 3-D co-registered (horizontal and vertical) to maximize agreement between the non-glacierized terrains of both DEMs. Over the period 1970–2001, total ice volume loss was 0.69 ± 0.06 km^3 corresponding to a mean (area-weighted) specific mass balance rate of -0.54 ± 0.05 m w.e. a^{-1} (± uncertainty). The arithmetic mean of all glaciers' specific mass balance rates was -0.47 ± 0.27 m w.e. a^{-1} (± 1 std. dev.). A value of -0.52 ± 0.36 m w.e. a^{-1} (± 1 std. dev.) was found when 3-D co-registration is performed over the entire domain instead of individually for each glacier, indicating the importance of proper co-registration. Glacier area, perimeter, boundary compactness, mean elevation, and mean slope were correlated with specific balance rates, suggesting that large, low-elevation, elongated and shallow sloped glaciers had more negative balance rates than small, high-elevation, circular, and steep glaciers. A subsample of 36 glaciers showed a mean area reduction of 26 ± 16 % (±1 std. dev.) over ~35 years.

---

[2] Published as Jason Geck, Regine Hock, and Matt Nolan "Geodetic Mass Balance of Glaciers in the Central Brooks Range, Alaska, U.S.A., from 1970 to 2001," Arctic, Antarctic, and Alpine Research 45(1), 29-38, (1 February 2013). https://doi.org/10.1657/1938-4246-45.1.29

2.2 Introduction

Climate change is impacting Alaska's glaciers, resulting in accelerated rates of mass loss (Arendt and others, 2002; Molnia, 2007; Berthier and others, 2010). In contrast to the large ice masses in Alaska's south and southeast, Alaska's arctic glaciers, geographically defined as located north of the Arctic Circle (66°33′N), include relatively small valley and cirque glaciers. Most of these glaciers started to retreat in the 1890s with a more significant retreat and thinning during the last four decades (Rabus and Echelmeyer, 1998; Nolan and others, 2005; Sikorski and others, 2009). Although small contributors to rising sea level, these glaciers are important indicators of climate change and provide information on long-term climate variations in an area that has few meteorological stations. In addition, these thinning glaciers contribute additional water to streamflow. Recent observations in the Arctic have shown an increase in discharge levels (Peterson and others, 2002). Continued glacier retreat and thinning will ultimately lead to reduced streamflow (Hock and Jansson, 2005), potentially impacting arctic stream ecology (Nolan and others, 2011). Currently the only long-term glacier mass balance record in Arctic Alaska comes from McCall Glacier (69°18′N, 143°48′W), with an area-averaged rate of -0.35 ± 0.07 m w.e. a^{-1} between 1956 and 1993 and an increased rate of -0.47 ± 0.03 m w.e. a^{-1} from 1993 to 2002 (Nolan and others, 2005).

Many studies in Alaska have assessed geodetic glacier mass balance by differencing DEMs of different years (e.g. Cox and March, 2004; Larsen and others, 2007; Berthier and others, 2010). Cox and March (2004) compared mass balance results obtained from both direct and geodetic methods. Larsen and others (2007) found substantial glacier thinning on glaciers in southeast Alaska and Canada using DEMs derived from

U.S. Geological Survey (USGS) topographic maps and Shuttle Radar Topography Mission (SRTM). Berthier and others (2010) estimated that Alaska's glaciers contributed 0.12 ± 0.02 mm to sea level rise between 1962 and 2009, which corresponds to 7.5 % of the total sea level rise estimate for the period 1961–2003 by Domingues and others (2008).

To determine surface elevation change with DEM differencing, accurate co-registration between DEMs is required. This typically includes a 2-D (horizontal) or 3-D (both horizontal and vertical) co-registration between two DEMs. Several studies have co-registered DEMs, but few have compared the impacts on results from the mis-registration of DEMs prior to differencing. Van Niel and others (2008) found that a mis-registration of half a pixel dramatically impacted elevation differences, with errors compounded on steep slopes. Nuth and Kääb (2011) described the analytical solution to DEM mis-registration. Berthier and others (2004, 2006, 2010) co-registered DEMs by minimizing the elevation error of the non-glacierized regions. In this study, we co-register DEMs for each glacier individually and collectively within one spatial domain, using statistical minimization methods for comparison.

This study determines the volume and mass change between 1970 and 2001 for 107 small valley and cirque glaciers in the central Brooks Range, Arctic Alaska, using DEMs derived from USGS topographic maps and airborne interferometric synthetic aperture radar (referred hereafter as the 2001 DEM). For each glacier, a 1970 or 1973 DEM was created from USGS topographic maps and 3-D co-registered to the 2001 DEM to maximize agreement between non-glacierized terrains of both DEMs. To explore the effect of mis-registration, we computed glacier volume change for alternate co-

registration methods. We also determined volume change using the 1970/1973 USGS national elevation data set (NED) for comparison to the results derived from our reconstructed DEMs. Optical satellite remote sensing (Quickbird; Digital Globe, http://www.digitalglobe.com) was used to update glacier boundaries and determine area change rates between 1970/1973 and 2001–2007 for a subset of 36 glaciers visible in imagery. Additionally, several topographic and geometric indices were related to mass balance results to explore the dependence of small glacier response on topography to changing climatic conditions.

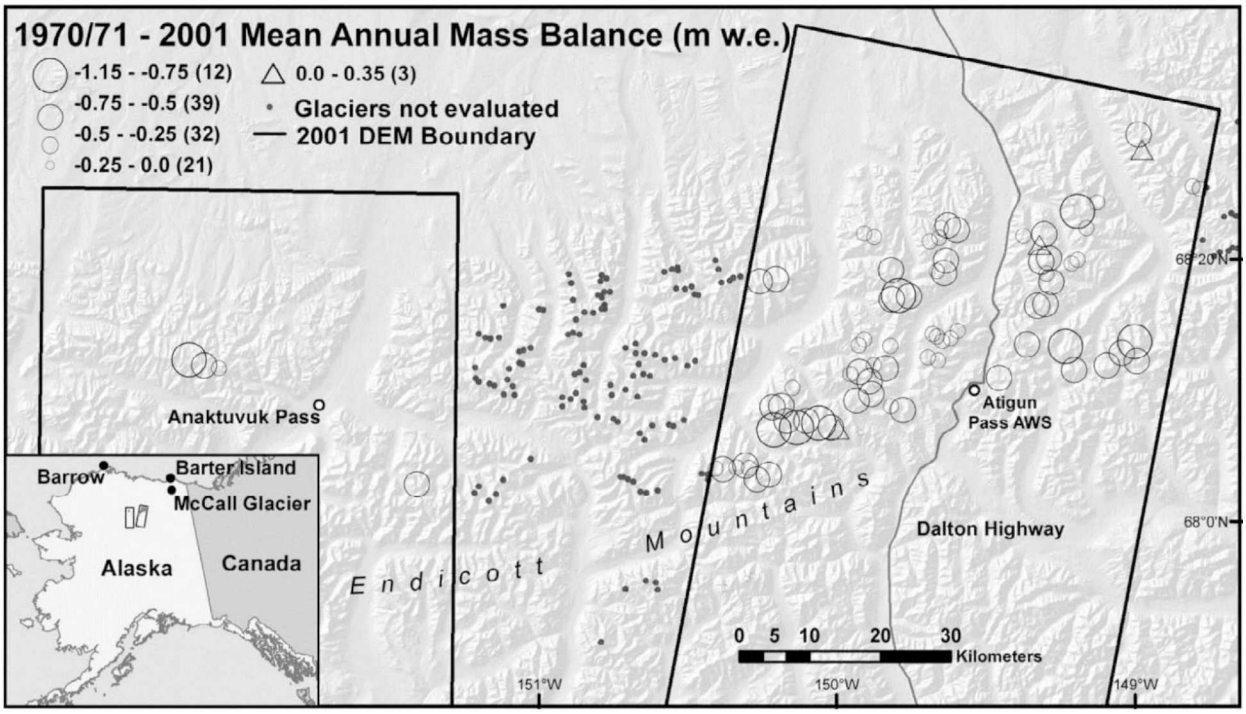

Figure 2.1: Location and mean mass balance rate (m w.e. a^{-1}) for each of the 107 investigated glaciers for the period 1970/1973 to 2001. Circles (triangles) indicate glacier thinning (thickening). Values in parentheses indicate the number of glaciers within each mass balance rate range. Boxes indicate the boundaries of the 2001 DEM. Dots refer to glaciers not evaluated as they lie outside the boundaries of the 2001 DEM. McCall Glacier, Barter Island, and Barrow locations are indicated on the vicinity map.

2.2.1. Geographic Setting

Alaska's arctic glaciers are located in the Brooks Range, a 1000-km-long mountain range in northern Alaska with elevations reaching 3000 m above sea level (a.s.l.) in the east. The glaciers evaluated in this study fall within the Endicott Mountains subrange (Fig. 2.1). The glaciers are located at a mean elevation of 1747 m a.s.l. (1250–2210 m a.s.l.). The 107 glaciers investigated here (total area = 42 km^2, 1970/1973) represent 13 % of ~850 Brooks Range glaciers covering 520 km^2 (the value is based on digitized glacier outlines from USGS maps; B. Manley, unpublished data) and corrects a previously published erroneous area estimate (598 km^2) by Berthier and others (2010) (Berthier, personal communication, 2011). The majority of the 107 glaciers are small, north-facing cirque glaciers (Fig. 2.2) ranging in size from 0.05 km^2 to 1.97 km^2 with mean size of 0.39 ± 0.35 km^2 (±1 std. dev.). The mean annual temperature and annual precipitation totals for the period 2000–2009 observed at the Atigun Pass weather station were -9.5 °C and 0.58 m, respectively (Snowtel Site #957, 1463 m a.s.l., NWCC http://www.wcc.nrcs.usda.gov/snotel/Alaska/alaska.html; Fig. 2.1).

2.2.2 Data

2001 DEM

The most recent DEM (10 m grid spacing) was acquired 18–30 August 2001 by the Intermap Technologies Corporation's Star3i system. Two separate areas covering over 19,000 km^2 were captured and contained 123 glaciers within the boundaries (Fig. 2.1). A total of 16 glaciers were eliminated from the analysis—nine due to small size (<0.05 km^2) and seven due to poor agreement in non-glacierized elevations between the earlier and the 2001 DEM. The proprietary Star3i system uses interferometric synthetic

aperture radar (IFSAR, X-band) to generate DEMs with a horizontal accuracy of 2 m and vertical accuracy of 1 m (Intermap, http://www.intermap.com). Wave penetration into snow from X-band is <3 cm when water is present (Haritashya and Singh, 2011). The 2001 DEM was collected during the late summer period when ablation areas are generally snow-free and water is present in the snow in the accumulation area, so wave penetration is considered minimal in this study.

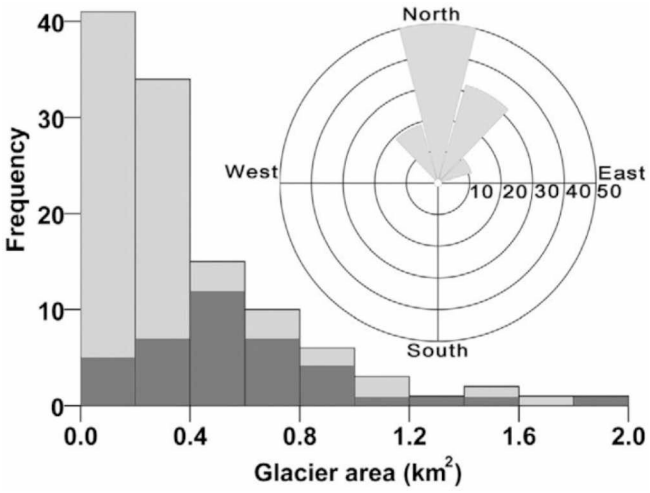

Figure 2.2: Size and aspect distributions of the 107 investigated glaciers in the central Brooks Range, Alaska, per 0.2 km^2 size classes. Darker gray part of the histogram depicts subsample of the 36 glaciers for which area reduction between 1970/1973 and 2001–2007 could be determined. Inset rose diagram depicts number of glaciers per 20° aspect classes for the 107 glaciers.

National Elevation Dataset (NED) 1970/1973 DEM

The 1970/1973 USGS national elevation data set (NED) DEM (~40 m grid spacing) was downloaded from the USGS web server (http://seamless.usgs.gov) and projected into UTM zone 5 WGS84 along with re-sampling to a 10 m grid spacing (cubic convolution

method). The NED DEM was originally created from vertical photography derived elevation contours produced for USGS topographic maps. The specific creation methods are poorly documented, and contour interpolation techniques are unclear. These unknown aspects of the NED prompted us to construct new DEMs from the original USGS topographic maps with the same grid spacing as the 2001 DEM (10 m).

Reconstructed 1970/1973 DEMs

We reconstructed the 1970/1973 DEMs using a combination of manual and automated workflows, henceforth referred to as the reconstructed DEMs. Eleven original 1:63,360 USGS topographic map separates (mylar sheets with brown lines for elevation contours and blue lines for glacier boundaries) were acquired digitally (1200 dpi or 1.3 m ground resolution) from the USGS. The maps referred to 1970 air photos for 102 glaciers and 1973 air photos for five glaciers. An example of a glacier's 1970 NED DEM, reconstructed 1970 DEM, and 2001 DEM is illustrated in Figure 2.3, parts a-c. Within a Geographical Information System (GIS, ArcGIS v9.3), map separates were georeferenced (mean georeferencing error: 2.2 ± 1.0 m) using corner coordinates. Glacier outlines were digitized from the original USGS maps.

Contours within each glacier and within a 1 km distance of each glacier boundary were automatically digitized from georeferenced map separates and manually attributed with elevation values. Contours were interpolated to reconstruct DEMs using a modified spline technique with drainage enforcement (Anudem v5.2) root mean square error (RMSE = 2.4 ± 0.2 m, mean ± 1 std. dev.) at the same 10 m grid spacing as the 2001 DEM (Hutchinson, 1989). Contour interpolation with no drainage enforcement yielded no difference within results.

2.3 Methods

2.3.1 DEM Co-registration

Due to the small glacier sizes within the study, proper co-registration of DEMs was necessary prior to DEM differencing. A preliminary investigation indicated a need for 3-D co-registration (both horizontal and vertical) of reconstructed DEMs to match the more accurate 2001 DEM, thereby reducing potential inaccuracies in volume change calculations from mis-registration. We assumed that the 2001 DEM represents the true surface elevation and thus treated it as a reference DEM. Its non-glacierized area was assumed to have experienced no surface elevation change over the investigated time period. For each glacier, the 1970/1973 reconstructed DEM was shifted sequentially by up to 10 pixels in all combinations of the 4 cardinal directions. A root mean square error (RMSE) was used to estimate the vertical error between the reconstructed DEMs and the 2001 DEM. RMSE values were only calculated for the non-glacierized terrain surrounding the glaciers (1 km buffer). Each individual reconstructed glacier 1970/1973 DEM was co-registered to a final location based on the minimum RMSE values found for the non-glacierized region. Each DEM was then vertically shifted by ± 25 m at 0.1 m intervals to allow 3-D co-registration. A RMSE value was again calculated for each individual vertical shift combination between each individually reconstructed DEM and the 2001 DEM. The initial 2-D co-registration of DEMs reduced the associated horizontal positional error due to georeferencing errors. As of 2011, no vertical datum transformation exists in Alaska for NGVD29 (USGS maps) to a more commonly used datum (Nolan and others, 2005). The 3-D co-registration eliminated the need for vertical datum transformations from NGVD29 to NAVD88 and reduced concern over the

poor survey control of original USGS maps. We investigated the validity of the two-step procedure adopted here for co-registration by performing co-registration in one single step for 20 glaciers. Differences in results were negligible.

For comparison we also computed mass balances without any DEM co-registration and with only a vertical but no horizontal co-registration. We also applied all three co-registration techniques to a single DEM containing all glaciers (individual reconstructed DEMs aggregated into one DEM), i.e. the entire DEM was co-registered rather than each glacier individually. The purpose was to assess whether this simpler method yields results like those obtained from co-registering each glacier DEM individually. Finally, we applied the same co-registration methods to each individual NED glacier DEM. RMSE and co-registration parameters are shown in Table 2.1. As expected, the elevation error of the non-glacierized areas decreased as co-registration was performed in more directions. Figure 2.4 visualizes the direction and magnitude of the 3-D co-registration of each individual glacier DEM and indicates large variability in direction and magnitude between glaciers.

2.3.2. Mass Balance Calculation and Glacier Area

Volume change was calculated for each glacier by subtracting the reconstructed 1970/1973 DEMs from the 2001 DEM. We assumed lost volume consisted of ice (density = 900kgm^{-3}; Bader, 1954) to allow volume change conversion to mass change. Hence, our estimates are an upper bound since the actual density may be lower due to retreat and thinning of firn; however, information to quantify this effect is lacking. Specific mass balance was determined by dividing the volume change by the glacier area. Previous studies have generally used the mean glacier area over the considered

period for calculating specific mass balances (Finsterwalder, 1954; Arendt and others, 2002). For the earlier DEMs we determined glacier area from the glacier outlines digitized from the maps. Our 2001 glacier area estimate is based on manual digitization of glacier boundaries on recent high-resolution optical satellite images (Quickbird) via Google Earth™ (Fig. 2.3, part e). Of the 107 glaciers, 20 were not visible in satellite images (covered by snow, clouds, or shadows). All other glaciers visible in satellite images showed signs of retreat. A total of 8 out of the 87 remaining glaciers had no ice present but had past glacier evidence (e.g. defined lateral or terminal moraines). Several glaciers were visible on satellite imagery, but glacier boundaries were difficult to discern (e.g. due to rockfall). We were able to digitize the glacier outlines of 36 glaciers that had clearly defined boundaries on the imagery. These images were captured in 2001 (1 glacier), 2003 (9 glaciers), and 2007 (26 glaciers).

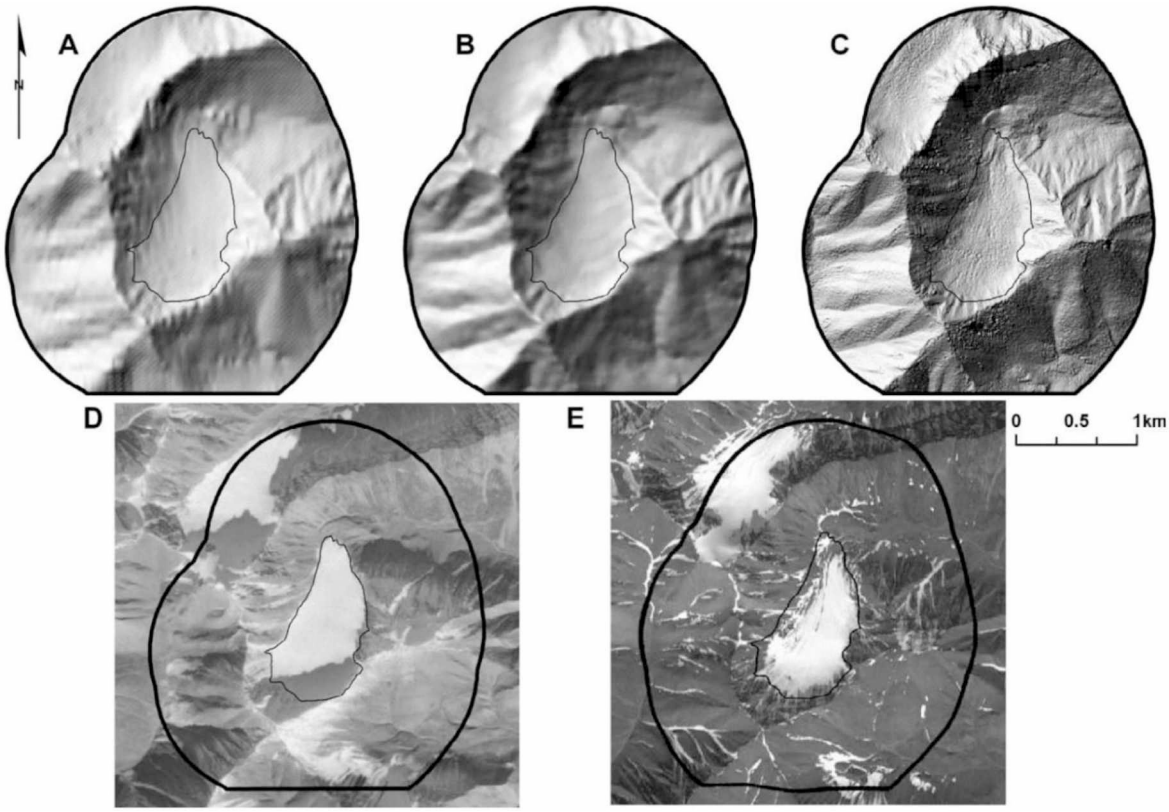

Figure 2.3: Shaded relief illustration of three different DEMs of one of the investigated glaciers (10 m grid spacing): (A) national elevation data set (NED) DEM (1970), (B) reconstructed DEM (1970) from U.S. Geological Survey (USGS) topographic maps, and (C) the 2001 DEM acquired by Intermap Technologies Corporation's Star3i system. (D) Image of the glacier on an original USGS aerial photograph captured 1 September 1970, and (E) a Quickbird satellite scene (captured July 2003; Google Earth™). The mean mass balance rate of the glacier is -0.62 m w.e. a^{-1} for the period 1970 to 2001. Thick line surrounds the glacier at one km distance with thin line depicting the glacier boundary.

Table 2.1: Co-registration parameters for the 107 investigated Brooks Range glacier DEMs using two different 1970/1973 DEMs ('reconstructed' and NED DEM) and several co-registration methods. Results are shown for the case where 3-D co-registration was applied to each glacier individually and for the case where it was applied to the entire DEM domain. 'Reconstructed' DEMs were produced in this study from the original U.S. Geological Survey topographic maps. RMSE is the root mean square of the elevation error of the 1970/1973 DEM given as the arithmetic mean of all glacier DEMs (± 1 std.dev.). Easting/Northing shift reflects the horizontal directional shift. Positive values indicate a North or East shift, while values reflect a South or West shift (± 1 std.dev.).

	RMSE (m)	Easting shift (m)	Northing shift (m)	Vertical shift (m)
(A) 2001 DEM minus reconstructed 1970/1973 glacier DEMs (each glacier co-registered individually)				
(a) No co-registration	14.1 ± 3.3	—	—	—
(b) Vertical shift only	12.3 ± 3.4	—	—	−3.9 ± 5.8
(c) 3-D co-registration	10.6 ± 3.0	2.3 ± 11.0	1.5 ± 11.3	−3.8 ± 5.2
(B) 2001 DEM minus 1970/1973 NED DEMs (each glacier co-registered individually)				
(a) No co-registration	14.6 ± 3.2	—	—	—
(b) Vertical shift only	12.9 ± 3.4	—	—	−4.0 ± 5.6
(c) 3-D co-registration	10.9 ± 3.0	2.1 ± 11.6	7.4 ± 10.9	−3.8 ± 5.1
(C) 2001 DEM minus reconstructed 1970/1973 glacier DEM (entire domain co-registered)				
(a) No co-registration	14.6	—	—	—
(b) Vertical shift only	14.1	—	—	−3.8
(c) 3-D co-registration	13.0	0.0	10.0	−4.3

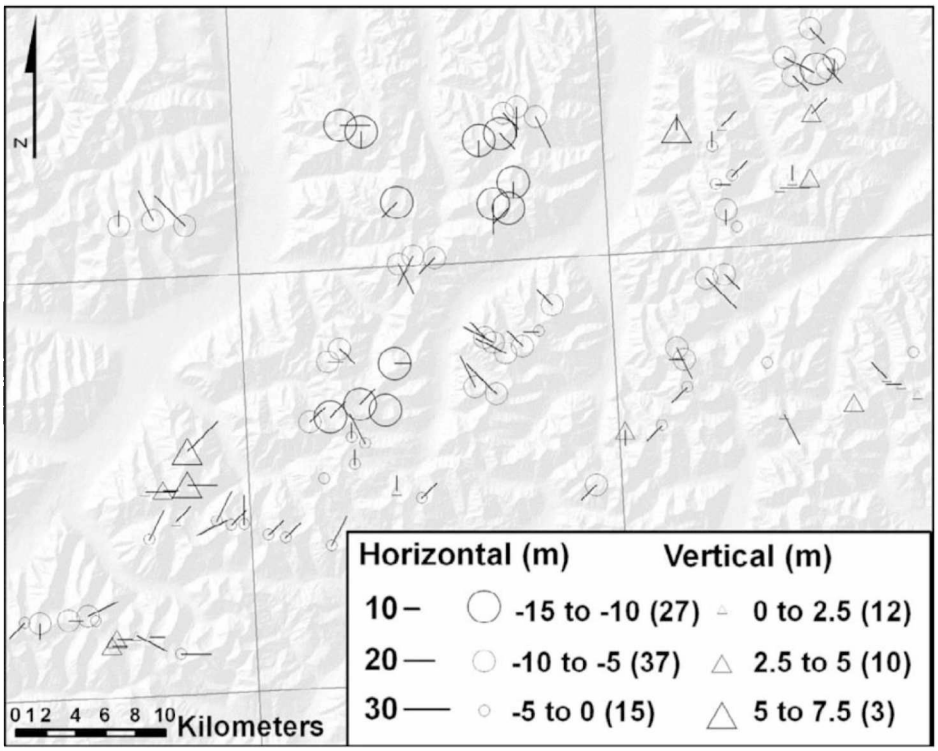

Figure 2.4: Co-registration parameters for a subset (94) of the107 reconstructed 1970/1973 glacier DEMs. Lines represent the direction and magnitude of 2D (horizontal) co-registration for glacier DEMs. Circles (triangles) indicate negative vertical shift (positive). Values in parentheses indicate the number of glaciers within each vertical shift range. The thin lines reflect 1:63,360 USGS quadrangle borders.

For each of the 36 glaciers a mean area reduction rate between the earlier (1970 or 1973) and the later (2001, 2003, or 2009) date was calculated. These rates were then applied to each of the 36 glaciers to compute the area in 2001 and 1970 (if glacier outline referred to 1973). The arithmetic mean of all 36 area reduction rates was applied to all remaining glaciers to compute the 2001 area of each of these glaciers. The computed total area of all 107 glaciers for the year 2001 was 30.5 km^2. The mean of each glacier's area in 1970 and 2001 was then used to compute the specific balances of each glacier. An average mass balance rate (m w.e. a^{-1}) was calculated for each glacier over the 31- (1970–2001) or 28-year period (1973–2001).

To compute an area-weighted specific glacier mass balance rate for the entire spatial domain for 1970–2001, we extrapolated the 1973–2001 volume losses of the 5 glaciers with 1973 DEMs to the earlier date (1970) by assuming their specific mass balance rates over 1970–2001 to be constant. To convert into specific mass balance units, we divided the volume change by the mean of the 1970 and 2001 glacier areas.

2.3.3. Topographic and Geometric indices

Within a GIS, we used each glacier's boundary from 1970/ 1973 and the 2001 DEM to calculate glacier area, perimeter length, mean elevation, mean slope, boundary compactness, and mean annual potential solar radiation. These were calculated to assess if these factors impact the response of each glacier to changing climate. Boundary compactness is the ratio of the perimeter of a circle with the same area as the glacier and the perimeter of that glacier (Allen, 1998). Boundary compactness ranges between 0 and 1, where elongated polygons typical of valley glaciers have lower values than more circular polygons typical of cirque glaciers. Mean annual potential solar radiation was also calculated for each glacier using topography from the 2001 DEM. We tested indices for significant ($p < 0.05$) Pearson correlations (SPSS v18) with specific mass balance rates for all glaciers. Because several indices are naturally correlated (e.g. greater area results in greater perimeter), principal component analysis was also conducted to identify a set of uncorrelated variables.

2.3.4. Estimating Uncertainties

Standard principles of error propagation were used to determine error estimates between two DEMs within the DEM differencing process (Burroughs and others, 1998). However, DEMs are highly spatially autocorrelated. To account for the spatial

autocorrelation, we estimated the uncertainty using uncorrelated measurements between the two DEMs (Nuth and Kääb, 2011). We assumed an autocorrelation distance of 0.25 km to allow for an adequate sample size. Other studies' autocorrelation distances range from 0.1 to 1 km (Koblet and others, 2010; Kääb, 2008). Thus, we examined 4 % of the total population of pixels differenced between DEMs to account for spatial autocorrelation. We estimated the uncertainty between the two independent DEMs by the following equation:

$$\epsilon = \sqrt{\sigma_1^2 + \sigma_2^2} \quad (1)$$

where σ1 and σ2 represent the random errors associated with each individual DEM. These were derived from the error components listed in Table 2.2. These include the original glacier contour representation on original USGS maps and contour interpolation. We calculated the standard error following the methods of Nuth and Kääb (2011) resulting in an overall uncertainty of 0.05 m w.e. a^{-1} for the area-averaged specific balance of all 107 glaciers. This standard error value is low in comparison to the individual glacier errors (ranging from 0.08 to 0.13 m w.e. a^{-1} mean = 0.11 m w.e. a^{-1}) due to the larger number uncorrelated measurements.

Table 2.2: Sources of random error for each individual pixel of the DEMs.

Error component	Error (m)	Source
Reconstructed 1970/1973 DEMs		
Map contour elevations	± 30	(Aðalgeirsdóttir et al., 1998)
Contour interpolation	± 3	(Hutchinson, 1989)
2001 DEM		
Band X ice/snow penetration	± 0.1	(Haritashya and Singh, 2011)
DEM elevation	± 1	(Intermap, 2011)

The error associated with the original USGS topographic maps dominates the uncertainty in our reconstructed DEMs. Aðalgeirsdóttir and others (1998) found errors as great as ± 45 m in glacier accumulation areas of the Harding Icefield for USGS contour elevations. However, errors tend to be larger in wide accumulations areas with small slope (Aðalgeirsdóttir and others, 1998; Muskett and others, 2003). We assumed a smaller error of ± 30 m for the USGS contour elevations as our investigated glaciers are narrow valley or cirque glaciers. The 2001 DEM (vertical accuracy ± 1.0m) was collected using X-band IFSAR during the late summer period. We assumed minimal penetration of radar waves into glacier snow/ice and so allowed a 0.1 m error into our error estimates. Any other errors were considered small compared to the elevation change errors and not considered here.

Table 2.3: Mean mass balance rates, $\dot{B}$ for the 107 investigated Brooks Range glaciers for the period 1970/1973 to 2001 using two different 1970/1973 DEMs and several co-registration methods. 'Num. $\dot{B}^+$' is the number of glaciers found to have mass gain along with the percentage of total number of glaciers in parenthesis is the arithmetic mean of the specific balance rates of all glaciers (± 1 std.dev.). $\dot{B}_{min/max}$ is the minimum/maximum mass balance rate of the glacier sample (m w.e. a^{-1}). ΔZ is the mean elevation change of all glaciers (± 1 std.dev.).

	$Num.\dot{B}^+$ (%)	$\dot{B}$ (m w.e. a^{-1})	$\dot{B}_{min}$ (m w.e. a^{-1})	$\dot{B}_{max}$ (m w.e. a^{-1})	ΔZ (m)
(A) 2001 DEM minus 1970/1973 reconstructed glacier DEMs (each glacier co-registered individually)					
(a) No co-registration	9 (8)	−0.60 ± 0.39	−1.40	1.00	−20.6 ± 13.5
(b) Vertical shift only	8 (7)	−0.47 ± 0.32	−1.07	0.79	−16.0 ± 10.9
(c) 3-D co-registration	3 (3)	−0.47 ± 0.27	−1.12	0.34	−16.2 ± 9.1
(B) 2001 DEM minus 1970/1973 NED DEMs (each glacier co-registered individually)					
(a) No co-registration	8 (7)	−0.62 ± 0.40	−1.82	0.91	−21.1 ± 13.8
(b) Vertical shift only	11 (10)	−0.48 ± 0.35	−1.90	0.78	−16.4 ± 11.9
(c) 3-D co-registration	2 (2)	−0.55 ± 0.29	−1.99	0.06	−18.9 ± 9.9
(C) 2001 DEM minus 1970/1973 reconstructed glacier DEM (entire domain co-registered)					
(a) No co-registration	9 (8)	−0.60 ± 0.39	−1.40	1.00	−20.6 ± 13.5
(b) Vertical shift only	13 (12)	−0.43 ± 0.39	−1.25	1.13	−14.7 ± 13.3
(c) 3-D co-registration	11 (10)	−0.52 ± 0.36	−1.30	0.47	−18.0 ± 12.2

2.4 Results and Discussion

2.4.1. Mass Balance 1970–2001

Using 3-D co-registered reconstructed 1970/1973 glacier DEMs, the total ice volume lost by the 107 glaciers between 1970 and 2001 was 0.69 ± 0.06 km^3, corresponding to a mean specific area-weighted balance rate of -0.54 ± 0.05 m w.e. a^{-1} (± uncertainty). The arithmetic mean of all balances (not area-weighted) is - 0.47 ± 0.27 w.e. a^{-1} (± 1 std. dev.; Table 2.3, part a). The rate varied widely among the glaciers ranging from -1.12 ± 0.09 (± uncertainty) to 0.34 ± 0.12 m w.e. a^{-1} with 104 glaciers losing mass and three glaciers gaining mass (0.05 ± 0.12, 0.09 ± 0.12, and 0.34 ± 0.12 m w.e. a^{-1}) during the study period (Table 2.3, part a). These three glaciers are among the smallest glaciers

(0.09, 0.09, and 0.05 km^2, respectively). Hence, the positive balances may be artifacts of co-registration errors.

The observed volume loss is consistent with an observed increase in air temperatures and a decrease in annual precipitation. Weather stations are sparse in the region; only two long-term records are available for the Arctic—Barrow and Barter Island—and are roughly 300 and 100 km away from the studied glaciers, respectively (Fig. 2.1). Mean temperature increased at both Barrow and Barter Island between 1965 and 1995 (1.4 °C and 1.0 °C, respectively; Curtis and others, 1998) while annual precipitation decreased between 1949 and 1988 (30 % and 47 %, respectively; Curtis and others, 1998). On McCall Glacier, Rabus and Echelmeyer (2002) estimated a 1.1 ± 0.3 °C increase in air temperature between 1975 and 1995.

Our mass losses over the period 1970 to 2001 (0.54 ± 0.05 m w.e. a^{-1}) are larger than those from previous studies within the Brooks Range. McCall Glacier located ~220 km from our closest investigated glacier (Fig. 2.1) showed mass balances of -0.35 ± 0.07 m w.e. a^{-1} from 1956 to 1993 and -0.47 ± 0.03 m w.e. a^{-1} from 1993 to 2002 (Nolan and others, 2005). The glacier is much larger (~6.4 km^2) than our glaciers. Berthier and others (2010) reported a mean mass balance rate of -0.37 ± 0.06 m w.e. a^{-1} for all Brooks Range glaciers during 1956–2001. They applied McCall Glacier's mass balance profile to the area-altitude distribution of the unmeasured glaciers based on the conclusion of Rabus and Echelmeyer (1998) that McCall Glacier was representative of glaciers in the northeastern Brooks Range. Our results indicate that McCall Glacier's mass changes may not be representative for the regional-scale mass changes

occurring in the Brooks Range, although differences may at least partially be due to different time periods between our and their study.

Despite the arctic location of our investigated glaciers, our results are consistent with those from glaciers located throughout Alaska. Arendt and others (2002) found an area-weighted mean thinning rate of -0.52 m ice eq. a^{-1} for 67 glaciers located throughout Alaska between the mid-1950s and mid-1990s. Berthier and others (2010) in their statewide Alaska DEM differencing study found varying regional results for the 1960s–2006 time period ranging from -0.19 m w.e. a^{-1} in the Alaska Peninsula to -0.65 m w.e. a^{-1} in southeast Alaska. Although these time periods are different, all studies show consistent thinning over the last 50 years of the same order of magnitude.

2.4.2. Glacier Area Changes

For the 36 glaciers whose recent boundaries could be digitized, total glacier area was reduced from 21.5 km^2 (original USGS maps from 1970 or 1973) to 16.4 km^2 (satellite images between 2001 and 2007), a 24 % area reduction in about 35 years. The arithmetic mean of all individual glaciers' area reduction rates was 0.73 ± 0.44 % a^{-1} (± 1 std. dev.). Results may be affected by errors due to misclassification of perennial snow in the USGS maps; this error is unknown. However, Granshaw and Fountain (2006) compared a glacier inventory derived manually from aerial photos (Post and others, 1971) to a new digital inventory derived from USGS topographic maps. The total glacier-covered area of the former (116 km^2) differed from the latter by only 1.5 % over a total glacier area of 116 km^2. These 321 glaciers were very similar in area (mean area = 0.4 km^2) to our investigated glaciers (0.39 km^2).

Figure 5 depicts annual reduction rates versus original 1970/ 1973 glacier area. Despite the scatter, results indicate that relative area loss tends to be greater for smaller glaciers. Results may not be representative of the entire glacier sample since the size distribution of the 36 glacier subsample is biased towards larger glaciers (Fig. 2.2). Nevertheless, these results are an additional indication of widespread mass loss and are consistent with our quantitative results obtained from DEM differencing.

2.4.3. Topographic Indices

We tested for correlations between the specific mass balance rates and topographic indices using the Pearson correlation coefficient. Results are based on 3-D co-registration of each individual reconstructed DEM. Table 2.4 provides statistical summaries of the topographic indices calculated. We observed significant negative correlations between mass balance and glacier area ($r = -0.33$; Fig. 2.6, part a) and glacier perimeter ($r = -0.39$). This suggests that the larger glaciers thinned more than the smaller glaciers. The larger glaciers in Brooks Range are valley glaciers while the smaller glaciers tend to be more circular cirque glaciers. Significant positive correlations were found for mean glacier slope ($r = 0.48$; Fig. 2.6, part c), mean glacier elevation ($r = 0.19$; Fig. 2.6, part b), and compactness ($r = 0.26$; Fig. 2.6, part d; Table 2.4). This is consistent with the findings above since the small glaciers tend to be steeper, at higher mean elevations, and more circular than the larger glaciers. No significant correlations were found between mass balance rates and potential solar radiation, longitude, or latitude (Table 2.4).

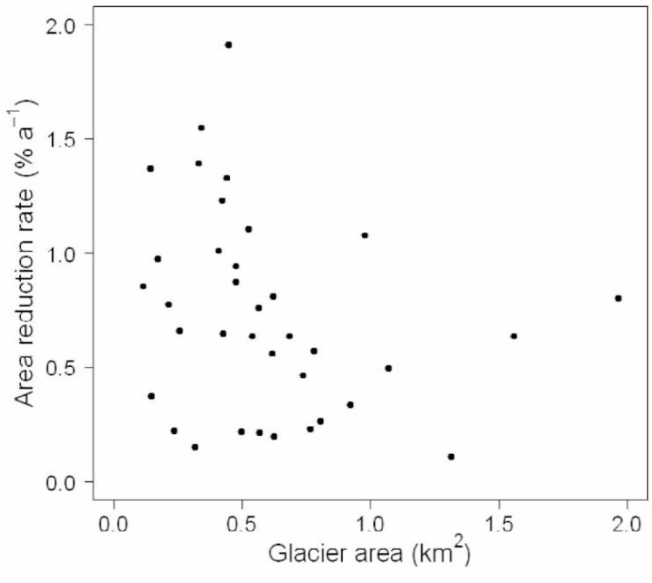

Figure 2.5: Mean area reduction rates of 36 glaciers between 2001 and 2007 (recent satellite imagery) and 1970/1973 glacier area (USGS maps).

As these indices are naturally correlated, we used principal component analysis (varimax rotation method; IBM, 2011) to reduce six variables (size, perimeter, compactness, elevation, slope, and radiation) into two components. The first component axis was principally determined positively by glacier size (loading = 0.89) and perimeter (0.95), while negatively by compactness (0.73) and mean slope (0.65). This "shape and steepness" axis represented a gradient from large, elongate, and flat glaciers to small, round, and steep glaciers and captured 49 % of the variance among the six variables. The mass balance rate was significantly and negatively correlated with the "shape and steepness" axis component ($r = - 0.45$, $P < 0.01$, $n = 107$), confirming that larger, more elongated, and shallow-sloped (valley) glaciers thinned more than smaller, more circular, steeper-sloped (cirque) glaciers. The second component, which accounted for 23 % of the variance, included mean elevation (0.89) and potential solar radiation (0.78). This "elevation and solar radiation" axis

represented a gradient from low-elevation glaciers with low potential solar radiation to higher elevations with high solar radiation. The mass balance rate was not significantly correlated with the "elevation and solar radiation" axis component ($r = 0.07$). Our results are consistent with findings by De Beer and Sharp (2009), who evaluated glacier area retreat for small glaciers (<0.4 km^2) in the Monashee Mountains, British Columbia, Canada. They found that larger glaciers exhibited larger retreat rates than smaller glaciers as the smaller glaciers tended to occupy topographically sheltered sites. The authors suggested that shading and topography reduced mass loss of small cirque glaciers. A dependence of (areal) retreat rate on glacier size has also been found for a larger range of glacier sizes in glaciers in the European Alps (Paul and others, 2004), Norway (Andreassen and others, 2008), and the Canadian Rocky Mountains (Jiskoot and others, 2009).

Table 2. 4: Pearson correlation matrix between mean specific mass balance rates, $\dot{B}$ (using 3-D co-registered reconstructed DEMs) over the period 1970/1973 to 2001, and topographic and geometric indices. The top three rows are the mean ± std.dev. ($\bar{x}$+ σ), minimum (Min), and maximum (Max) of the results for the 107 investigated glaciers. A is the glacier area, P is the glacier perimeter, Z is the mean glacier elevation, α is the mean glacier slope, *I* is mean potential solar radiation, *C* is boundary compactness, λ is latitude, and ψ is longitude. Bold values indicate significance at the 95 % confidence interval.

	$\dot{B}$ (*m w.e. a*$^{-1}$)	*A* (km^2)	*P* (km)	*Z* (m a.s.l.)	*α* (degrees)	*I* (W m^{-2})	*C*	*λ* (degrees)	*ψ* (degrees)
± *σ*	−0.53 ± 0.29	0.39 ± 0.35	2717 ± 1475	1747 ± 123	23 ± 5	568 ± 80	0.79 ± 0.11	—	—
Min	−1.25	0.05	863	1351	12	300	0.52	67.89N	−152.56W
Max	0.37	1.97	8441	2017	39	777	0.98	68.44N	−148.66W
A	**−0.33**	1.00							
P	**−0.38**	**0.95**	1.00						
Z	**0.19**	0.04	−0.04	1.00					
α	**0.48**	**−0.47**	**−0.45**	**0.3**	1.00				
I	−0.18	**0.41**	**0.37**	**0.43**	**0.50**	1.00			
C	**0.28**	**−0.52**	**0.72**	0.10	0.17	0.12	1.00		
λ	0.08	0.05	0.01	**0.64**	0.11	**0.19**	0.12	1.00	
ψ	0.18	−0.13	−0.18	**0.40**	−0.01	−0.07	**0.22**	**0.48**	1.00

2.4.4. Sensitivity of Mass Balance Results to co-registration

We also computed mass balance using three co-registration methods of the 1970/1973 reconstructed glacier DEMs. These included (1) no co-registration, (2) no horizontal co-registration and only a vertical shift, and (3) a 3-D co-registration (both horizontal and vertical). The specific mass balance rates (mean of all glaciers) differed by up to 0.12 m w.e. a^{-1} between the three methods when each glacier was co-registered individually (Table 2.3, case A, a—c). The standard deviation and range of values tended to increase as co-registration was performed in fewer directions. Hence, although the mean balance rate averaged over all glaciers changed relatively little between different co-registration methods, the rate of individual glaciers was affected considerably as indicated by the larger range in balance rates (Table 2.3).

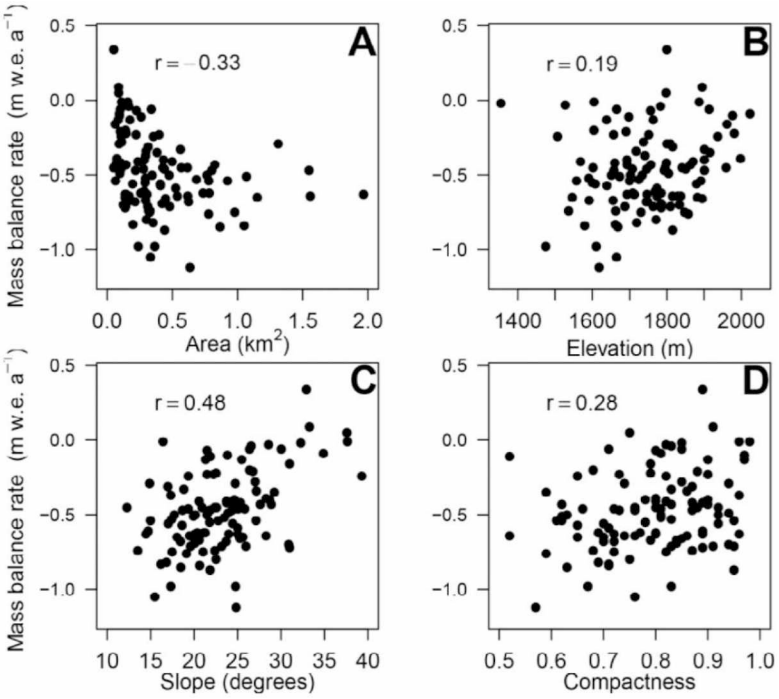

Figure 2.6: Mean mass balance rates (m w.e. $a^{-1}$of the 107 glaciers 1970/1973 to 2001 (3-D co-registered reconstructed DEMs) versus (A) glacier area, (B) mean glacier elevation, (C) mean glacier slope, and (D) glacier boundary compactness.

Past studies focused on DEM co-registration of larger domains including a large number of glaciers (Larsen and others, 2007; Berthier and others, 2010). Larger DEMs may contain internal distortions introduced from georeferencing or collection methods. We compared the results above with those derived from 3-D co-registration of a single DEM containing all glaciers (Table 2.3, case C). The elevation error (see RMSE in Table 2.1, case C) was consistently higher for all co-registration methods compared to the results derived from co-registration of each individual glacier DEM (Table 2.1, case A). This is not unexpected considering the lack of a consistent regionalscale pattern of co-registration direction and magnitude that was necessary to minimize the elevation error

of each individual glacier (Fig. 2.4). Some co-registration vectors exhibit some level of spatial autocorrelation indicating that for these glaciers co-registration at larger spatial scales could be sufficient. However, it is unclear how to identify these scales a priori.

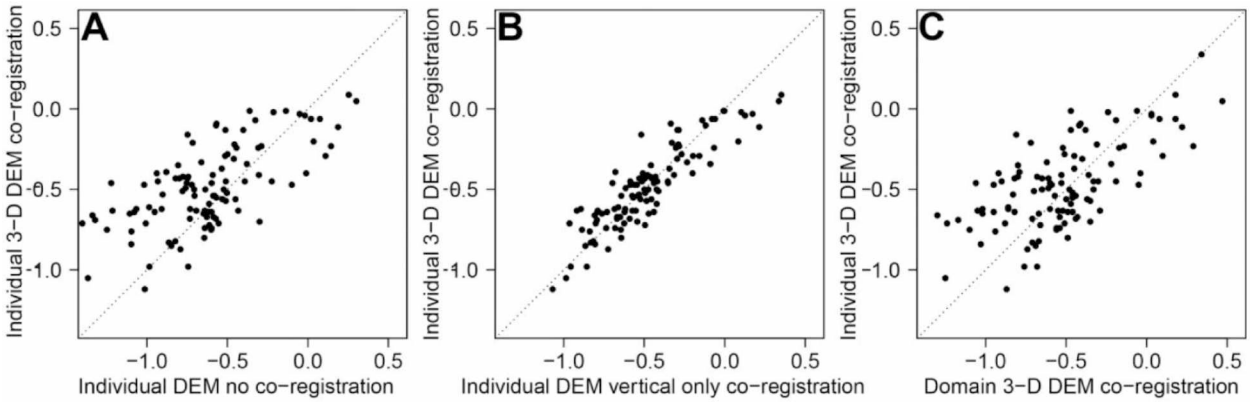

Figure 2.7: Mean mass balance rates (m w.e. a^{-1}) of the 107 glaciers 1970/1973 to 2001 for individual 3-D co-registered DEMs versus (A) individual DEMS with no co-registration, (B) individual DEMS with vertical co-registration only, and (C) 3-D co-registration of entire domain. The dotted line represents the one-to-one line.

The mean mass balance rate (averaged over all glaciers) differed by up to 0.27 m w.e a^{-1} between the two methods (Table 2.3, cases A and C) indicating that co-registration should be performed for each glacier individually rather than adopting the common method of 3-D co-registering a larger domain including many glaciers. Figure 2.7 illustrates the scatter between the glacier's specific mass balances using individual 3-D DEM co-registration and those derived from the alternative methods.

2.4.5. NED DEM Versus Reconstructed DEMs

We calculated mass balances by subtracting the 1970/1973 NED DEMs from the corresponding 2001 DEMs to compare to the mass balance results derived with our reconstructed DEMs. Although both DEMs are based on the same data source (i.e.

1970/ 1973 USGS topographic map contours), the mass balance results differed slightly from each other (Table 2.3, cases A and B). Consistent with the results using the reconstructed DEMs, we found a narrower range in mass balance rates and reduced standard deviations for 2-D co-registration versus no co-registration, and further reduction of range and standard deviation using 3-D co-registration (Table 2.3, case B). The slight differences may be explained by the unknown original interpolation technique used to create NED versus our modified spline technique (Hutchinson, 1989). Another reason for different results may be the initial difference of grid spacing between NED and our reconstructed DEMs. The NED, originally at ~40 m grid spacing, was re-sampled to the grid spac- ing of our reconstructed DEM (10 m). With similar elevation errors and mass balance results found between the NED glacier DEMs and our reconstructed glacier DEMs, we conclude that the NED DEM data set is appropriate for use for geodetic mass balance calculations in this region.

2.5. Conclusion

DEMs reconstructed from historical USGS topographic maps (1970/1973) differenced from a 2001 DEM within the central Brooks Range, Alaska, allowed us to calculate the volume change and mean specific mass balance rate for 107 glaciers over the period 1970/1973 to 2001. The area-weighted mean balance rate was - 0.54 ± 0.05m w.e. a^{-1} (± uncertainty). Hence, the mass loss is somewhat larger than the one reported for McCall Glacier (-0.35 ± 0.07 m w.e. a^{-1} [1956–1993] and -0.47 ± 0.03 m w.e. a^{-1} [1993–2002]), which is located ~220 km from our closest investigated glacier (Nolan and others, 2005). The mass loss is consistent with observed increasing air temperatures and decreasing annual precipitation at northern Alaska coastal weather stations during

the study period. The correlation of multiple topographical indices with specific mass balance suggests that the larger valley glaciers thinned more than the smaller cirque glaciers that have already retreated into topographically more sheltered sites.

Proper co-registration prior to DEM differencing was found to be important for the 107 studied glaciers that are small, located in steep terrain, with a predominately northern aspect. Co-registration direction and magnitude varied largely between glaciers in the investigated domain. In this study it was necessary to co-register each glacier individually instead of collectively within one larger spatial domain containing all glaciers. This is especially necessary when working with historical USGS-derived DEMs that are known to have poor horizontal and vertical control. Mass balances derived from the reconstructed 1970/1973 DEMs differed only slightly from those obtained using the NED DEMs. This demonstrates that for our study region the existing NED DEMS are appropriate for volume change calculations.

2.6. Acknowledgments

We thank B. Manley (INSTARR, University of Colorado Boulder) for providing a subset of digital glacier boundaries used within analysis. The Star3i DEM was funded by the NASA Commercial Remote Sensing Program. Analysis was supported by grants NSF OPP-0714045 and NASA NNX11AF41G. This work was also supported by the U.S. National Park Service's Arctic Network as part of their Inventory and Monitoring Program (H9910030024/J9910324509 and H9910080028/J9940090220). We also thank A., Arendt, M. Loso, C. Mulder, R. Dial, E. Creely, J. Williams, and classmates D. Podrasky, B.Truessel, and M. Engram for comments that greatly improved manuscript readability.

References

G. Aðalgeirsdáttir, K. A. Echelmeyer, and W. D. Harrison, 1998: Elevation and volume changes on the Harding Icefield, Alaska. Journal of Glaciology, 44(148): 570–582.

T. R. Allen, 1998: Topographic context of glaciers and perennial snowfields, Glacier National Park, Montana. Geomorphology, 21(3–4): 207–216.

L. M. Andreassen, F. Paul, A. Kääb, and J. E. Hausberg, 2008: Landsat-derived glacier inventory for Jotunheimen, Norway, and deduced glacier changes since the 1930s. The Cryosphere, 2: 131–145, http://dx.doi.org/10.5194/tc-2-131-2008.

A. A. Arendt, K. A. Echelmeyer, W. D. Harrison, C. S. Lingle, and V. B. Valentine, 2002: Rapid wastage of Alaska glaciers and their contribution to rising sea level. Science, 297: 382–386.

H. Bader, 1954: Sorge's Law of densification of snow on high polar glaciers. Journal of Glaciology, 2(15): 319–323.

E. Berthier, Y. Arnaud, D. Baratoux , C. Vincent , and F. Rémy , 2004: Recent rapid thinning of the “Mer de Glace” glacier derived from satellite optical images. Geophysical Research Letters, 31: L17401, http://dx.doi.org/10.1029/2004GL020706.

E. Berthier, Y. Arnaud, C. Vincent, and F. Rémy, 2006: Biases of SRTM in high-mountain areas. Implications for the monitoring of glacier volume changes. Geophysical Research Letters, 33: L08502, http://dx.doi.org/10.1029/2006GL025862.

E. Berthier, E. Schiefer, G. K. C. Clarke, B. Menounos, and F. Rémy, 2010: Contribution of Alaskan glaciers to sea level rise derived from satellite imagery. Nature GeoScience, 3(2): 92–95.

P. P. Burroughs, and R. A. McDonnel, 1998: Principles of GIS. New York: Oxford University Press, 299 pp.

L. H. Cox, and R. S. March, 2004: Comparison of geodetic and glaciological mass balance techniques, Gulkana Glacier, Alaska, U.S.A. Journal of Glaciology, 50(170): 363–370.

J. Curtis, G. Wendler, R. Stone, and E. Dutton, 1998: Precipitation decrease in the Western Arctic, with special emphasis on Barrow and Barter Island, Alaska. International Journal of Climatology, 18(15): 1687–1707.

M. De Beer, and M. Sharp, 2009: Topographic influences on recent changes of very small glaciers in the Monashee Mountains, British Columbia, Canada. Journal of Glaciology, 55(192): 691–700.

C. M. Domingues, J. A. Church, N. J. White, P. J. Gleckler, S. E. Wijffels, P. M. Barker, and J. R. Dunn, 2008: Improved estimates of upper-ocean warming and multi-decadal sea-level rise. Nature, 453: 1090–1093.

R. Finsterwalder, 1954: Photogrammetry and glacier research with special reference to glacier retreat in the eastern Alps. Journal of Glaciology, 2(15): 306–315.

F. D. Granshaw, and A. G. Fountain, 2006: Glacier change (1958–1998) in the North Cascades National Park Complex, Washington, USA. Journal of Glaciology, 52(177): 251–256.

V. S. Haritashya, and P. Singh, 2011: Encyclopedia of Snow, Ice and Glaciers. New York: Springer Press, 1253 pp.

R. Hock, and P. Jansson, 2005: Modelling glacier hydrology. In M. G. Anderson, and J. McDonnell (eds.), Encyclopedia of Hydrological Sciences. Chichester: John Wiley and Sons, vol. 4, 2647–2655.

M. F. Hutchinson, 1989: A new method for gridding elevation and streamline data with automatic removal of pits. Journal of Hydrology, 106: 211–232.

IBM, 2011: IBM SPSS Statistics for Windows, Version 20.0. Armonk, New York: IBM Corporation.

H. Jiskoot, C. M. Curran, D. L. Tessler, and L. R. Shenton, 2009: Changes in Clemenceau Icefield and Chaba Group glaciers, Canada, related to hypsometry, tributary detachment, length-slope and areaaspect relations. Annals of Glaciology, 50(53): 133–143.

A. Kääb, 2008: Glacier volume changes using ASTER satellite stereo and ICESat GLAS laser altimetry. A test study on Edgeøya, eastern Svalbard. IEEE Transactions on Geoscience and Remote Sensing, 46(10): 2823–2830.

T. Koblet, I. Gärtner-Roer , M. Zemp , P. Jansson , P. Thee , W. Haeberli , and P. Holmlund , 2010: Determination of length, area, and volume changes at Storglaciären, Sweden, from multi-temporal aerial images (1959–1999). The Cryosphere, 4: 333–343.

C. F. Larsen, R. J. Motyka, A. A. Arendt, K. A. Echelmeyer, and P. E. Geissler, 2007: Glacier changes in southeast Alaska and northwest British Columbia and contribution to sea level rise. Journal of Geophysical Research, 112: F01007, http://dx.doi.org/10.1029/2006JF000586.

B. F. Molnia, 2007: Late nineteenth to early twenty-first century behavior of Alaskan glaciers as indicators of changing regional climate. Global Planetary Change, 56: 23–56.

R. R. Muskett, C. S. Lingle, W. V. Tangborn, and B. T. Rabus, 2003: Multi-decadal elevation changes on Bagley Ice Valley and Malaspina Glacier, Alaska. Geophysical Research Letters, 30(16): http://dx.doi.org/10.1029/2003GL017707.

M. Nolan, A. Arendt, B. Rabus, and L. Hinzman, 2005: Volume change of McCall Glacier, arctic Alaska, from 1956 to 2003. Annals of Glaciology, 42: 409–416.

M. Nolan , R. Churchwell , J. M. Adams , J. McClelland , K. Tape , S. Kendall , A. Powell , K. H. Dunton , D. Payer , and P. D. Martin , 2011: Predicting the impact of glacier loss on fish, birds, floodplains, and estuaries in the Arctic National Wildlife Refuge. Proceedings of the Fourth Interagency Conference on Research in the Watersheds: Observing, Studying and Managing for Change. U.S. Geological Survey Scientific Investigations Report 2011–5169, 49–54.

C. Nuth, and A. Kääb, 2011: Co-registration and bias corrections of satellite elevation data sets for quantifying glacier thickness change. The Cryosphere, 5: 271–290, http://dx.doi.org/10.5194/tc-5-2712011.

F. Paul, A. Kääb, M. Maisch, T. Kellenberger, and W. Haeberli, 2004: Rapid disintegration of Alpine glaciers observed with satellite data. Geophysical Research Letters, 31: L21402, http://dx.doi.org/10.1029/2004GL020816.

B. J. Peterson, R. M. Holmes, J. W. McClelland, C. J. Vörömarty, R. B. Lammers, A. I. Shiklomanov, I. A. Shiklomanov, and S. Rahmstorf, 2002: Increasing river discharge to the Arctic Ocean. Science, 298: 2171–2173.

A. Post, D. Richardson, W. V. Tangborn, and F. L. Rosselot, 1971: Inventory of glaciers in the North Cascades, Washington. U.S. Geological Survey Professional Paper 705-A, 19 pp.

B. T. Rabus, and K. A. Echelmeyer, 1998: The mass balance of McCall Glacier, Brooks Range, Alaska, U.S.A.; its regional relevance and implications for climate change in the Arctic. Journal of Glaciology, 44(147): 333–351.

B. T. Rabus, and K. A. Echelmeyer, 2002: Increase of 10m ice temperature: climate warming or glacier thinning? Journal of Glaciology, 48(161): 279–286.

J. J. Sikorski, D. S. Kaufman, W. F. Manley, and M. Nolan, 2009: Glacial-geologic evidence for decreased precipitation during the 'Little Ice Age' in the Brooks Range, Alaska. Arctic, Antarctic, and Alpine Research, 41: 138–150, http://dx.doi.org/10.1657/15230430-41.1.138.

T. G. Van Niel, T. R. McVicar, L. Li, J. C. Gallant, and Q. Yang, 2008: The impact of SRTM and DEM image differences. Remote Sensing of Environment, 112(5): 2430–2442.

Chapter 3 Modeling the impacts of climate change on mass balance and discharge of Eklutna Glacier, Alaska, 1985-2019[2]

3.1. Abstract

Alaska's largest city, Anchorage, is critically dependent upon the melt water of Eklutna Glacier for both drinking water and hydropower generation; however, the 29 km^2 glacier is rapidly retreating. We used a temperature index model to reconstruct the glacier's mass balance for the period 1985-2019 and quantify the impacts of glacier change on runoff. Model calibration involved a novel combination of in-situ mass-balance measurements and observed snow lines from satellite imagery. A resulting ensemble of best fitting model parameters was used to model discharge. Eklutna Glacier experienced a significant negative trend (-0.38 m w.e. $decade^{-1}$) in annual mean surface mass balance. Mean annual cumulative melt increased by 24 % between the 1985-93 and 2011-19 time period. Additionally, the day of the year when 95 % of annual melt has occurred was eight days later in the later time period than in the earlier period, demonstrating a prolongation of the melt season. The modeled mean annual discharge increased at a rate of 0.2 m $decade^{-1}$, indicating that peak water, i.e. the year when annual discharge starts decreasing as the glacier becomes smaller, has not been reached. Four of the five highest specific discharge years have occurred since 2013. The past increases in runoff quantity and melt season length provide opportunities for water resource managers that must be balanced against future decreased runoff as the glacier continues to shrink.

[2] Submitted as Jason Geck, Regine Hock, Michael Loso, Johnse Ostman, and Roman Dial to the Journal of Glaciology "Modeling the impacts of climate change on mass balance and discharge of Eklutna Glacier, Alaska, 1985-2019"

3.2 Introduction

The mountain cryosphere provides clean drinking water and hydropower resources to an estimated 1.6 billion people living downstream of mountainous areas (Immerzeel and others, 2020). The thinning and retreating of glaciers worldwide can have an immediate socio-economic implication in addition to the longer-term glacier contribution to sea level rise (Hock and others, 2019). This is true even in Alaska, where the largest city, Anchorage, is critically dependent upon the melt water of Eklutna Glacier in the western Chugach for both drinking water (~80 % of the city's supply) and hydropower generation (10-15 % of the city's supply, Moran and Galloway, 2006). The regional area-average glacier mass balance for all the western Chugach Mountains in southcentral Alaska from 1962-2006 was -0.64 ± 0.07 m w.e. a^{-1} (Berthier and others, 2010), and geodetic mass balance of Eklutna Glacier calculated for the time periods 1957-2010 and 2010-15 was -0.52 ± 0.46 m w.e. a^{-1} and -0.74 ± 0.10 m w.e. a^{-1}, respectively (Sass and others, 2017). These results indicate a possible acceleration in mass loss. Reconstructing the annual variations of Eklutna Glacier's historic mass balance and resulting glacier runoff can help anticipate and mitigate future impacts on water resources.

Here, we calibrate a temperature index model with observations from 2011-15 and then reconstruct multi-decadal mass-balance variations of Eklutna Glacier to quantify the impacts of glacier change on runoff patterns. A novel approach combining in-situ mass-balance measurements and observed snow lines from satellite imagery is applied to calibrate the model parameters and identify an ensemble of the 250 best-performing model parameter combinations. This ensemble is then used to reconstruct the glacier's mass balance and discharge over the period 1985–2019.

3.2.1 Study site

Ranging in elevation from 600 to 1,700 m a.s.l., Eklutna Glacier (61.21°N, 148.98°W) is a ~29 km^2 glacier located in the Western Chugach Mountains of south-central Alaska (Fig. 3.1). The glacier's tongue is fed by two branches: a larger main (east) branch (~16 km^2) and a west branch (~13 km^2). Ground penetrating radar performed in 2010 indicated a mean ice thickness of 139 m with a maximum thickness of 430 m in the upper basin of the main branch (Sass, 2011). The glacier is in a transitional maritime climate. An automated weather station (AWS) in coastal Girdwood (76 m a.s.l.), 25 km south of the glacier, shows a mean annual precipitation of 1,907 mm from 1984 to 2014. Measurements from an AWS operated close to the equilibrium line altitude (ELA) on the glacier from 2009 to 2015 indicate a mean melt season (May-September) air temperature of 2.2 °C.

Eklutna Glacier has been subject to numerous research projects (Brabets, 1993 , Larquier, 2011; Sass, 2011, Sass and others., 2017). A field study conducted by the United States Geological Survey (USGS) from 1985-88 found that the annual glacier-wide mass-balance rate varied from -0.34 to 0.42 m w.e. a^{-1} (mean: -0.1 m w.e. a^{-1}) and the accumulation area ratio (AAR) ranged from 0.58 to 0.75 (mean: 0.63) (Brabets, 1993). For the hydrological years 1986-88 (years beginning 1 October), annual specific runoff at a gauging station (USGS 15277800 WF Eklutna) 3 km downstream from the glacier terminus ranged from 1.39 m to 1.47 m (mean: 1.43 m). The mean daily discharge at this gauging station for 1986-88 melt season (May-September) was 6.1 m^3 s^{-1} (Brabets, 1993). Alaska Pacific University has monitored both the glacier's mass balance and discharge since 2008 (Larquier, 2011; Sass and others, 2011). Sass and

others (2017) found winter mass balance varied from 1.4 to 2.5 m w.e. a^{-1} (mean: 1.7 m w.e. a^{-1}) and summer mass balance from -1.4 to -2.1 m w.e. a^{-1} (mean: -1.7 m w.e. a^{-1}) over 2009-15.

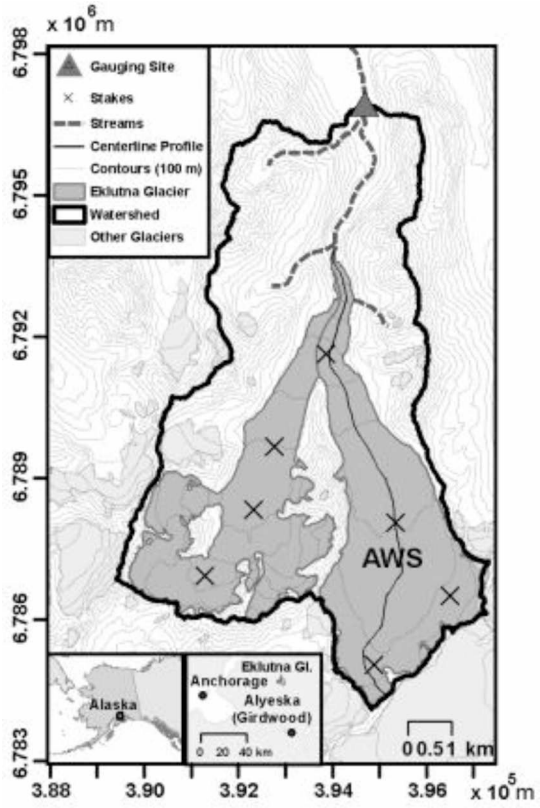

Figure 3.1: Map of Eklutna Glacier, its watershed and observation sites. The glacier area (year 2010) is shown in dark gray, while surrounding glaciers are marked in light grey. Black line depicts the glacier's watershed at the location of the discharge gauging station. Elevation contours are at 100 m intervals. Tic marks represent easting/northing (UTM 6, WGS84). Left inset shows location in Alaska. Right inset shows glacier location relative to Anchorage and Alyeska (Girdwood).

3.2.2 Data sources and use

To model Eklutna Glacier's mass balance and discharge, a digital elevation model (DEM) of the glacier and DEM derived slope, aspect and topographic shading, as well as climate datasets, were required. The model was forced with daily mean air

temperature and precipitation observations from automated weather stations (AWS). For calibration and validation, we used in-situ surface mass-balance observations (point balances) and snow line observations digitized from optical satellite imagery.

3.2.3 DEM and terrain layers

A LIDAR mission flown September 2010 with an Optech Gemini Airborne scanning system created a point cloud with a nominal post spacing of 1.9 m and a vertical accuracy of 0.3 m (Sass and others, 2017). The USGS processed the point-cloud resulting in a 2.5 m gridded DEM (OCM Partners, 2020). The DEM was used to derive surface slope, aspect, a hillshade layer, daily means of potential direct solar radiation, and to delineate a watershed boundary (ArcGIS, vers. 10.6, ESRI, 2019). The hillshade layer was used to support the digitization the 2010 glacier boundary. All layers were resampled (cubic convolution method) to a 25 m resolution for use as model input.

3.2.4 Climate and weather data

Our model relies on two different meteorological sources for temperature and precipitation: a shorter (2011-19) melt-season-only on-glacier record and longer year-round off-glacier records from the nearest long-term weather stations. Using observations from these multiple stations and transfer functions allowed extension of the on-glacier temperature and precipitation data series to the entire period 1984-2019 for model forcing.

Eklutna Glacier AWS: A local on-glacier AWS deployed on Eklutna Glacier near the ELA (~1,390 m a.s.l.) recorded hourly meteorological observations over the melt seasons (May-September) from 2011 to 2019. The AWS recorded air temperature at 2 m above surface (Campbell Scientific, model CS215 temperature sensor) and liquid

precipitation (Campbell Scientific, model TE525 tipping bucket precipitation sensor). We refer to these data as the "Eklutna data".

Girdwood AWS: The nearest long-term and year-round meteorological observations are from Girdwood, Alaska ~25 km south of Eklutna Glacier. We use the data from two stations as neither have both complete precipitation and air temperature data. An AWS located at the base of Alyeska Ski Resort in Girdwood recorded daily mean air temperature (76 m a.s.l., NOAA Cooperative Station #500243, www.wrcc.dri.edu) for the period October 1984 to 2016. A National Resource Conservation Service (NRCS) SNOTEL site also in Girdwood on Mt. Alyeska (470 m a.s.l., SNOTEL #1103, www.wcc.nrcs.usda.gov) has daily mean air temperature from 2010 to 2019. This SNOTEL site also has daily precipitation for the period October 1984 to 2019. We refer to the air temperature and precipitation data from the two sources as the "Girdwood data."

Transfer Functions: To extend the Eklutna data temperature series (2012-19) to the entire period 1984-2019, we compared the Eklutna data to the Girdwood data to build transfer functions based on the common melt seasons of each of the Girdwood stations. An air temperature sensor failure for Eklutna data prevented inclusion of the 2011 data observations. Since neither the NOAA nor the SNOTEL site cover the entire period 1984-2019, we first regressed the Eklutna data against the NOAA Cooperative Station data (n = 479 days) and applied this transfer function to the NOAA Cooperative Station data 1984-2015 (Fig. 3.2A). Next, we regressed the Eklutna temperature data the against the SNOTEL data (Fig. 3.2B) and applied this transfer function to the SNOTEL data for the melt seasons 2016-19. The SNOTEL daily precipitation data were used as

model input without any adjustments and assumed to refer to the location (elevation) of the Eklutna AWS. Instead, biases were accounted through a constant precipitation correction factor that was derived by model calibration (Section 3.2.1).

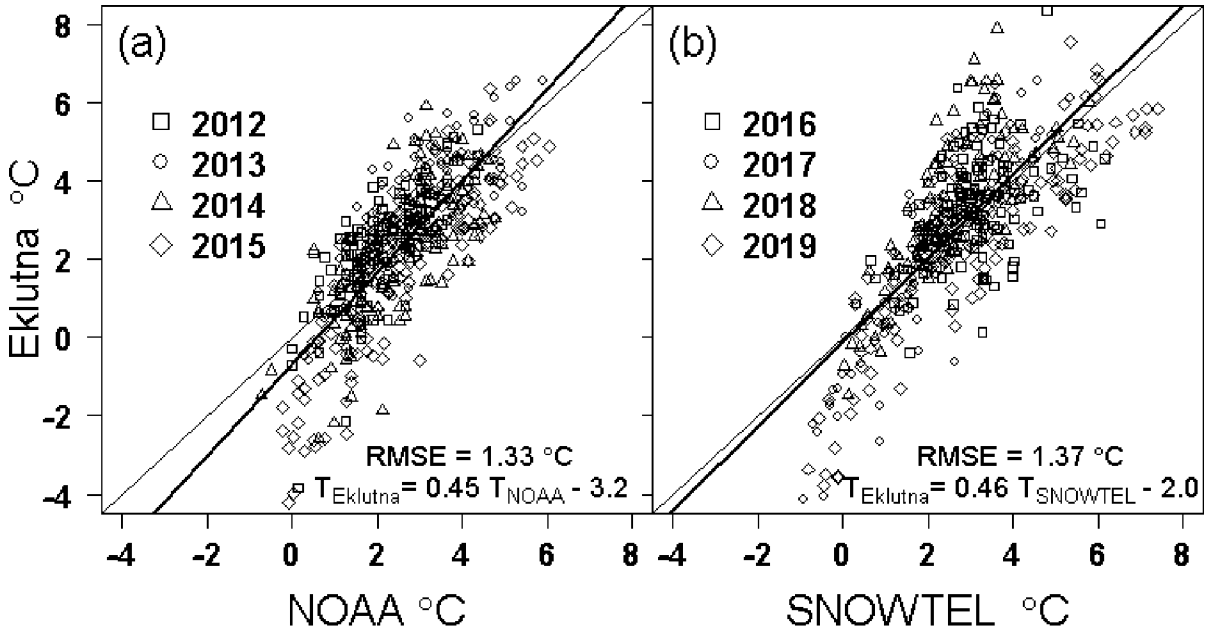

Figure 3.2: Daily mean air temperatures during the melt season (May – September) at the Eklutna AWS versus (a) the NOAA Cooperative Station (76 m a.s.l) and (b) the SNOTEL site (470 m a.s.l.) in Girdwood. Eklutna data refers to temperatures after application of transfer functions derived from correlating the measured Eklutna temperatures with the NOAA and SNOTEL temperatures for overlapping periods. Transfer functions for each data set are provided.

3.2.5 In situ point mass balances

Alaska Pacific University has maintained a glacier mass-balance monitoring program on both branches of Eklutna Glacier since 2008. Index sites and locations have evolved over the course of the program, with four to eight sites per year generally located near the glacier center line and spanning the accumulation and ablation zones of each branch (Fig. 3.1). Point mass balances were derived at each site from measured

ablations stake height, snow depth, and snow pit densities (Sass and others, 2017). The sites were visited at least twice each year. In spring, snow pits were dug to measure snow density and snow depths to calculate winter balances. Stakes were also installed in spring and measured again in fall to observe the summer balance. Seasonal mass balances thus refer to the floating (summer balance) and combined time system (winter balance, Cogley and others, 2011). For model calibration we used observations from 2011-15, a total of 18 individual index sites resulting in 36 summer/winter point balances. For validation purposes, we used observations from 2016-19 including 30 summer/winter point balances.

3.2.6 River discharge

River discharge was monitored on the West Fork of Eklutna River ~3 km downstream from the glacier terminus. The corresponding watershed is 46 % glacierized. A non-vented submersible pressure transducer (Onset Hobo, U20L) mounted to a boulder in the river recorded the stage (water level) at hourly intervals and was verified to gage datum by standard wire-weight gage on the bridge. Water pressures were adjusted to reflect atmospheric pressure variations measured concurrently at the gage site. Discharge was measured by mid-section velocity measurements using a mechanical current meter (Price AA) and sounding weight (75 C) per USGS standards (Rantz, 1982). We constructed a stage-discharge relationship from 23 observations over the years 2015-19 (Fig. 3.3); the relationship between stage and discharge is well established for discharge <25 $m^3 s^{-1}$. An hourly discharge time-series for the summer melt seasons was aggregated as daily averages to compare with model output.

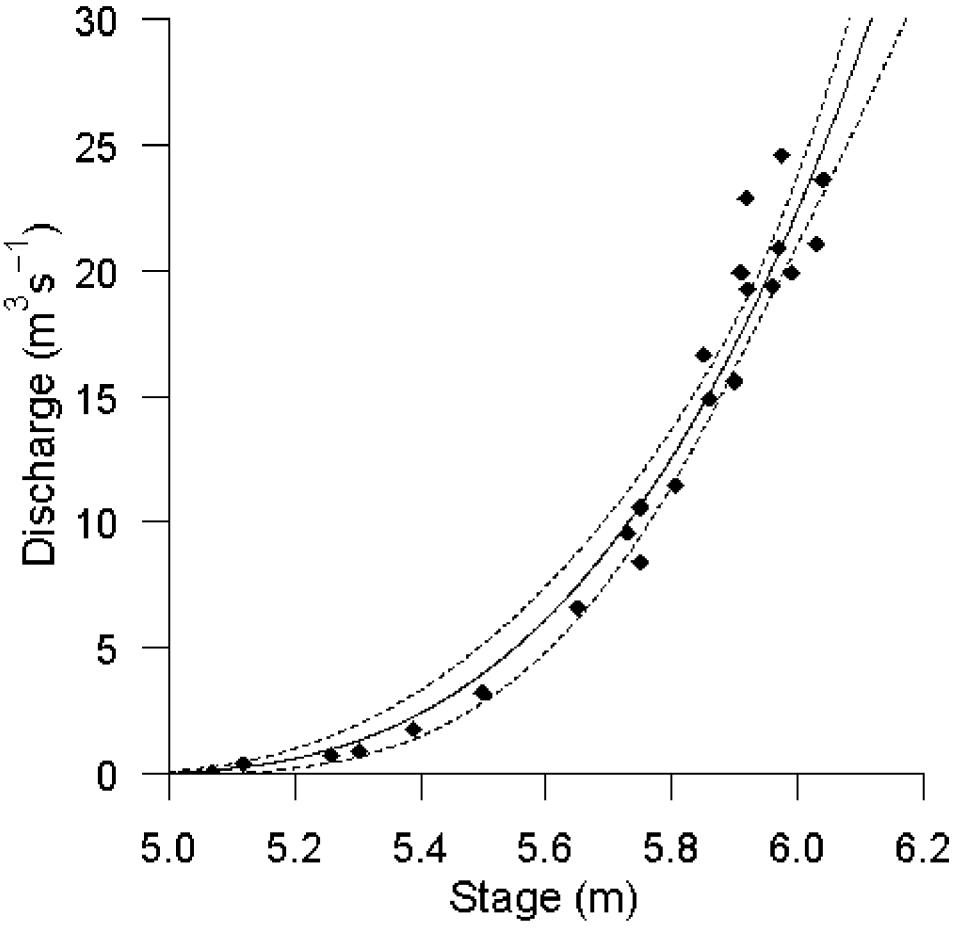

Figure 3.3: Stage-discharge rating curve constructed using 23 observations (diamonds) at the watershed's gauging station (Fig. 3.1) of the West Fork of the Eklutna River for 2015-19. Dashed lines indicates ± 1 sd.

3.2.7 Snow line position

Transient snow lines were digitized from satellite imagery over all melt seasons (June-September) between 1985 and 2015 (Table S3.1). Cloud-free satellite scenes with clearly visible snow lines were selected from LandSat 4-8 (30-60 m spatial resolution), Sentinel 2 (10 m), and SPOT (5 m) as available from USGS Earth Explorer (earthexplorer.usgs.gov). Within a GIS (ArcGIS Ver. 10.6, ESRI, 2019), a single snow

line was manually digitized (Fig. 3.1) over the glacier's two main branches for each satellite scene (n= 61 snow lines) and a centerline profile created along the main (east) branch (Fig. 3.1, Table S3.1.). We then determined the centerline distance from the high point of the centerline at the glacier head to the intersection of each snow line with the centerline. This distance is used to compare modeled results with observations (henceforth referred to as snow line position). This centerline method avoids potential border effects along glacier margins from shadows, avalanche input, and wind deposition. Because of difficulty discriminating snow from firn surfaces, we delineated snow lines only below the firn line. We assume a ± 60 m horizontal digitizing accuracy, reflecting the coarsest satellite resolution.

3.3 Mass-balance model

Model description

We used the open access Distributed Enhanced Temperature Index Model (DETIM) to recreate a 34-year (1985-2019) record of surface mass balance and discharge from Eklutna Glacier (Hock, 1999), http://regine.github.io/meltmodel). At each grid cell of the 25 m resolution DEM and at a daily timestep, DETIM models snow accumulation, melt through a temperature index method, and resulting discharge via a linear reservoir approach. Accumulation is computed from precipitation using a threshold temperature to discriminate between rain and snow. Precipitation is distributed across the glacier using a linear precipitation gradient. Melt, M (mm d^{-1}), is calculated from daily average air temperature, T (˚C), as

$$M = \begin{cases} (f_m + r_{ice/snow} \cdot I)T, T > 0 \\ 0, T \leq 0 \end{cases} \quad (2)$$

where f_m is a melt factor (mm d^{-1} °C^{-1}), $r_{ice/snow}$ (mm m^2 W^{-1} d^{-1} °C^{-1}) represents a radiation factor for snow/firn and ice surfaces, and *I* is potential clear-sky direct radiation (W m^{-2}).

The model sums melt water and rainfall over the entire watershed defined by the gauging station (i.e. including the glacier and non-glacierized areas; Fig. 3.2). It computes discharge using three linear reservoirs of firn, snow, and ice (Hock and Noetzli, 1997) and their different hydraulic properties and associated water transit velocities. The firn reservoir reflects the glacier area above a user-defined firn line; the snow reservoir is any glacier area outside the firn area with snow present at the surface; and the ice reservoir includes the bare ice area. The linear reservoir approach assumes that at any time step, *t*, the reservoir volume, *V(t),* is proportional to the reservoir discharge, *Q(t):*

$$V(t) = k_j Q(t) \quad (3)$$

with reservoir-specific storage constants, k_j (*j* = firn, snow, or ice). The units of k_j are hours, with firn at the longest temporal scale of hundreds of hours, snow at tens of hours, and ice at < 30 hours (Hock and others, 2005; Hock & Noetzli, 1997). Each reservoir's discharge is summed as a total discharge value exiting the glacier terminus. Runoff from the non-glacierized portions of the watershed are accounted for by adding melt and rainwater to the ice reservoir.

3.3.1 Model calibration

The mass-balance model was calibrated by optimizing six model parameters over the period 2011-15 including the temperature lapse rate (Y), melt factor (f_m), radiation

factors for ice (r_{ice}) and snow (r_{snow}), precipitation correction factor, (p_{cor}) and a precipitation gradient (p_{grad}). A grid search for the best-performing mass-balance parameter combinations was applied by running the model with all parameter combinations inside a prescribed parameter space of defined increments established by preliminary testing. This resulted in a total of 257,040 model runs (Fig. 3.4). Each model run covered the period 1 October 2010 to 30 September 2015 (i.e. the five mass-balance/hydrological years 2011-15).

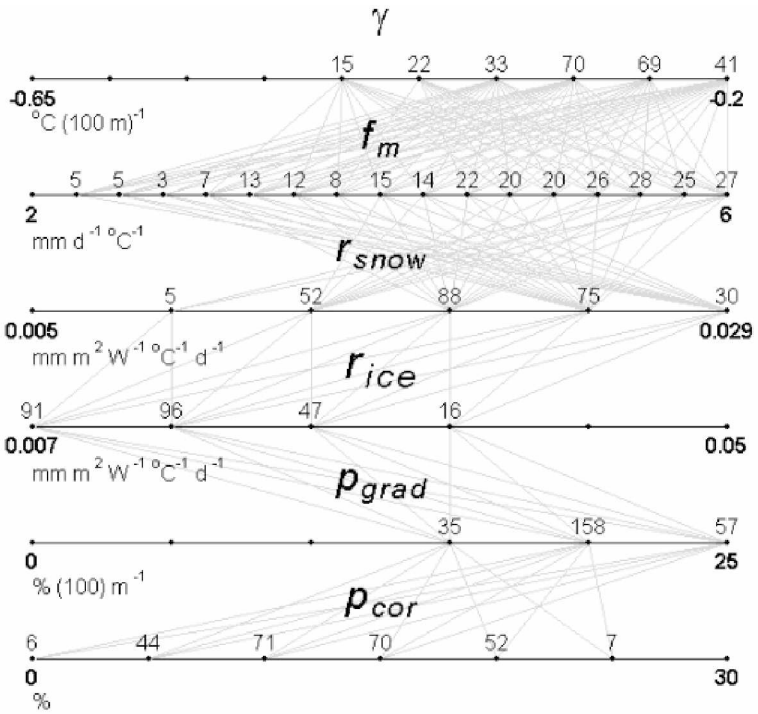

Figure 3.4: Parameter values of the 250 best-performing parameter combinations superimposed on the search parameter space. Υ is the temperature lapse rate, f_m is the melt factor, r_{snow} and r_{ice} are the radiation factors of ice and snow (Equation 1), p_{grad} is the precipitation gradient, and p_{cor} is the precipitation correction factor. Numbers on the left and right sides indicate the range of the parameter space and black dots mark the parameter values tested. Grey lines connect the parameter combinations of each of the 250 best-performing parameter sets. The values above each point reflect the number of successful combinations through a tested parameter (only show if >0).

To select the best-performing parameter combinations, we performed a multicriteria calibration by comparing the results of each DETIM run with summer/winter point balance measurements and snow line positions. A fixed date system was applied for computing winter and summer balances with 12 May marking the end of winter and 17 September the end of summer. These dates were determined from the average annual maxima and minima of modeled cumulative mass balances (daily resolution) derived from preliminary model runs. A total of 20 snow line positions obtained from satellite imagery were available during the calibration period (Table S3.1). For both variables we quantified the agreement between modeled and observed values by calculating standard z-scores as:

$$z_i = \frac{RMSE_i - \overline{RMSE}}{\sigma} \qquad (4)$$

where $RMSE_i$ is the root mean square error from the *i*th parameter set, $\overline{RMSE}$ is the mean RMSE averaged across all tested 257,040 parameter sets, and σ is the standard deviation. Hence, the z-score represents each parameter set's departure from the mean performance in standard deviations for each variable, i.e., the point balance at index sites (in m w.e.) and distance along the glacier centerline (in m) for the snow line positions. A z-score of zero indicates an "average" error; a positive z-score indicates a parameter set with greater error than average, and a negative z-score indicates a parameter set with a lower error than the average.

We found that a total of 95,096 parameter sets (~ 37 %) performed better than average for both variables. The mean z-score for these 95,096 parameters sets of stakes and snow line location were 0.74 ± 0.39 and 0.77 ± 0.43, respectively. Z-scores from these

parameter sets were then normalized to range between zero and one to allow equal weighting between the variables of different units. For each variable, the normalized z-score maximum value of one indicates the best possible agreement between modeled and observations. Since the observations have errors and the model is overparameterized it is not possible to determine a single best model run. Different parameter combinations can perform equally well in reproducing the observations. For example, overestimation of melt due to an overestimated degree-day factor can be compensated by an underestimated precipitation correction factor. Therefore, following previous studies (e.g., Truessel and others, 2015; Kienholz and others, 2017, Rounce and others, 2020) we use an ensemble of the best performing 250 for further analysis and present results in terms of ensemble mean and standard deviation.

We retained all model runs with normalized z-scores for both variables exceeding 0.84 to obtain the ensemble of 250 parameter sets for further analysis (Fig. 3.5).

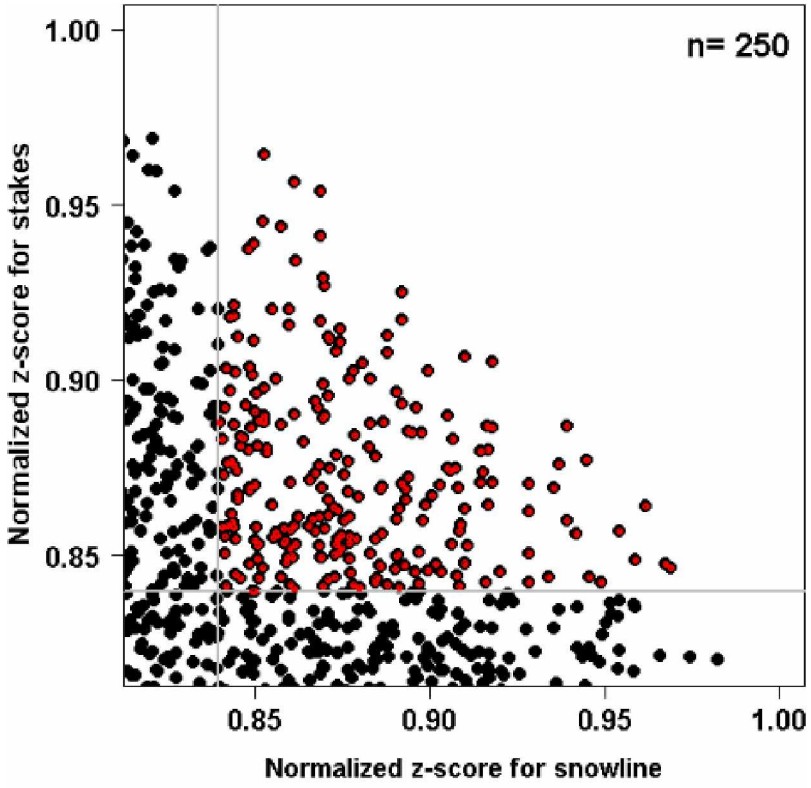

Figure 3.5: Normalized z-scores for ablation stakes versus normalized z-scores of snow line positions. Values greater that 0.84 (marked in red) for both variables corresponded to the 250 best-performing parameter sets. Grey lines mark the threshold of 0.84.

Figure 3.4 depicts parameter ranges, intervals, and frequency of the top 250 best-performing parameter sets. The temperature lapse rate among the best parameter sets ranged from -0.45 to -0.2 ˚C (100 m)$^{-1}$ with a mean of -0.29 ˚C (100 m)$^{-1}$ and a mode of -0.3 ˚C (100 m)$^{-1}$. All melt factors ranged from 2.25 to 6.00 mm d^{-1} ˚C^{-1} with the most frequent values being 5.25 and 5.50 mm d^{-1} ˚C^{-1}. The radiation factor for ice was distributed across three values between 1.2 and 1.8 m^2 W^{-1} mm h^{-1} ˚C^{-1}) while the radiation factor for snow was most frequent in the range of 0.2 and 0.4 m^2 W^{-1} mm h^{-1} ˚C^{-1}. Precipitation gradients of 20 % (100 m)$^{-1}$ and a precipitation correction factor of 10 % and 15 % dominated among the best parameter sets.

In a final step, we calibrated the three storage constants *k* (Equation 2) using the 250 best-performing sets of mass-balance parameters. The coefficient does not affect the annual amounts of discharged water but modifies the seasonality of discharge by increased (higher k-values) or decreased (lower k-values) flow speed of water through firn, snow, and ice reservoirs. The k-values were determined by varying them within established ranges (Hock and others, 2005). Tested values for k_{firn} ,k_{snow}, and k_{ice} ranged from 240 to 400 hours (20 hr interval), 30-200 hours (10 hr interval), and 5-25 hours (1 hr interval), respectively. The k-values were calibrated over 1 September 2010 to 30 August 2015 (3,402 daily discharge values). A Nash-Sutcliff model efficiency coefficient (R^2, Nash, J.E. and Sutcliffe, 1970) was calculated between modeled and observed daily discharge to assess model performance. These best-performing k-values ($k_{firn} = 300\ hrs$, $k_{snow} = 70\ hrs$, and $k_{ice} = 15\ hrs$) were then used for all model runs.

3.3.2 Model validation

We cross-validated the 250 best-performing model parameter sets using (i) snow line positions, and (ii) discharge observations over periods excluded from calibration. Modeled snow line locations were compared to observations on 41 melt season days between 1985 and 2010. There is a tendency for the model to over-predict snow cover extent early in the season and to under-predict at the end of the season. The agreement with snow line observations only could be improved by choosing different model parameter sets; however, this is expected to lead to decreased agreement between modeled and measured point mass balances. Figure S3.1 shows the distribution of r^2 values calculated from only (no snow line observations) modeled

versus observed seasonal point balances for accumulation/ablation stakes for the calibration period (2011-2015). The mean r^2 values calculated over 2011-2015 was 0.97, demonstrating the need to use snow lines. Figure 3.6 shows the agreement between the modeled and observed 41 snow line locations for the best-performing mass-balance parameter set.

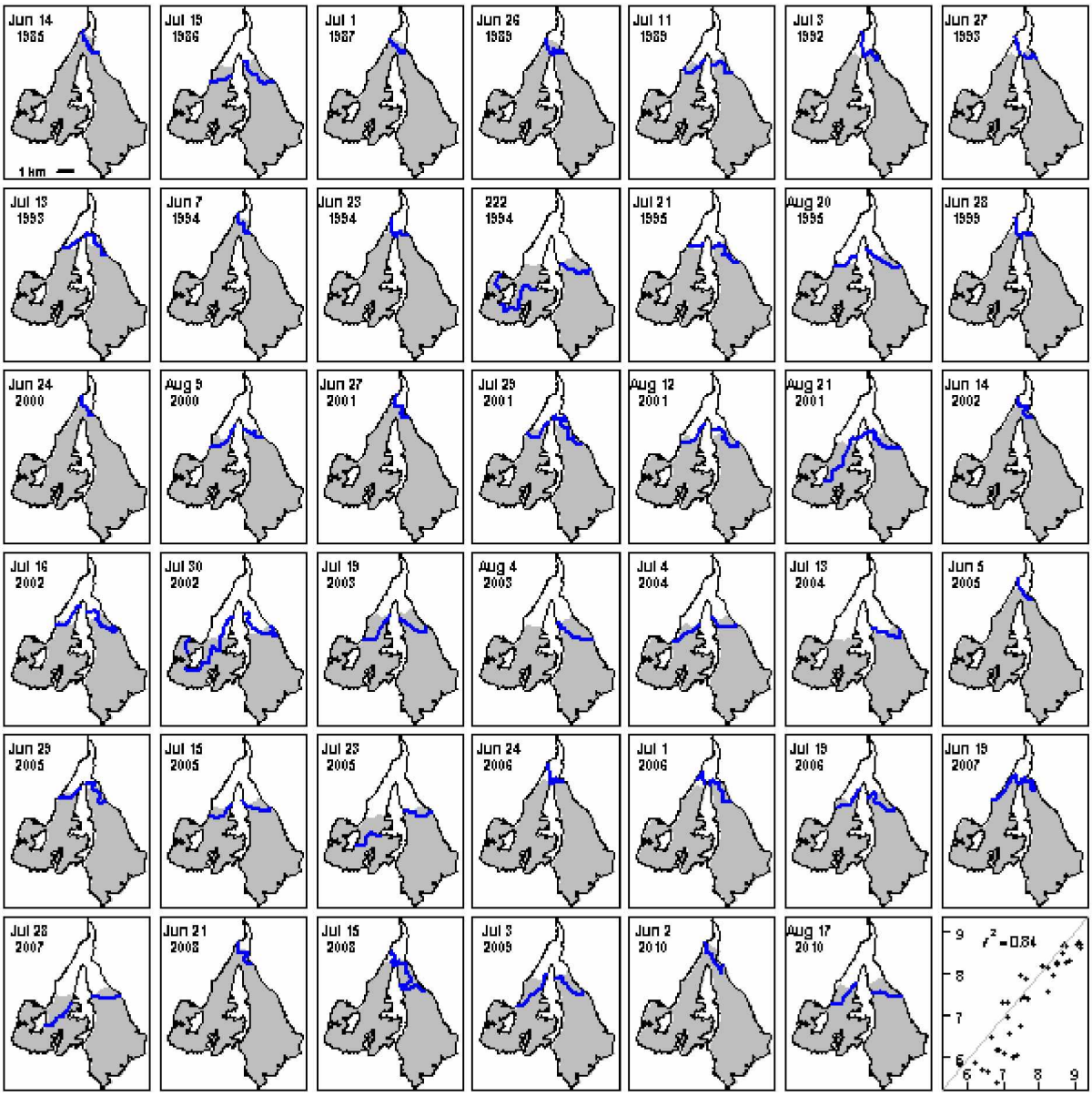

Figure 3.6: Modeled and observed snow line locations for 41 days during the melt seasons 1985-2010 for the best-performing 250 parameter combination (T = -0.2 °C (100 m)$^{-1}$, M_f,= 5.5 °C^{-1} d^{-1} , α_{ice} = 1.8 m^2 W^{-1} mm h^{-1} (°C)$^{-1}$), α_{snow} = 0.23 m^2 W^{-1} mm h^{-1} (°C)$^{-1}$), p_{cor} = 15 %, and p_{grad} = 25 % (100 m)$^{-1}$). Modeled snow-covered glacier area is shown in grey, while observed snow lines are depicted by blue line. Lower right plot depicts the 41 observed versus modeled snow line positions as measured along the centerline profile (in units of 1000 m) including the 1:1 line (grey).

Additionally, daily mean discharge was compared to observed discharge over the periods 1985-88 (Brabets, 1993) and 2016-19 (Figure 3.7). Hydrological year mean R^2 values ranged from 0.76 to 0.86 with a mean value of 0.77 from 1985 to 1988 and 0.75 to 0.87 with a mean value of 0.87 from 2016 to 2019.

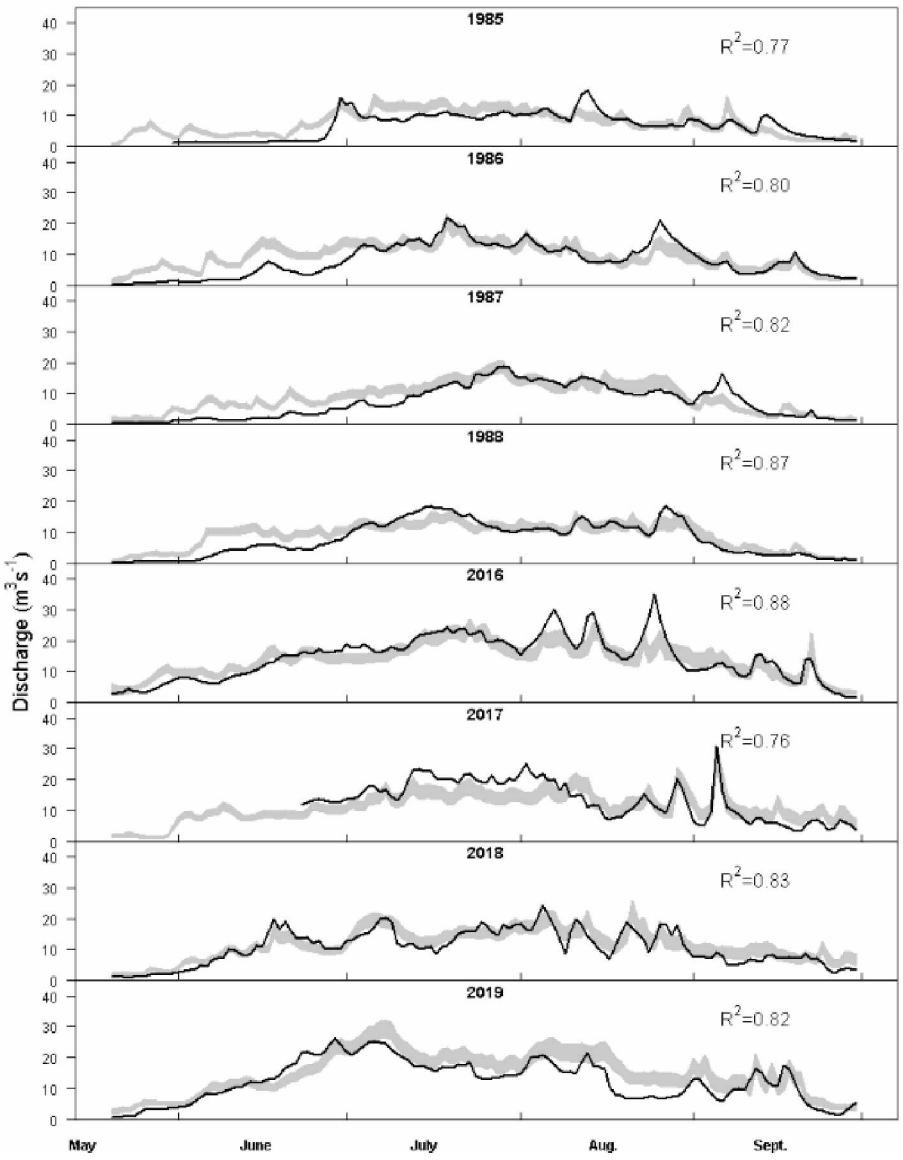

Figure 3.7: Daily mean discharge during the melt seasons for 1985-88 and 2016-19 calculated from the best 250 best performing parameter sets. The gray lines represent the range of modeled discharges with the black line representing observed discharge. Tics mark the first and last day of each month.

3.4 Results

3.4.1 Mass balance

Using the 250 best-performing mass-balance parameter sets and forcing the model with the adjusted climate observations from the Girdwood stations, we hindcast surface mass balance for the mass-balance years from 1985 to 2019 (Fig. 3.8). The annual surface mass balance averaged over the 250 parameter sets was 0.0 ± 0.1 m w.e. (± standard deviation (sd)). The maximum annual balance (1.6 m w.e.) occurred in 1988 and the minimum (-1.4 m w.e. a^{-1}) in 2004 (Fig. 3.8). Prior to 2000, simulations suggest annual surface mass balances were mostly positive, while following 2000 they were mostly negative. Annual mass balances were negative in eight of the last ten years (2009-19); the last seven were each negative.

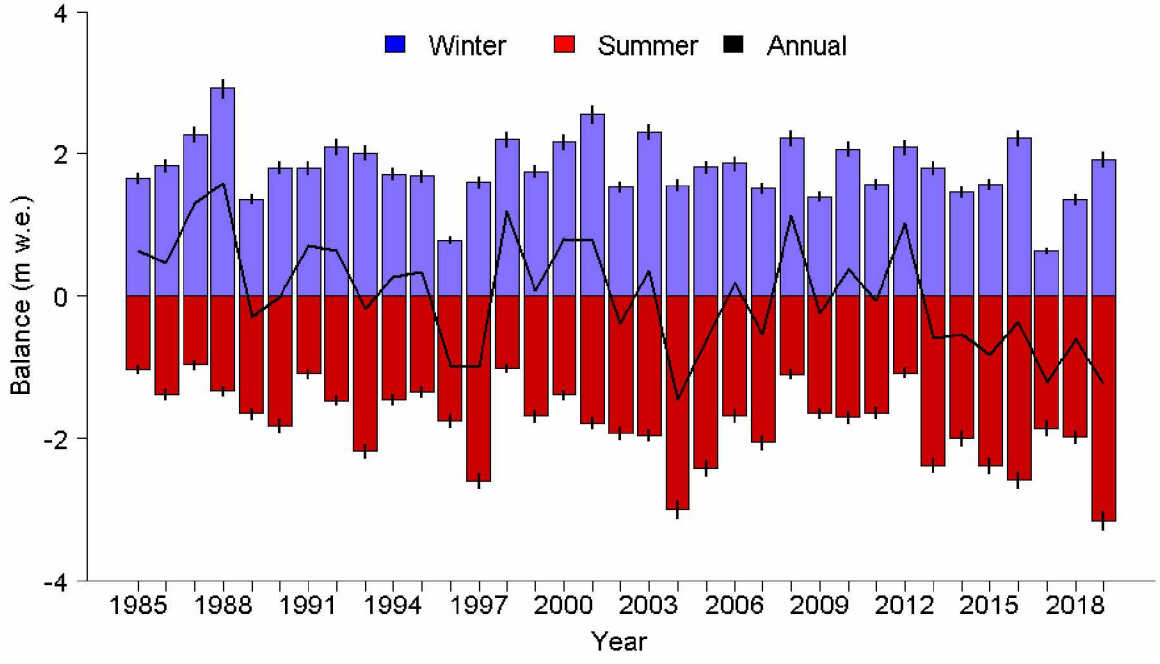

Figure 3.8: Modeled winter, summer, and annual surface mass balance (m w.e.) from 1985 to 2019. Results refer to mean values from the 250 best-performing parameter sets (± 1 sd for the winter and summer balances).

From 1985 to 2019, there is a statistically significant negative trend in annual surface mass balance (-0.38 m w.e. decade^{-1}, p = 0.002; Fig. 3.9), due mostly to a significant negative trend in summer balance (-0.28 m w. e. decade^{1}, p = 0.004). The decreasing trend in winter balance is less than half of the summer trend and not significant (-0.10 m w. e. decade^{1}, p = 0.173).

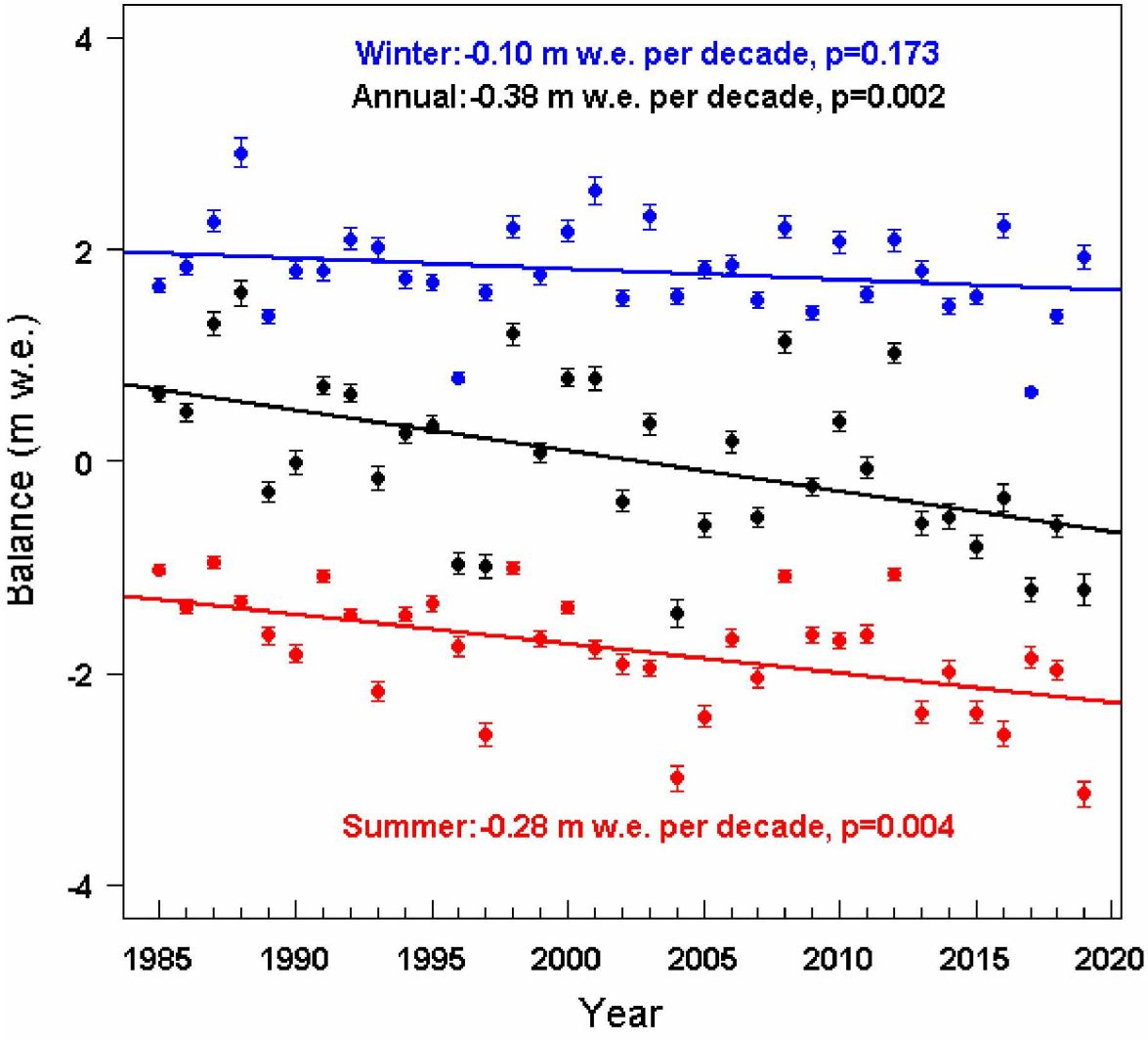

Figure 3.9: Modeled winter (blue), summer (red), and annual (black) mass balance (m w. e.) from 1985 to 2019. Dots show the mean of the 250 best-performing parameter sets (± 1 sd) and lines show the linear trends.

Modeled glacier melt increased steadily over the near-decacal periods from 1985 to 2019 (Fig. 3.10). Changes in mean annual cumulative melt over four consecutive 8 to 9-year periods (1985-93, 1994-2001, 2002-10, and 2011-19) demonstrated a 24 % increase from the earliest to latest period. In addition, the day of the year when 95 % of annual melt has occurred is eight days later in the latest period than in the earliest period, demonstrating a prolongation of the melt season. Like the near-decadal trends in annual melt, we found considerable changes over time in transient and annual accumulation area ratios (AAR), computed as the ratio of current snow-covered and total glacier area (Fig. 3.11). Annual AARs (defined by the annual AAR minima) decreased from ~70 % during the earliest period (1985-93) to ~50 % during the latest period (2011-19). Transient AARs indicate that the glacier's winter snow cover extent is depleted faster in each consecutive period.

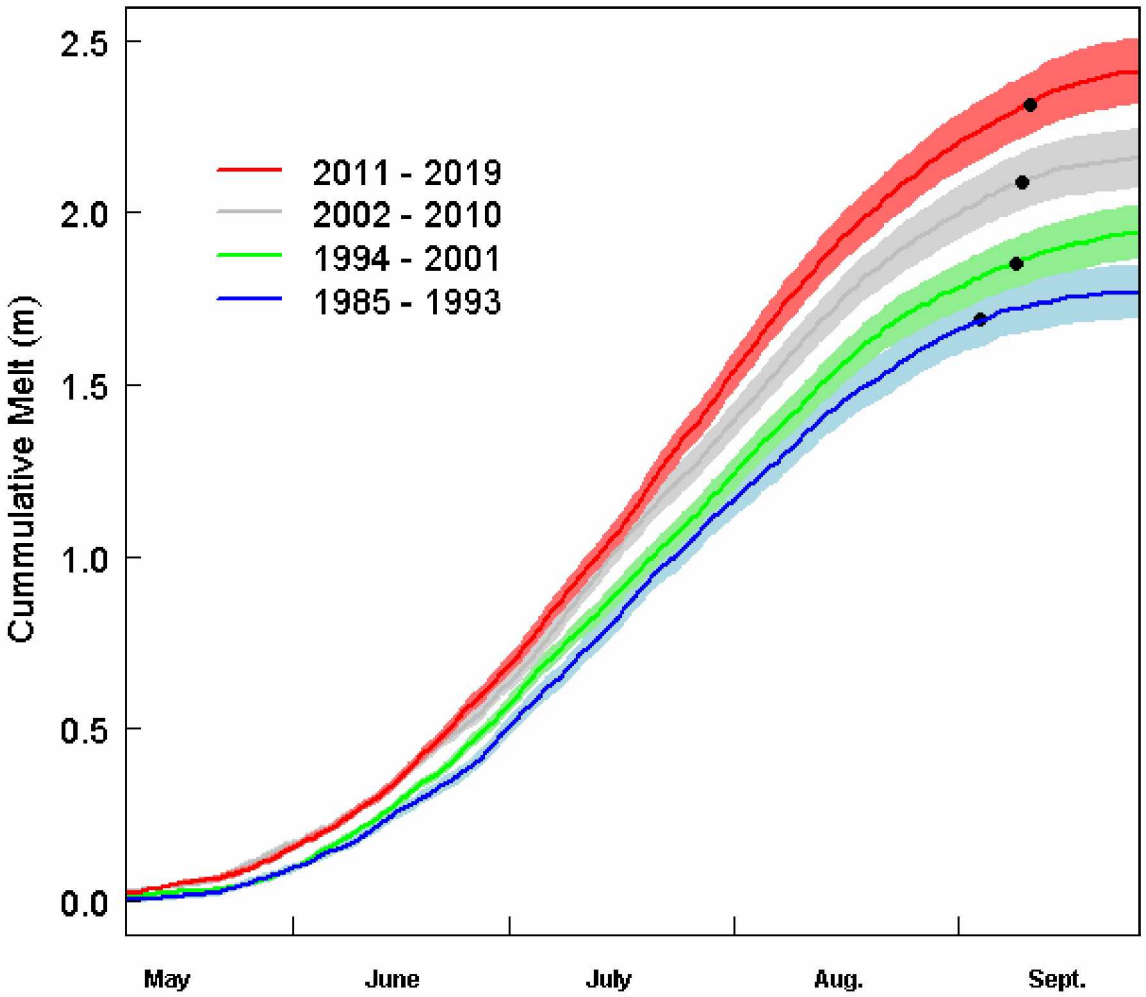

Figure 3.10: Modeled cumulative glacier melt averaged over four consecutive periods from 1985 to 2019. Lines give ensemble means and shading indicates ± 1 sd for the 250 best-performing parameter sets. Black dots indicate when 95 % of cumulative melt (hydrologic year Oct. 1 to Sept. 30) is reached. Tics mark the first and last day of each month.

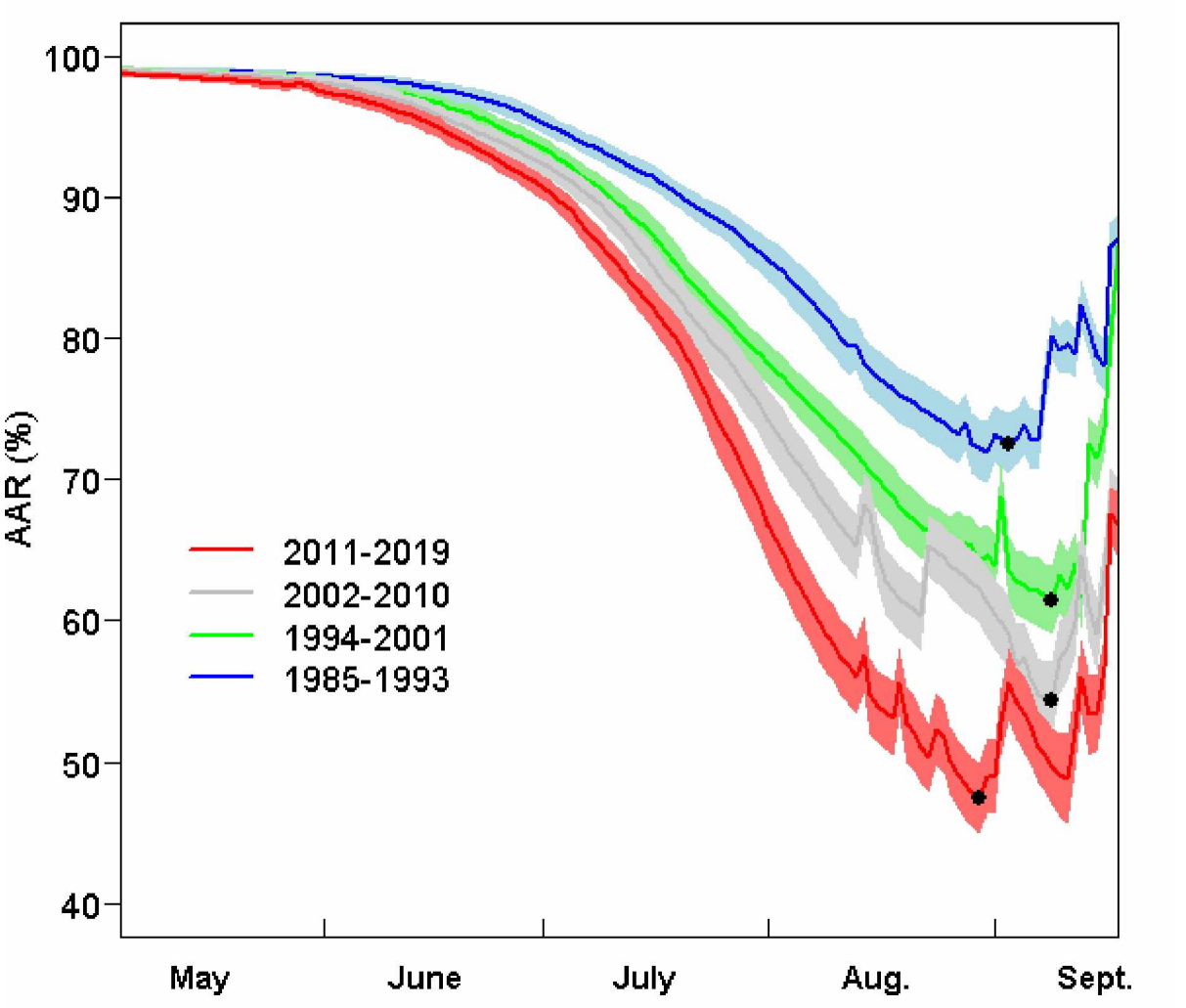

Figure 3.11: Modeled transient accumulation area ratio, AAR (%) averaged over four consecutive periods between 1985 and 2019. Lines show the ensemble mean of the 250 best-performing parameter sets and shading indicates ± 1 sd for the 250 best-performing parameter sets. Black dots depict the date and value of the annual AAR at the time of maximum snow line retreat. Tics mark the first and last day of each month.

3.4.2 Discharge

The modeled mean annual discharge (hydrological year 1 Oct.- 30 Sept.) increased from 1985 to 2019 (Fig. 3.12), a significant positive trend of 0.2 m decade^{-1} ($p = 0.001$). Overall, the mean specific annual discharge averaged over 1985- 2019 was 2.4 ± 0.37

m (± 1 sd) with the greatest modeled specific discharge most recently (3.3 m in 2019) and the lowest in the earliest year (1.4 m, 1985). Four of the five highest runoff years for model period occurred since 2013 (2013, 2014, 2016, and 2019).

Despite strong day-to-day variability due to differences in amount and timing of daily precipitation and melt, we observed a trend of increasing modeled discharge in all seasons, consistent with the above results for modeled melt (Fig. 3.13). Precipitation showed a decreasing trend and temperature an increasing one, reinforcing the notion that increasing melt dominated the discharge trend. The strongest increases in discharge occurred in the main melt season and fall.

The entire time series was used to calculate standard hydrological metrics from Fleming & Clarke (2005), including annual median daily discharge, total annual flow volume, annual maximum daily discharge, and the centroid of annual hydrograph (half the year's total flow volume). Both the median daily discharge evaluated over the melt season (May-September) and total annual flow have positive significant correlations (Median discharge = 0.776*Year -145.1; $p = 0.02$: Total annual flow = 12.7*Year -24,117; $p < 0.01$). The annual maximum daily discharge and the centroid of the annual hydrograph both showed a positive trend, though not significantly correlated (Max daily discharge = .127*Year – 229.1; $p=0.46$; Centroid DOY =0.07531*Year + 56.63; $p=0.32$).

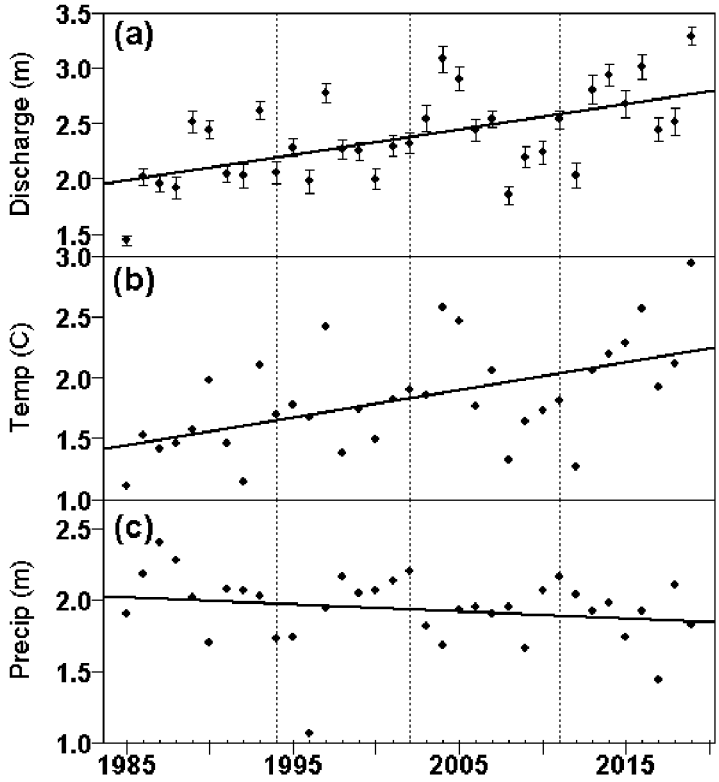

Figure 3.12: Annual specific discharge (a), mean air temperature over melt season (May – September) (b), and precipitation (c) from 1985 to 2019. Discharge refers to the modeled mean of the 250 best-performing parameter sets (± 1 sd). Temperature and precipitation refer to the data used to force the model (Section 1.6). Vertical dotted lines mark the four averaging periods used in Figures 3.10, 3.11 and 3.13.

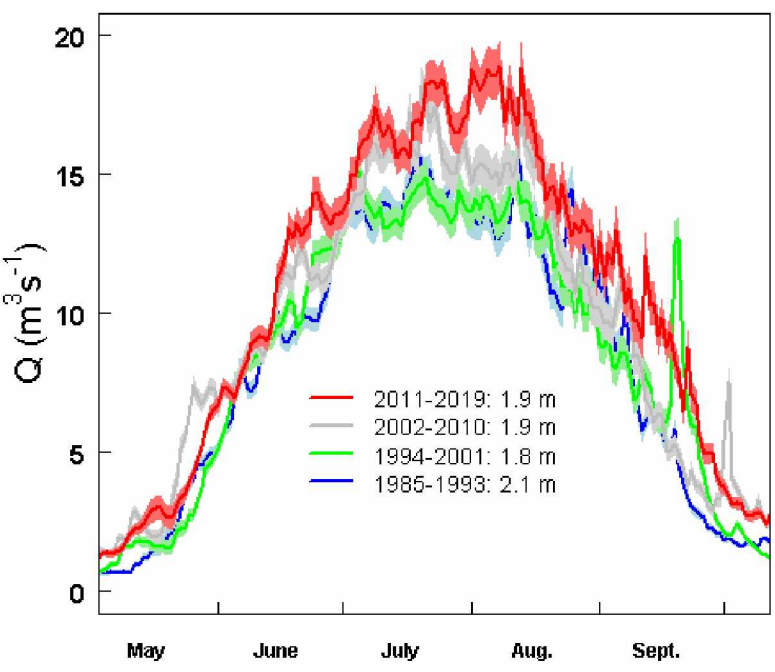

Figure 3.13: Modeled daily mean discharge ($m^3 s^{-1}$) for the 250 best-performing parameter sets. Four intervals are depicted: 1985-93, 1994-01, 2002-10, 2011-19. Mean annual precipitation for each interval shown in legend. Peaks in late fall reflect large flood events on 21 September 1995 and 3 October 2003. Tics mark the first and last day of each month.

3.5 Discussion

Overall, using an ensemble of 250 best performing models to estimate mass balance, accumulation area ratio (AAR), and discharge from 1985-2019, our implementation of DETIM shows patterns consistent with warming-induced increased melt of the Eklutna Glacier. Mass balance was mostly positive in the 1980s and negative in 2010s with the trend driven largely by a change in summer mass balance. The decadal means of AAR also showed a decrease over the period. These losses in ice and snow from Eklutna Glacier, given the decreasing trend in precipitation coupled with warming, show that the increase in discharge is due to mass wastage of the glacier.

3.5.1 Model calibration

Results from model calibration indicate the value of using multi-criteria validation that includes both point balances and snow line positions. The point balances alone were not well-constrained, as the comparison between modeled and predicted point balances found 90 % of individual parameter set model runs has an $r^2 > 0.9$ (Fig. 3.S1). This suggests that selecting the best model parameters based solely on point balances is not sufficient: many parameters sets are considered 'good fits' and so some other constraint is required. Here, we added snow line position for multi-criteria optimization. The mean RMSE snow line position among all parameter sets (n = 257,040), converted to a percentage of total centerline length, was 15 ± 7 %. Mean snow line position RMSE for the better than average 37 % (n=95,096) was reduced to 9.7 ± 3 % with a range of 4.7 % to 43.3 %. Thus, the inclusion of both variables proved necessary to provide a more robust calibration.

3.5.2 Mass balance

The modeled mean surface mass-balance rate over the period 2010-15 of -0.59 ± 0.10 m w.e. a^{-1} is slightly less negative than the mass-balance rate calculated for the same time period using the glaciological method (-0.73 ± 0.20 m w.e. a^{-1}; (Sass and others, 2017). Sass and others (2017) extrapolated the point balance measurements at three to seven locations across the glacier based on elevation dependencies to calculate the glacier-wide mass balance. DETIM uses the same point measurements but uses them, along with transient snow line positions, to constrain a model which includes terrain shading for more spatially explicit melt modeling. Additionally, Sass and others (2017) found similar agreement for their mass balance results comparing the glaciological

method to geodetic methods. Thus, our modeled mass balance results may be underestimated.

Other glaciers in Alaska with long-standing mass-balance records include the USGS benchmark glaciers Wolverine and Gulkana, which have been studied since the 1960s (O'Neel and others, 2019). Wolverine Glacier (15.6 km^2) is located within a maritime climate (Bieniek and others, 2012) on the Kenai Mountains, ~90 kilometers south of Eklutna Glacier. Gulkana Glacier (16 km^2) is in a continental climate in the eastern Alaska Range, ~ 290 kilometers northeast of Eklutna. The ensemble mean of the modeled annual mass balance for Eklutna Glacier is strongly correlated with the observed mass balance of Wolverine Glacier from 1985 to 2019 ($r = 0.83$, $p<0.001$, $n = 35$ years; Fig. 3.14) and moderately correlated to the observed mass balance of Gulkana Glacier ($r = 0.55$; $p < 0.001$, $n = 35$ years; Fig. 3.14). The lower correlation with Gulkana is expected given its distant location and different climatic setting. Eklutna and Wolverine glaciers are 90 kilometers apart and each are >35 km from the ocean. Eklutna Glacier's annual mass balances are generally greater than Wolverine's, possibly due to Eklutna's northerly versus Wolverine's southerly orientation, and the generally cooler, somewhat transitional climate of Eklutna compared to the more maritime climate of Wolverine Glacier. While both are near the ocean, Eklutna is on the lee side of the Chugach Mountains and Wolverine on the coastal side of the Kenai Mountains.

Early disagreements between Eklutna and Wolverine Glacier mass-balance results may be explained by nearby volcanic eruptions. Two specific disagreement years (1990 and 2009) coincide with Redoubt Volcano eruptions. Redoubt Volcano (~220 km away)

erupted throughout the winter of 1989/1990 and spring of 2009 and deposited substantial amounts of volcanic ash on glacier surfaces across parts of Alaska (Waythomas and Nye, 2002; Schaefer and Wallace, 2012). Spurr Volcano also deposited ash on Alaskan glacier surfaces in summer of 1992 (McGimsey and others, 2001). Such ash deposits can influence surface albedo across multiple years. DETIM as implemented here did not consider these altered surface conditions.

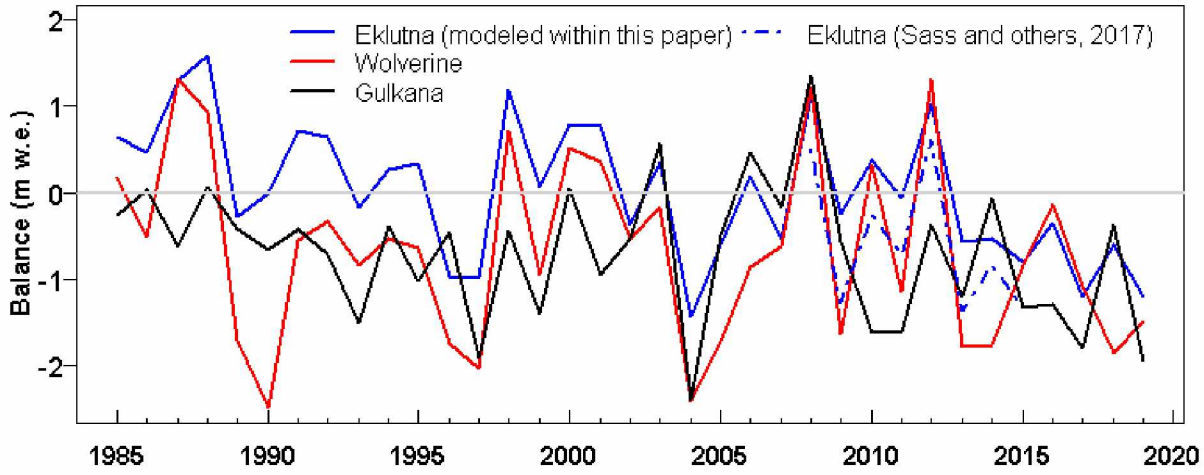

Figure 3.14: Modeled annual mass balance (m w.e.) for Eklutna, and observed balances for Wolverine, and Gulkana Glacier (O'Neel and others, 2019) over the period 1985-2019. Balances for Eklutna 2010-15 based on the glaciological method are also shown (Sass and others, 2017).

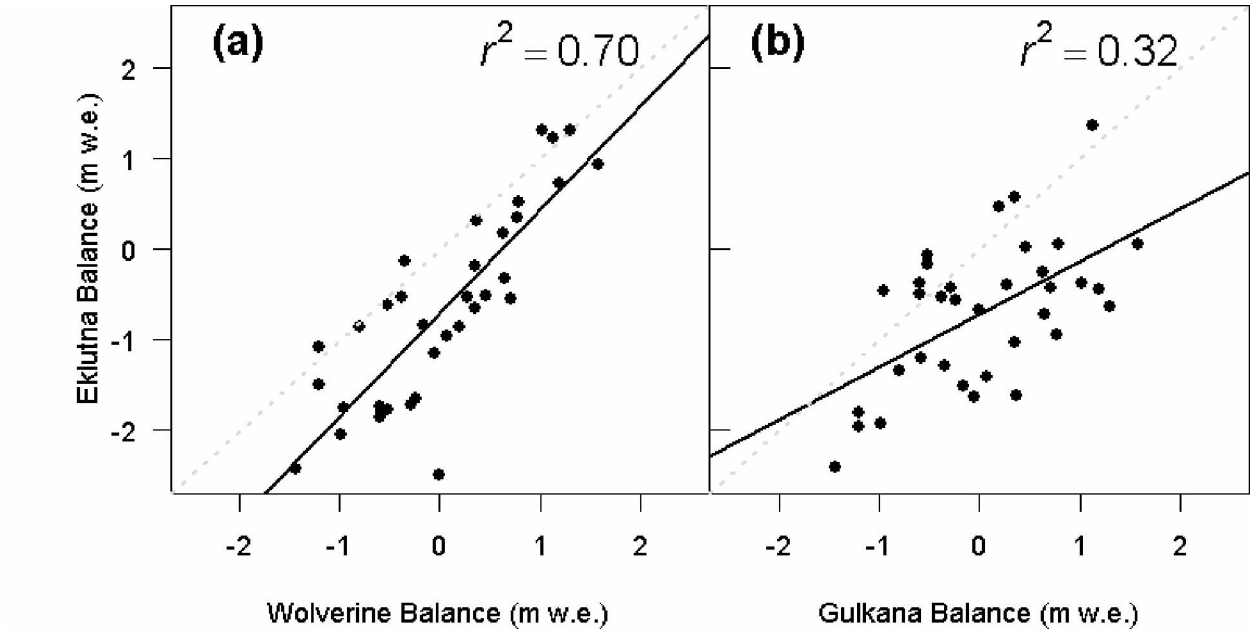

Figure 3.15: Modeled annual mass balance (m w.e.) for (a) Eklutna Glacier versus Wolverine Glacier and (b) Gulkana Glacier (right) over time period 1985-2019 (USGS, 2019). The grey dashed line depicts the 1:1 line.

3.5.3 Discharge

Modeled discharge results suggest trends of increasing annual flow and a lengthening of the discharge season (Fig. 3.12). These model observations are consistent with the observations and with other glacier discharge studies in Alaska (Beamer and others, 2016, O'Neel and others, 2015). Beamer and other (2016) found glacier volume loss contributed 760 km yr^{-1} (8 %) mean annual runoff from over the period 1980-2014. O'Neel and others (2015) found Wolverine Glacier's mass loss caused an increase in runoff. The increase in Eklutna Glacier discharge did not result from an increase in precipitation, which shows a slight decreasing trend, but rather from increased glacier melt (Fig. 3.10) coincident with increasing temperatures (Fig. 3.11). Results also show a lengthening of melt season (Fig. 3.10 and 3.13). A positive feedback may be

occurring where more melt causes less snow cover area, exposing lower albedo ice and leading to more melt. More exposed glacier ice surface also leads to a faster throughflow of water (Hock and others., 2005). Hence, one can expect increases in flood peaks, especially when coincident with heavy precipitation events (e.g., thunderstorms).

The positive trend in annual discharge indicates that the Eklutna watershed has not yet reached peak water, an interpretation consistent with model and observational studies elsewhere in Alaska (see Hock and others (2019) for summary). Valentin and others (2018) project that in Eastern Alaska's Copper River watershed (60,800 km^2) glacier discharge may peak in 2070 using the moderate emission scenario RCP 4.5. Global-scale projections indicate that peak water in Alaska will be reached later in the 21st century than elsewhere in the world (Huss and Hock, 2018).

The anticipated peak water has implications for Eklutna watershed water resources: water available for power generation and fresh water supply is increasing as more of the glacier mass is melted, but it will then decrease when, at some point, the glacier volume is diminished sufficiently that increases in melt water can no longer be sustained. The timing of peak water depends on the interaction between future climate and the evolving glacier hypsometry. Predicting this evolution is necessary for water resource managers because water usage at Eklutna Lake is typically managed over the course of the summer to reach its maximum capacity in autumn. This allows maximizing the head pressure and winter storage for hydropower production. Over winter, lake levels steadily drop as water is consumed for both drinking and power generation. If managers misjudge the length and intensity of the melt season, they risk overfilling the

lake (hence losing unused water over the spillway) or underfilling it, negatively impacting winter power generation capacity. The earlier spring melt will provide additional water in the near term; however, this will not be sustained after peak flow, when runoff will diminish with less glacier ice providing melt water. A recent study of headwater glaciers of the Columbia River found melt water contribution in August already reaching peak flow (Moore and others, 2020). Fall peak floods may disrupt optimal storage levels when the additional water spills lake storage already at its maximum. Thus, precise, real-time estimates of lake inflow will be needed for decision makers to adjust to changing conditions.

3.6 Conclusion

We have shown that multi-criteria optimization highlights the flexibility and accuracy of DETIM as a distributed, temperature-index model useful in predicting discharge based on glacier melt. DETIM offers an ability to tune model parameters that reflect glacier processes. While we found fairly good agreement between observed and predicted discharge, improvements could include variable albedos to capture the role of red-snow algae and volcanic tephra found on Eklutna Glacier (Ganey and others, 2017). DETIM's flexibility also allows the possibility to include the role of elevation dependent warming (Pepin and others, 2015) to better parameterize lapse rates. Additional modelling to include these spatial and temporal conditions may lead to better agreement with in-situ observations. The shift from positive to negative mass balance, the increase in discharge as warming summers 'mine' the glacier's stored water, and the extended melt season all have implications for water managers who seek to maximize water resources for hydropower needs as glaciers retreat and thin under a warmer climate (Hock and

Jansson, 2005). Continued monitoring of both Eklutna Glacier mass balance and discharge as model input and validation will better inform predictive models of future peak water timing.

3.7 Acknowledgements

We are grateful for funding provided by NSF ARCSS (grant #1418032), National Institute for Water Resources (#2017AK137B), NASA Alaska Space Grant and EPSCoR RID Grant. We are extremely thankful to all the students at Alaska Pacific University (APU) Glaciology and Glacier Travel field courses, other students, and faculty that have helped with glacier and river fieldwork. Special thanks to past APU graduate students Ann Marie Laquier and Louis Sass. Thanks for support from the Alaska Science Center, USGS Anchorage Office and Municipal Light and Power, and Anchorage Water and Wastewater Utility.

References

Beamer, J. P., Hill, D. F., Arendt, A., and Liston, G. E. (2016), High-resolution modeling of coastal freshwater discharge and glacier mass balance in the Gulf of Alaska watershed, *Water Resour. Res.*,(**52**) 3888– 3909, (doi:10.1002/2015WR018457)

Berthier E, Schiefer E, Clarke GKC, Menounos B and Rémy F (2010) Contribution of Alaskan glaciers to sea-level rise derived from satellite imagery. *Nat. Geosci.* **3**(2), 92–95 (doi:10.1038/ngeo737)

Bieniek PA, Bhatt US, Thoman RL, Angeloff H, Partain J, Papineau J, Fritsch F, Holloway E, Walsh JE, Daly C, Shulski M, Hufford G, Hill DF, Calos S and Gens R (2012) Climate divisions for Alaska based on objective methods. *J. Appl. Meteorol. Climatol.* **51**(7), 1276–1289 (doi:10.1175/JAMC-D-11-0168.1)

Brabets TP (1993) Glacier Runoff and Sediment Transport and Deposition Eklutna Lake Basin , Alaska. Water-Resources Investigations Report 92-4132 (doi.org:10.3133/wri924132)

Cogley, J.G., R. Hock, L.A. Rasmussen, A.A. Arendt, A. Bauder, R.J. Braithwaite, P. Jansson, G. Kaser, M. Möller LN and MZ (2011) Glossary of Glacier Mass Balance and Related Terms. *IHP-VII Tech. Doc. Hydrol.* **No. 86**(IACS Contribution No. 2,) https://wgms.ch/downloads/Cogley_etal_2011.pdf

ESRI (2019) ArcGIS Desktop: Release 10.6. Redlands, CA: Environmental Systems Research Institute.

Fleming SW and Clarke GKC (2005) Attenuation of high-frequency interannual streamflow variability by watershed glacial cover. *J. Hydraul. Eng.* **131**(7), 615–618 (doi:10.1061/(ASCE)0733-9429(2005)131:7(615))

Ganey GQ, Loso MG, Burgess AB and Dial RJ (2017) The role of microbes in snowmelt and radiative forcing on an Alaskan icefield. *Nat. Geosci.* **10**(10), 754–759 (doi:10.1038/NGEO3027)

Hock, R., G. Rasul, C. Adler, B. Cáceres, S. Gruber, Y. Hirabayashi, M. Jackson, A. Kääb, S. Kang, S. Kutuzov, Al. Milner, U. Molau, S. Morin, B. Orlove, and H. Steltzer 2019 (2019) High Mountain Areas. In: IPCC Special Report on the Ocean and Cryosphere in a Changing Climate. *Press.* **4**(vii, 973), 7–22 (doi:http://www.ipcc.ch/publications_and_data/ar4/wg2/en/spm.html)

Hock, R (1999). A distributed temperature-index ice- and snowmelt model including potential direct solar radiation. *J. Glaciol.*, **45** (149), 101-111. (doi:10.3189/S0022143000003087)

Hock R and Jansson P (2005) Modelling Glacier Hydrology. *Encyclopedia of Hydrological Sciences*, 2647–2655

Hock R, Jansson P and Braun LN (2005) Modelling the Response of Mountain Glacier Discharge to Climate Warming. (Ipcc 2001), 243–252 (doi:10.1007/1-4020-3508-x_25)

Hock R and Noetzli C (1997) Areal melt and discharge modelling of Storglaciären, Sweden. *Annals of Glaciology* **24**, 211–216 (doi:10.3189/s0260305500012192)

Huss M and Hock R (2018) Global-scale hydrological response to future glacier mass loss. *Nat. Clim. Chang.* **8**(2), 135–140 (doi:10.1038/s41558-017-0049-x)

Immerzeel WW, Lutz AF, Andrade M, Bahl A, Biemans H, Bolch T, Hyde S, Brumby S, Davies BJ, Elmore AC, Emmer A, Feng M, Fernández A, Haritashya U, Kargel JS, Koppes M, Kraaijenbrink PDA, Kulkarni A V., Mayewski PA, Nepal S, Pacheco P, Painter TH, Pellicciotti F, Rajaram H, Rupper S, Sinisalo A, Shrestha AB, Viviroli D, Wada Y, Xiao C, Yao T and Baillie JEM (2020) Importance and vulnerability of the world's water towers. *Nature* (doi:10.1038/s41586-019-1822-y)

Kienholz C, Hock R, Truffer M, Bieniek P and Lader R (2017) Mass balance evolution of black rapids glacier, Alaska, 1980–2100, and its implications for surge recurrence. *Front. Earth Sci.* **5**(July) (doi:10.3389/feart.2017.00056)

McGimsey RG, Neal CA and Riley CM (2001) Areal distribution, thickness, mass, volume, and grain size of tephra-fall deposits from the 1992 eruptions of Crater Peak vent, Mt. Spurr Volcano, Alaska. *USGS Open-File Rep. 01–370* http://pubs.er.usgs.gov

Moore RD, Pelto B, Menounos B and Hutchinson D (2020) Detecting the Effects of Sustained Glacier Wastage on Streamflow in Variably Glacierized Catchments. *Front. Earth Sci.* **8**(May) (doi:10.3389/feart.2020.00136)

Moran, E.H and Galloway DL (2006) Ground Water in the Anchorage Area , Alaska: Meeting the Challenges of Ground-Water Sustainability. (U.S. GEOLOGICAL SURVEY Fact Sheet 2006–3148), 4 https://pubs.usgs.gov/fs/2006/3148/

O'Neel S, Hood E, Bidlack AL, Fleming SW, Arimitsu ML, Arendt A, Burgess E, Sergeant CJ, Beaudreau AH, Timm K, Hayward GD, Reynolds JH and Pyare S (2015) Icefield-to-ocean linkages across the northern pacific coastal temperate rainforest ecosystem. *Bioscience* **65**(5), 499–512 (doi:10.1093/biosci/biv027)

O'Neel S, McNeil C, Sass LC, Florentine C, Baker EH, Peitzsch E, McGrath D, Fountain AG and Fagre D (2019) Reanalysis of the US Geological Survey Benchmark Glaciers: Long-term insight into climate forcing of glacier mass balance. *J. Glaciol.* **65**(253), 850–866 (doi:10.1017/jog.2019.66)

Pepin N, Bradley RS, Diaz HF, Baraer M, Caceres EB, Forsythe N, Fowler H, Greenwood G, Hashmi MZ, Liu XD, Miller JR, Ning L, Ohmura A, Palazzi E, Rangwala I, Schöner W, Severskiy I, Shahgedanova M, Wang MB, Williamson SN and Yang DQ (2015) Elevation-dependent warming in mountain regions of the world. *Nat. Clim. Chang.* **5**(5), 424–430 (doi:10.1038/nclimate2563)

Rounce, D., Hock, R., & Shean, D. (2019). Glacier Mass Change in High Mountain Asia Through 2100 Using the Open-Source Python Glacier Evolution Model (PyGEM). *Frontiers in Earth Science*. **7**. (doi: doi.org/10.3389/feart.2019.00331)

Sass LC (2011) Characterizing Eklutna Glacier's response to climate through measurements of mass balance, geometry, and motion. Alaska Pacific University.

Sass LC, Loso MG, Geck J, Thoms EE and Mcgrath D (2017) Geometry, mass balance and thinning at Eklutna Glacier, Alaska: An altitude-mass-balance feedback with implications for water resources. *J. Glaciol.* **63**(238), 343–354 (doi:10.1017/jog.2016.146)

Schaefer JR and Wallace KL (2012) Ash fall contour map of the 2009 eruption of Redoubt Volcano, Alaska: Digital shapefiles of contours and sample locations. (doi:10.14509/23463)

Trüssel, B., Truffer, M., Hock, R., Motyka, R., Huss, M., & Zhang, J. (2015). Runaway thinning of the low-elevation Yakutat Glacier, Alaska, and its sensitivity to climate change. *Journal of Glaciology,* ***61***(225), 65-75. doi:10.3189/2015JoG14J125

Valentin MM, Hogue TS and Hay LE (2018) Hydrologic regime changes in a high-latitude glacierizedwatershed under future climate conditions. *Water (Switzerland)* **10**(2) (doi:10.3390/w10020128)

Waythomas CF and Nye CJ (2002) Preliminary Volcano-Hazard Assessment for Mount Spurr Volcano , Alaska. *USGS Open-File Rep.* **01–482**, 1–39 (doi.org/10.3133/ofr01482)

Supplementary Material

Table S3.1: Satellite scenes used to obtain snow line positions over melt season (June – August) for the study period (1985-2015). Imagery date reflected year, day of year (DOY), and date image was captured, sensor is the specific satellite/sensor, and path/row reflect path/row of scene collection.

Year	Date	Sensor	Path	Row
1985	June 14, 1985	LandSat MMS	68	17
1986	July 19, 1986	LandSat MMS	68	17
1987	July 1, 1987	SPOT HRV	145	32
1989	June 26, 1989	LandSat MMS	67	17
1989	July 11, 1989	LandSat MMS	67	17
1992	July 3, 1992	LandSat MMS	68	17
1993	June 27, 1993	LandSat TM	68	17
1993	July 13, 1993	LandSat TM	68	17
1994	June 7, 1994	LandSat TM	68	17
1994	June 23, 1994	LandSat TM	68	17
1994	August 10, 1994	LandSat TM	68	17
1995	July 21, 1995	LandSat TM	67	17
1995	August 20, 1995	LandSat TM	69	17
1999	June 28, 1999	LandSat TM	69	17
2000	June 24, 2000	LandSat ETM+	69	17
2000	August 9, 2000	LandSat ETM+	69	17
2001	June 27, 2001	LandSat ETM+	69	17
2001	July 29, 2001	LandSat ETM+	69	17
2001	August 12, 2001	LandSat ETM+	69	17
2001	August 21, 2001	LandSat ETM+	69	17
2002	June 14, 2002	LandSat ETM+	69	17
2002	July 16, 2002	LandSat ETM+	69	17
2002	July 30, 2002	LandSat ETM+	69	17
2003	July 19, 2003	LandSat ETM+	67	17

Table S3.1 continued.

2003	August 4, 2003	LandSat ETM+	67	17
2004	July 4, 2004	LandSat TM	68	17
2004	July 13, 2004	LandSat TM	67	17
2005	June 5, 2005	LandSat TM	68	17
2005	June 29, 2005	LandSat ETM+	68	17
2005	July 15, 2005	LandSat ETM+	68	17
2005	July 23, 2005	LandSat TM	68	17
2006	June 24, 2006	LandSat TM	68	17
2006	July 1, 2006	LandSat TM	69	17
2006	July 19, 2006	LandSat TM	67	17
2007	June 19, 2007	LandSat ETM+	68	17
2007	July 28, 2007	LandSat ETM+	69	17
2008	June 21, 2008	LandSat ETM+	68	17
2008	July 15, 2008	LandSat TM	68	17
2009	July 3, 2009	LandSat TM	68	17
2010	June 2, 2010	LandSat ETM+	69	17
2010	August 16, 2010	LandSat ETM+	69	17
2011	June 18, 2011	LandSat ETM+	68	17
2011	June 22, 2011	LandSat TM	68	17
2011	July 7, 2011	LandSat ETM+	69	17
2012	June 22, 2012	LandSat ETM+	69	17
2012	July 27, 2012	LandSat ETM+	67	17
2012	August 15, 2012	LandSat ETM+	67	17
2012	August 28, 2012	LandSat ETM+	67	17
2013	June 17, 2013	Landsat OLI	69	17
2013	June 27, 2013	Landsat OLI	68	17
2013	July 13, 2013	Landsat OLI	68	17

Table S3.1 continued.

2013	July 29, 2013	Landsat OLI	68	17
2013	August 13, 2013	Landsat OLI	69	17
2014	June 5, 2014	Landsat OLI	69	17
2014	July 24, 2014	LandSat ETM+	68	17
2014	August 2, 2014	Landsat OLI	69	17
2015	June 17, 2015	Landsat OLI	68	17
2015	June 24, 2015	Landsat OLI	69	17
2015	July 3, 2015	Landsat OLI	68	17
2015	July 10, 2015	Landsat OLI	69	17
2015	August 4, 2015	Landsat OLI	68	17

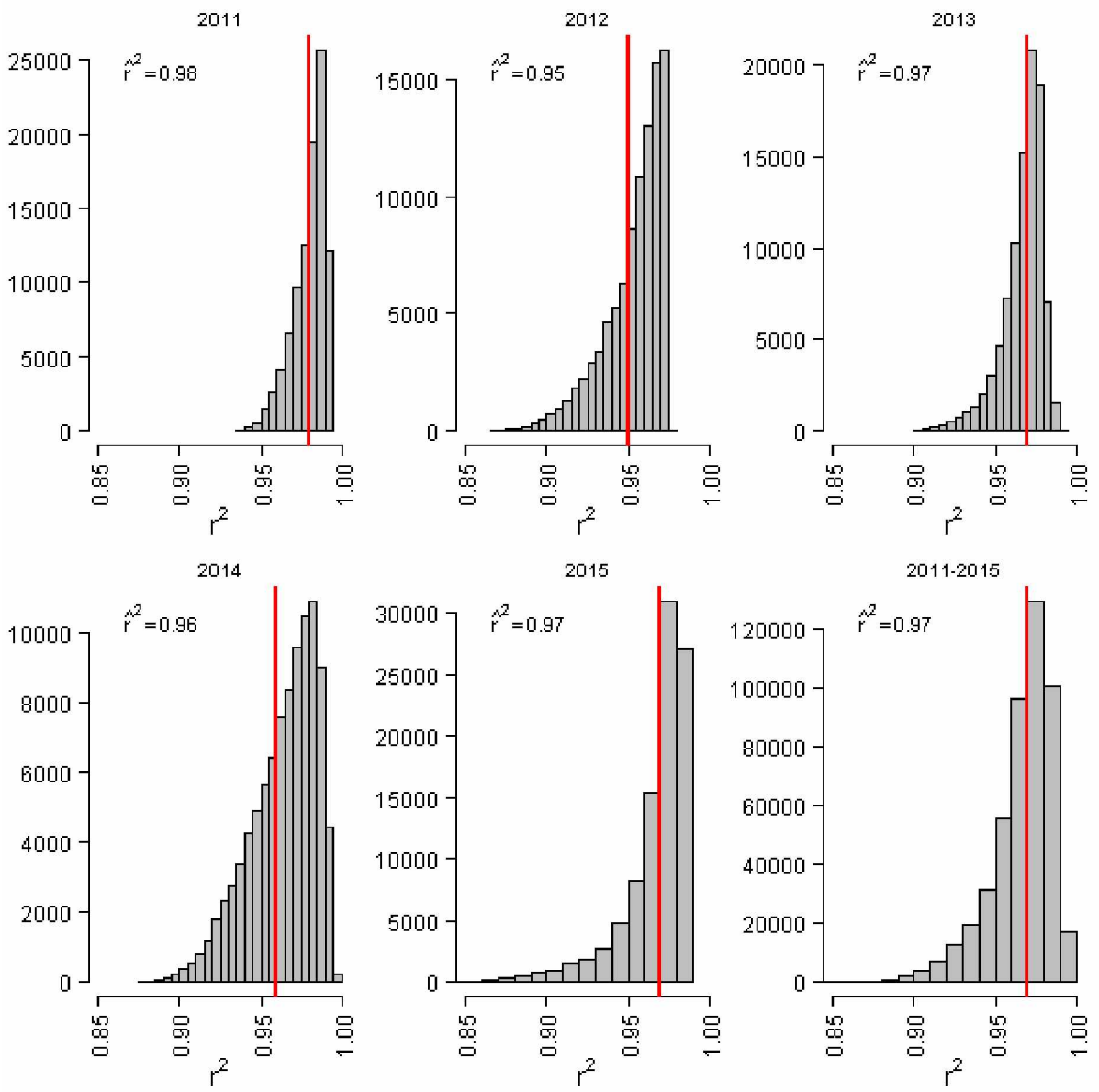

Figure S3.1: Histograms of r^2 values calculated from modeled versus observed seasonal point balances for accumulation/ablation stakes for the calibration period (2011-2015). The solid red line represents the mean r^2 value.

Chapter 4 Persistence from 1992 to 2019 of Mt. Spurr tephra deposited on glacier surfaces in the western Chugach Mountains, Alaska

4.1 Abstract

Throughout the Holocene, volcanic eruptions have repeatedly deposited volcanic ash on glaciers in Alaska, modifying surface albedo and melt. We mapped the distribution of tephra originating from the 1992 eruption of Mt. Spurr using aerial photos and satellite imagery on seven glaciers located ~180 km east of the volcano in the western Chugach Mountains in southcentral Alaska. The glaciers were completely covered by ≥ 500 g m^{-2} tephra deposits immediately after the event, deposits that are still visible on all glaciers 26 years later. Using surface reflectance, we quantified percentages of tephra glacier coverage. Results suggest an increasing tephra extent on five of the seven investigated glaciers over 2013-2018 period explained by firn line retreat which exposes previously covered deposits. The mean percent increase for all glaciers was 4% with Troublesome Glacier showing greatest increase (~ 7%) and Finch Glacier showing a slight decrease (~1%). This long-term tephra persistence on glacier surfaces most likely increased melt but by a currently unknown degree.

4.2 Introduction

The regional area-average glacier mass balance for the Chugach Mountains in southcentral Alaska from 1962-2006 was -0.64 ± 0.07 m w.e. a^{-1} (Berthier and others, 2010), well within the margin of error of the most rapid in Alaska (the Coastal Mountain region in southeast Alaska: -0.65 m w.e. a^{-1};Berthier and others, 2010). Unlike glaciers in southeast Alaska, western Chugach Mountains glaciers are subject to volcanic events depositing tephra. Worden and others (2018) show the greatest number of Alaskan tephra deposition events have occurred over the western Chugach Mountains,

with five specific events documented in the past 60 years. Tephra deposition on glacier surfaces impacts the surface energy balance by altering albedo and thereby also impacts melt and mass balance. Depending on the thickness of tephra deposition, melt may be enhanced, potentially increasing glacier mass wastage. With thicker tephra layers, glacier surfaces may be insulated, reducing melt. Field experiments have found maximum glacier melt occurs with a 1-3.5 mm layer of tephra (Dragosics and others, 2016). Recent cryosphere studies consider the role of light absorbing particles on the cryosphere, including black carbon, dust on snow events (DiMauro and others, 2015; Skiles and others, 2018), and ongoing snow and ice algal growth (Ganey and others, 2017). However, comparatively little research exists on tephra on glacier surfaces.

Visible remote sensing techniques have been widely used to map the extent of glacier debris and other light-absorbing material. Both band ratios (e.g. Landsat 7 band 3/band5, RGI Consortium, 2017) and normalized difference indices (e.g. NDSI, Selkowitz & Forster, 2016) have been applied to Landsat imagery. Scherler and others (2018) used LandSat 8 band ratios to map a 4.4 % debris coverage of glaciers globally (excluding Greenland and Antarctica). Casey & Kääb (2012) identified mineral and geochemical composition of supraglacial dust and debris using ASTER imagery (AST_07XT surface reflectance product). Their study found that supraglacial debris consisting primarily of tephra at low concentrations could be identified as visible near-infrared (VNIR) reflectance below 0.2 and short-wave infrared (SWIR) below 0.1 on Mangatoetoenui and Mangaehuehu glaciers in in New Zealand (Casey and Kääb, 2012).

Mt. Spurr located 125 km west of Anchorage, Alaska, erupted multiple times between 27 June and 17 September 1992 (Fig. 1). An 18 August event deposited 500-1000 g m^{-2} of tephra on multiple glacier surfaces in the western Chugach Mountains (Fig. 1; McGimsey and others, 2001). The aim of this study is to investigate the temporal evolution of tephra deposits at the glacier surface of seven western Chugach glaciers that were completely covered after the eruption. We map the end-of-summer extent of exposed tephra between initial deposition on 19 August 1992 and 4 September 2018 using aerial photos and satellite imagery. While multiple volcanic eruptions from other nearby volcanoes also deposited tephra on surrounding glaciers over the past five decades, we focus on the 18 August 1992 event due to size (McGimsey and others, 2001) and satellite scene availability (Fig. 2).

4.2.1 Study site

The seven investigated glaciers are located within a maritime climate of the western Chugach Mountains, Alaska, approximately 180 km east of Mt. Spurr. The glaciers range in area from 6 to 47 km^2 covering 182 km^2 (Table 4.1). Among the seven, Eklutna Glacier is well-studied, with a decade-long record of mass balance and glacier runoff (Sass and others, 2017; Larquier, 2011). Winter mass balance varied from 1.4 to 2.5 m w.e. a^{-1} (mean: 1.7 m w.e. a^{-1}) and summer mass-balance from -1.4 to -2.1 m w.e. a^{-1} (mean: -1.7 m w.e. a^{-1}) between 2009 and 2015 (Sass and others., 2017). Since 1957, Eklutna Glacier's terminus has retreated more than 2 km.

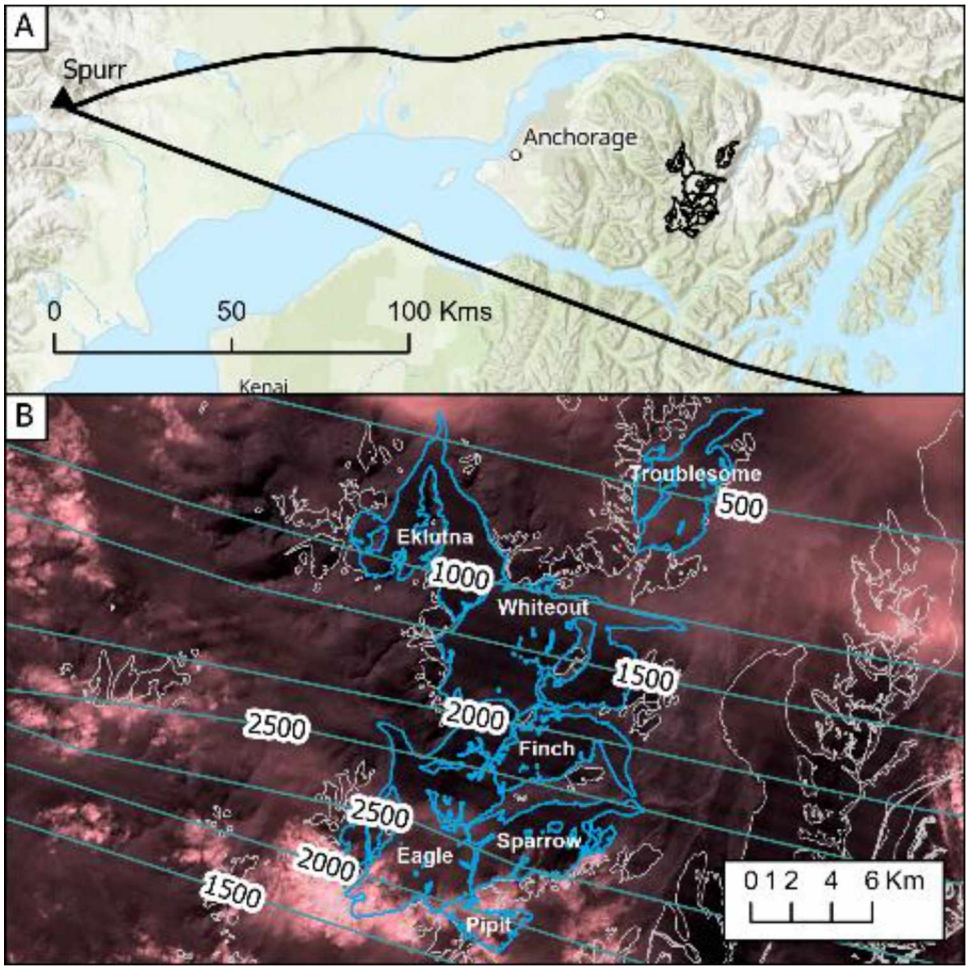

Figure 4.1: (A) Location of Mt. Spurr and study glaciers within the western Chugach Mountains, Alaska. Black line represents the 100 g m^{-2} isoline for tephra deposition following the 18 August 1992 Mt. Spurr eruption (McGimsey and others, 2001). (B) Tephra deposition isolines in g m^{-2} (Data from McGimsey and others, 2001). Blue outlines show the study glaciers. Background image is a LandSat 4 MMS false composite (bands 4, 3, 2) on the day following the eruption.

Table 4.1: General characteristics of investigated glaciers (ordered north to south). Glacier size refers to year 2009 and is based on outlines from the Global Land Ice Measurements on the Space (GLIMS) website (Randolph Glacier Inventory, V. 6.0, www.glims.org, RGI Consortium, 2017). Elevation and derived mean slope and aspect are based on Interferometric Synthetic Aperture Radar (IFSAR, http://ifsar.gina.alaska.edu).

Glacier	Mean elevation (range) (m)	Slope (deg)	Aspect
Troublesome	1,440 (606 – 2,022)	13	NE
Eklutna	1,439 (541 – 1,997)	10	N
Whiteout	1,460 (98 – 2,089)	11	NE
Eagle	1,490 (437–2,117)	10	NW
Finch	1,362 (511 – 1,982)	10	ENE
Sparrow	1,316 (379 – 2,000)	17	NE
Pipit	1,370 (809 – 1,993)	16	NE

Table 4.2: Satellite scenes and aerial imagery used to map glacier surface tephra in the late melt season over the period 1992-2019. Data were downloaded from United States Geological Survey (USGS) Earth Explorer website (earthexplorer.usgs.gov).

Year	Date	Satellite/Sensor	Path	Row
1992	18-Aug	LandSat 4 TM	69	17
1993	14-Aug	LandSat 4 TM	68	17
1994	10-Aug	LandSat 5 TM	68	17
1994	7-Sep	SPOT	--	--
1996	4-Sep	Aerial Photo	--	--

Table 4.2 continued

1999	8-Sep	LandSat 7 ETM+	68	17
2003	11-Sep	LandSat 5 TM	69	17
2004	29-Aug	LandSat 7 ETM+	68	17
2010	10-Sep	LandSat 7 ETM+	68	17
2013	15-Sep	LandSat 8 OLI	68	18
2015	28-Aug	LandSat 7 ETM+	68	
2016	29-Aug	LandSat 8 OLI	69	17
2018	4-Sep	LandSat 8 OLI	69	17
2019	8-Sep	Sentinel	06VUN	--

4.2.2 Data sources and use

Glacier outlines were downloaded from Global Land Ice Measurements on the Space (GLIMS) website (Randolph Glacier Inventory, V. 6.0, www.glims.org, RGI Consortium, 2017). The GLIMS outlines for the seven study glaciers were originally digitized from an August 2009 LandSat imagery. We updated the original 2009 outlines to reflect present-day glacier extent using an 8 September 2019 Sentinel 2 false composite scene (bands 4, 3, 2), finding an areal decrease of 4% between 2009 and 2019.

Aerial photos and cloud-free satellite scenes (Table 4.2) with clearly visible ice surfaces were selected from LandSat 4-8 (30 m spatial resolution), SPOT 5 (10 m), Sentinel 2 (10 m), and aerial imagery. LandSat Analysis Ready Datasets (ARD) were downloaded from the USGS Earth Explorer (earthexplorer.usgs.gov).

4.2 Methods

We identified exposed tephra surfaces from surface reflectance Landsat band 4 (red) scenes. Cloud-free satellite scenes with clearly visible ice surfaces were selected from atmospherically corrected products (ARD) of LandSat 8OLI+ for the years 2013, 2016, and 2018 captured near the end of melt seasons (late August to early September; Table 4.2). Suitable scenes were unavailable for other years.

To avoid mapping debris along glacier margins, a 90 m buffer inside each glacier's outline was removed from analysis within a GIS (ArcGIS Pro v 2.6, ESRI, 2020). Both medial moraines and shadow-prone areas were also excluded from analysis, reducing the glacier areas as given in Table 4.1 by 25 % (Whiteout Glacier) to 58 % (Sparrow Glacier). Tephra was then identified both through visually inspecting the darkness of glacier surfaces and through their surface reflectance values.

Individual satellite scene thresholds were established using surface reflectance pixel values identified from clearly identified tephra band on glacier surfaces. Yearly thresholds LandSat 8 band 4 (red) surface reflectance values were 2013 (0.18 – 0.27), 2016 (0.20 – 0.32), and 2018 (0.20 – 0.30). A constant threshold could not be applied to all LandSat scenes, as LandSat scenes vary in their solar zeniths causing 'darker' scenes that were thus not directly comparable to one another. Since glacier snow/ice is highly reflective, the threshold method identifies 'darker' regions within glacier boundaries. Pixels meeting these threshold criteria were quantified as a proportion of the glacier outlines, henceforth referred to as "tephra-mapping." Figure 4.2 depicts a reflectance value profile along a centerline of Eklutna Glacier. Reflectance values are lower (<0.3) in darker surface regions than on 'cleaner' ice. Once snow line is reached,

the reflectance values increase (> 0.4) as snow is highly reflective. Two to three tephra bands are visible on scenes with decreased reflectance values, demonstrating an ability for reflectance values to identify darker glacier surface regions. We assume these identify tephra, because the glaciers' medial moraines, surface debris, glacier margins, and shadows were excluded from analysis.

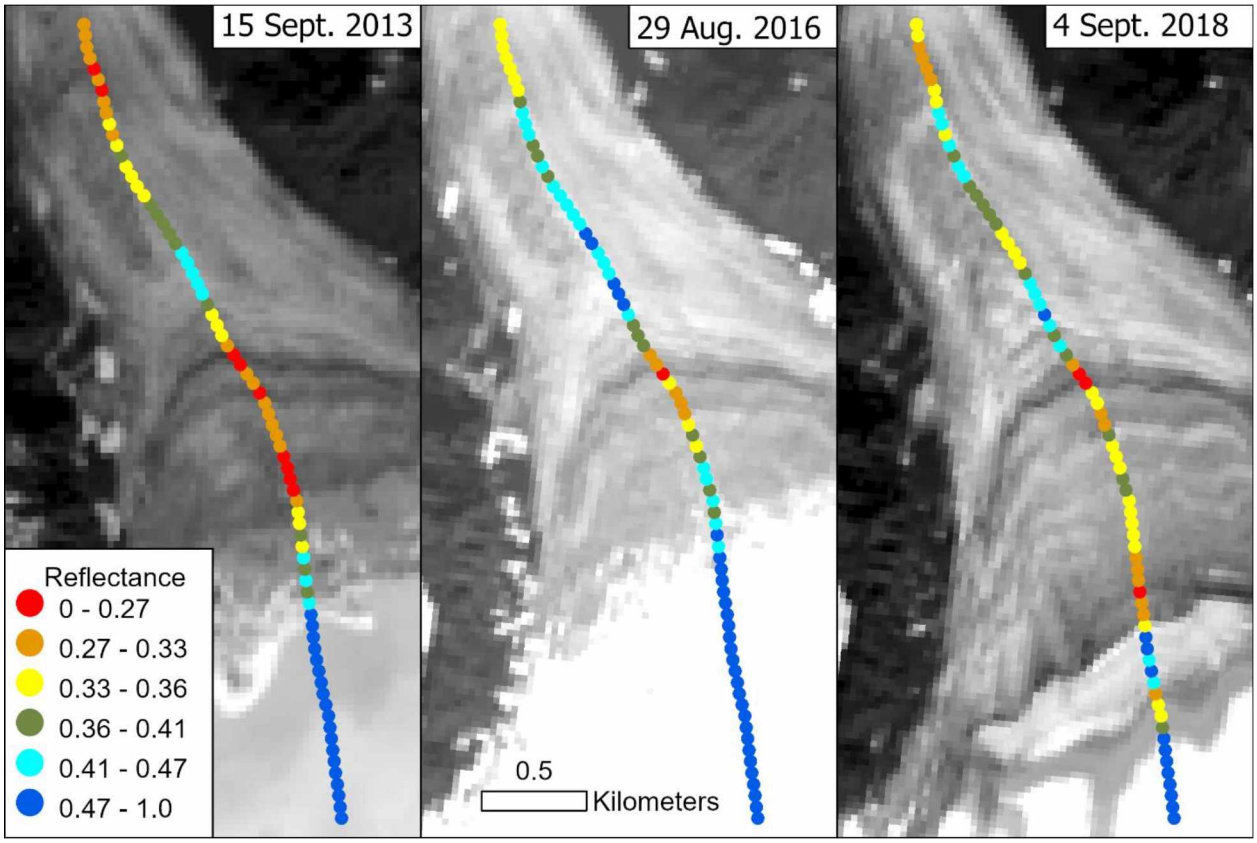

Figure 4.2: LandSat 8 Band 4 (red) scenes for 2013 (15 September), 2016 (29 August), and 2018 (4 September) depicting Eklutna Glacier surface reflectance values extracted from centerline profile.

To interpret tephra mapping results, each glacier's firn line retreat and the accumulation area ratios (AARs), i.e. the ratio of end summer accumulation area and total glacier area between 1994 and 2019, were calculated. A LandSat 5 TM (captured 10 August

1994) and Sentinel 2 satellite scene (captured 8 Sept. 2019, Table 4.2) were used to determine the firn line along each glacier's main branch.

We also focused on Eklutna Glacier by digitizing tephra from a 6 September 1996 digital ortho quad (DOQ) for comparison to late season snow lines from 1993-1996 imagery. These included a 14 July, 1993 LandSat 4 TM, a 7 September, 1994 SPOT 4 false composite (bands 3, 2, 1), a 20 August, 1995 LandSat 4 TM false composite (bands 4, 3, 2), and a digital ortho quad captured 6 September 1996. This allowed a visual comparison to explain possible mechanisms of tephra band creation.

4.3 Results

Distinct bands of tephra remain visible on the majority of investigated glaciers in 2016 and 2018, 26 years after the 1992 eruption of Mt Spurr (Fig. 4.3). Figure 4.3A shows that tephra deposition by the August 1992 Mt. Spurr appeared to completely cover the glaciers. Figure 4.1 depicts a concentration of 500-1000 g/m^2 (bands 4, 3, 2 from 19 August 1992 LandSat 4 MMS false composite image; McGimsey and others, 2001). Subsequent image scenes show tephra bands representing darker portions present near historic snow lines in 1996, 2003, 2013, and 2019. The most recent 2019 image shows up-glacier migration of tephra as it melts out from the firn line retreat.

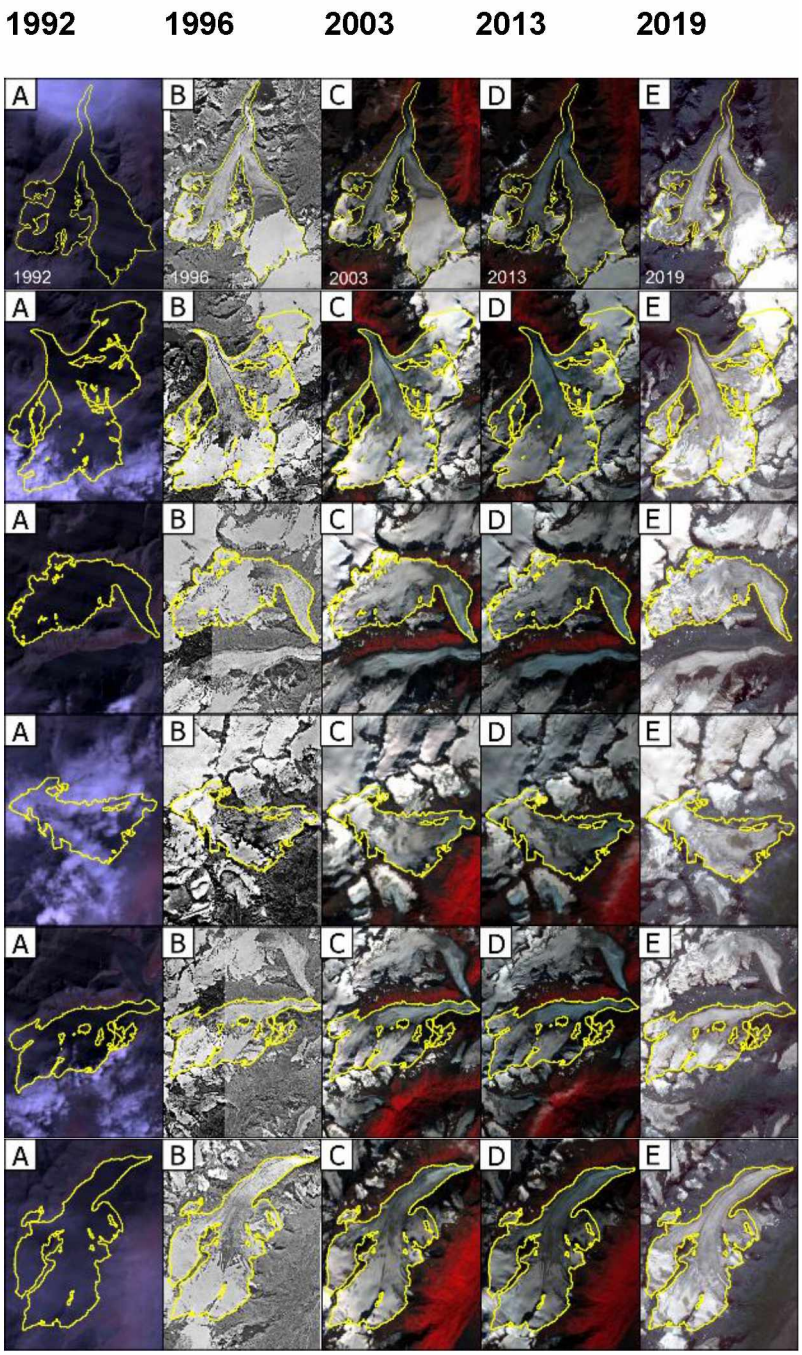

Figure 4.3: Eklutna, Eagle, Finch, Pippit, Sparrow, Troublesome, and Whiteout Glaciers depicted over multiple years: A) 19 August 1992 (one day following tephra deposition): LandSat 4 MMS false composite (bands 4, 3, 2), B) 4 September 1996: digital orthophoto quadrangle, C) LandSat 5 TM false composite (bands 4, 3, 2) captured 11 September 2003, D) LandSat 8 OLI false composite (bands 5, 4, 3) captured 15 September 2013, 2013, E) and a Sentinel 2 false composite (bands 4, 3, 2) 8 September 2019.

Table 4.3: Glacier firn line retreat distance (km) along main branch, and accumulation area ratios (AAR) for study glaciers visible with LandSat 5 TM (10 August 1994) and Sentinel 2 (10 August 2019) scenes. The last row gives mean values for investigated glaciers.

Glacier	Glacier length along centerline (km)	Firn line retreat along centerline (km)	AAR 1994	AAR 2019
Troublesome	9.9	2.7	0.69	0.35
Finch	9.6	1.2	0.77	0.45
Eagle	10.4	1.7	0.68	0.5
Pipit	4.6	1.8	0.71	0.21
Whiteout	13.5	1.6	0.69	0.69
Sparrow	10.0	0.5	0.62	0.40
Eklutna	11.0	1.6	0.68	0.43
Mean	**9.9**	**1.6**	**0.69**	**0.43**

We chose to focus on the well-studied Eklutna Glacier from 1993 to 1996. We identify five distinct tephra bands that we digitized within a GIS from a digital ortho quad (4 September 1996). The tephra band lines were visually compared to near-end-of-the-season snow lines for Eklutna Glacier during the 1993-1996 period. No late season satellite scenes were available for 1992 and 1993. A July 1993 shows snow line well below the interpreted 1993 band location. The 5 September 1994 SPOT scene depicts a late season snow line, only slightly earlier than the typical date of first snowfall (second week of September). The 1994 tephra band coincides with 1994 snow line location. The August 1995 snow line is the most down-glacier band and coincides with

the end of season snow line. Thus, tephra bands appear to concentrate near the end of season snow lines. The mean increase for all glaciers was 4 % with Troublesome Glacier showing the greatest increase (~ 7 %) and Finch Glacier showing a slight decrease (~ 1 %, Table 4.2). Figure 4.5 shows mapped tephra for three years (2013, 2016, 2018). The results of mapping across the suggested an increasing tephra extent on five of the seven study glaciers over the study period 2013-2018.

All glaciers experienced firn line retreat, averaging 1.6 km from 1994 to 2019 (Figure 4.2, Table 4.3), with individual distances ranging from 0.5 km (Sparrow) to 2.7 km (Troublesome). Each glacier AAR was also smaller in 2019, with reductions ranging from 11% (Whiteout) to 49% (Pipit), with an average of 27% across all glaciers (Table 4.3). Mapped tephra (yellow regions) depicts tephra both increasing in area and 'moving' uphill. We speculate identified tephra appearing further up glacier over time is related to firn line retreat and tephra melting out of the ELA zone of the glacier.

4.5 Discussion

Investigating tephra presence over time with satellite imagery both from a qualitative and quantitative view demonstrated tephra decadal persistence. Using ASTER imagery applied to red band surface reflectance values < 0.2, Casey & Kääb (2012) identified tephra on glacier surfaces in New Zealand using LandSat 4-8 red band imagery with a fixed threshold proved problematic over time, because scenes differed in solar zenith angles and inconsistent surface reflectance values, unsuitable for numeric mapping. Instead, use of variable thresholds proved beneficial. We did not estimate tephra mapping error. Quantifying tephra percentages is also problematic as snow obscures underlying glacier surface.

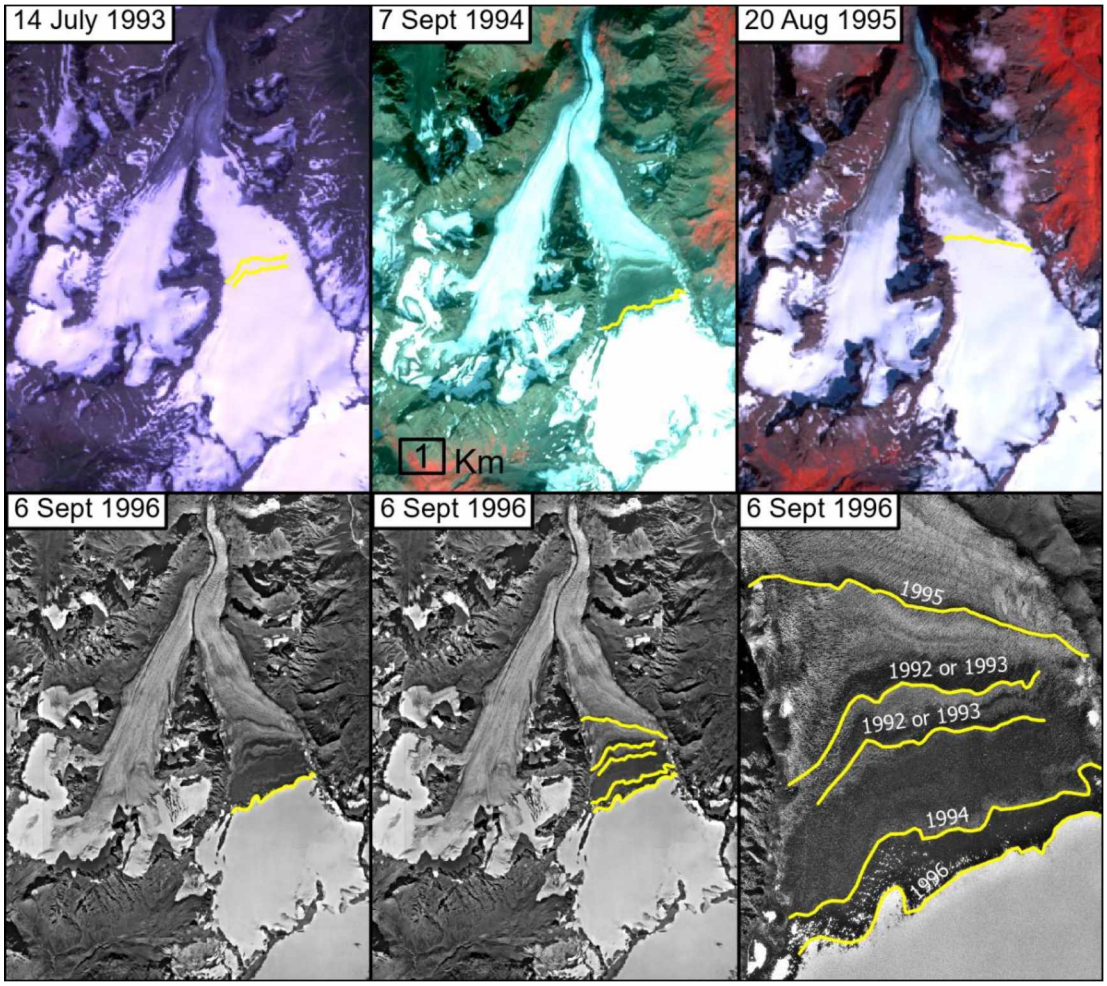

Figure 4.4: Eklutna Glacier tephra bands (yellow lines) digitized from 1996 aerial imagery superimposed on late melt season cloud-free imagery for 1993-96. Tephra bands coincide with late season snow lines (remaining snow on scenes). Satellite scenes reflect a 14 July, 1993 LandSat 4 TM false composite (bands 4, 3, 2), a 7 September, 1994 SPOT 4 false composite (bands 3, 2, 1), a 20 August, 1995 LandSat 4 TM false composite (bands 4, 3, 2), and a digital ortho quad captured 6 September 1996.

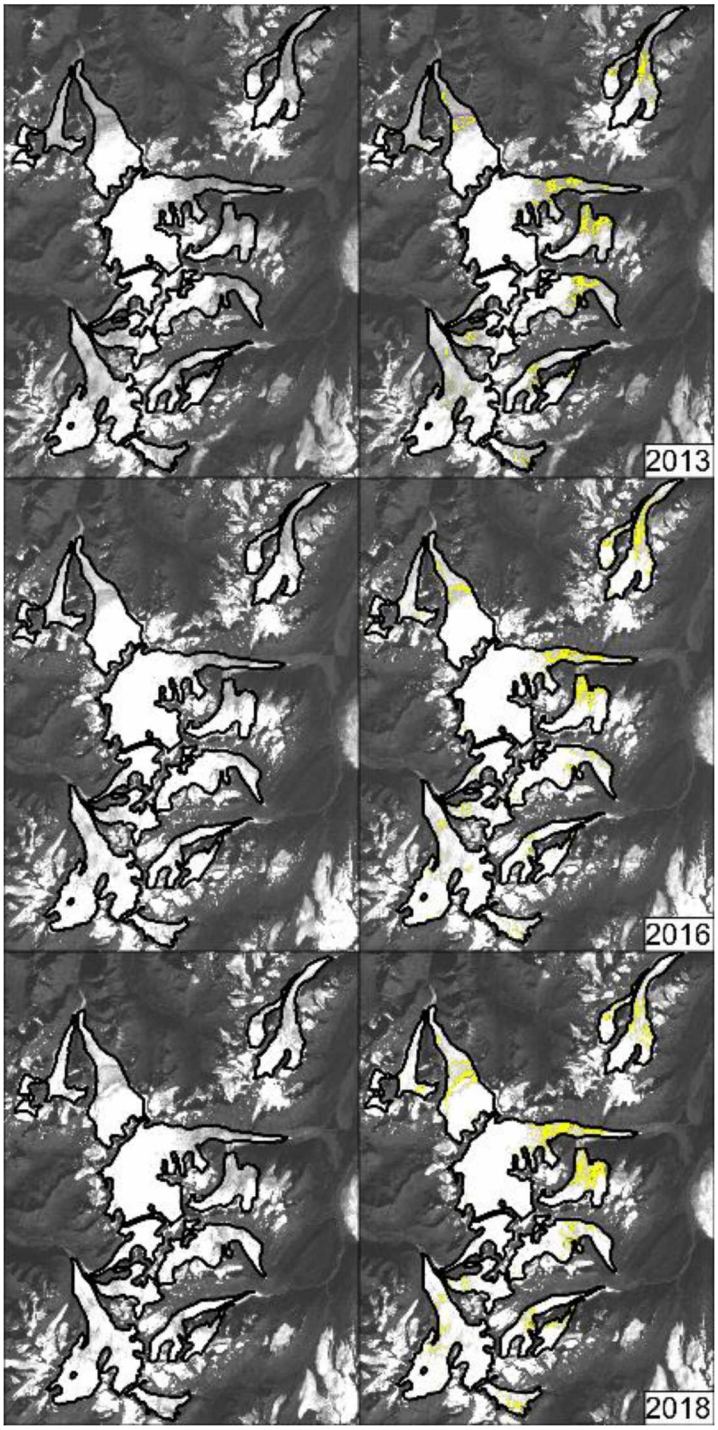

Figure 4.5: Putative tephra surfaces (yellow areas) found using threshold method on surface reflectance scenes. Image pairs show scenes with identified tephra (right) and without (left). Scenes are LandSat 8 OLI surface reflectance (visible: band 4 red) captured 15 September 2013, 29 August 2016, and 4 September 2018.

Table 4.4: Putative tephra percent coverage using threshold method on surface reflectance scenes from LandSat 8 OLI band 4 (red) for study glaciers. Values as percentages calculated by summing pixel areas within threshold bounds and dividing by reduced glacier area. Scenes captured 15 September 2013, 29 August 2016, and 4 September 2018.

Glacier	2013	2016	2018
Troublesome	14	20	21
Finch	10	6	9
Eagle	3	4	5
Pipit	6	7	12
Whiteout	8	10	13
Sparrow	8	7	12
Eklutna	5	5	9

4.5.1 Generation of Tephra Bands

Observations from satellite/aerial imagery suggest the distinct tephra bands coincide with late season snow lines (Figure 4.4). A mechanism creating these bands is presented here. We suggest that bands variation in the end-of-summer snow line generates band location. Tephra is deposited in the accumulation area, then captured within firn and trapped beneath subsequent snow/firn layers. Following multiple negative mass balance years, the firn line retreats as the firn layer thins, exposing additional tephra at the glacier surface. Insoluble in water, tephra remains surficial on the glacier near the ELA and within the ablation zone. Tephra transport may occur at the ice interface where downward melt water migration concentrates tephra before

horizontal movement impedes further motion down glacier. This results in an annual band of tephra concentrated on the newly exposed ice surface. Thus, the tephra supply is maintained and not easily removed from the system.

Surface reflectance threshold mapping (Fig 4.5) suggests an up-glacier migration and an overall percent increase in tephra over time. This may be explained by a mechanism whereby historic tephra is exposed as ice thins and firn both thins and retreats. Historic ice-embedded tephra moving down glacier melts out along with more recent deposited tephra entrapped within firn layers. Little is known about specific tephra amounts deposited prior to the 1900s. However, more recent tephra deposits (within 50 years) are most likely supplying glacier-wide tephra observations here (Fig. 4.5, Casey & Kääb, 2012; Schaefer & Wallace, 2012; Waythomas & Nye, 2002).

Tephra banding appears more clearly on some study glaciers than others. For example, Eklutna and Eagle each have clearly visible bands. Both are large, relatively flat, and are relatively crevasse-free near their historic glacier ELAs. Crevasses may serve as a drainage sink for tephra, whereby surface meltwater transports tephra into the glacier. Lliboutry (1957) explained that tephra bands on Patagonia glaciers may form at stationary firn lines. However, all study glaciers here exhibit receding firn lines since the 1990s.

4.6 Conclusion

Using both aerial/satellite imagery observations and LandSat 8 surface reflectance bands we have shown that glacier surface tephra persists for several decades after the

Mt. Spurr volcanic eruption in 1992, emphasizing the potential importance of tephra on glacier mass change. Additional melt enhancement will continue until tephra is removed by down-glacier transport and by englacial movement via surface water transport into crevasses and moulins. Further mapping efforts of volcanic tephra would extend the long-term observations of tephra coverage while melt modelling using variable surface albedos would allow a more generalized interpretation of tephra impact. Measuring in-situ tephra in combination with melt may help explain the more negative regional mass balance of western Chugach glaciers than others in Alaska.

References

Berthier E, Schiefer E, Clarke GKC, Menounos B and Rémy F (2010) Contribution of Alaskan glaciers to sea-level rise derived from satellite imagery. *Nat. Geosci.* **3**(2), 92–95 (doi:10.1038/ngeo737)

Casey K and Kääb A (2012) Estimation of supraglacial dust and debris geochemical composition via satellite reflectance and emissivity. *Remote Sens.* **4**(9), 2554–2575 (doi:10.3390/rs4092554)

Di Mauro, B., Fava, F., Ferrero, L., Garzonio, R., Baccolo, G., Delmonte, B., and Colombo, R. (2015), Mineral dust impact on snow radiative properties in the European Alps combining ground, UAV, and satellite observations. *J. Geophys. Res. Atmos.*,(**120**),6080– 6097. (doi: 10.1002/2015JD023287)

Dragosics M, Meinander O, Jónsdóttír T, Dürig T, De Leeuw G, Pálsson F, Dagsson-Waldhauserová P and Thorsteinsson T (2016) Insulation effects of Icelandic dust and volcanic ash on snow and ice. *Arab. J. Geosci.* **9**(2), 1–10 (doi:10.1007/s12517-015-2224-6)

ESRI (2020) ArcGIS Pro: Release 2.6. Redlands, CA: Environmental Systems Research Institute.

Ganey GQ, Loso MG, Burgess AB and Dial RJ (2017) The role of microbes in snowmelt and radiative forcing on an Alaskan icefield. *Nat. Geosci.* **10**(10), 754–759 (doi:10.1038/NGEO3027)

Larquier AM (2011) Differing contributions of heavily and moderately glaciated basins to water resources of the Eklutna Basin, Alaska. Masters Thesis. Alaska Pacific University.

Lliboutry L (1957) Banding and Volcanic Ash on Patagonian Glaciers. *J. Glaciol.* **3**(21), 18–25 (doi:10.3189/s0022143000024655)

McGimsey RG, Neal CA and Riley CM (2001) Areal distribution, thickness, mass, volume, and grain size of tephra-fall deposits from the 1992 eruptions of Crater Peak vent, Mt. Spurr Volcano, Alaska. *USGS Open-File Rep. 01–370* http://pubs.er.usgs.gov

Sass LC, Loso MG, Geck J, Thoms EE and Mcgrath D (2017) Geometry, mass balance and thinning at Eklutna Glacier, Alaska: An altitude-mass-balance feedback with implications for water resources. *J. Glaciol.* **63**(238), 343–354 (doi:10.1017/jog.2016.146)

Schaefer JR and Wallace KL (2012) Ash fall contour map of the 2009 eruption of Redoubt Volcano, Alaska: Digital shapefiles of contours and sample locations. (doi:10.14509/23463)

Scherler D, Wulf H and Gorelick N (2018) Global Assessment of Supraglacial Debris-Cover Extents. *Geophys. Res. Lett.* **45**(21), 11,798-11,805 (doi:10.1029/2018GL080158)

Skiles SMK, Flanner M, Cook JM, Dumont M and Painter TH (2018) Radiative forcing by light-absorbing particles in snow. *Nat. Clim. Chang.* **8**(11), 964–971 (doi:10.1038/s41558-018-0296-5)

Waythomas CF and Nye CJ (2002) Preliminary Volcano-Hazard Assessment for Mount Spurr Volcano , Alaska. *USGS Open-File Rep.* **01–482**, 1–39

Worden, A.K., Schaefer, J.R., and Mulliken KM (2018) ephra occurrence in Alaska: a map-based compilation of stratigraphic tephra data: Alaska Division of Geological & Geophysical Surveys Miscellaneous Publication 165. (doi:http://doi.org/10.14509/30059)

Chapter 5 Conclusions

This dissertation examined three glaciological topics centered on Alaska but with broader implications: 1) glacier volume change in the Brooks Range, 2) historic mass balance and runoff changes of Eklutna Glacier in the Chugach Mountains, and 3) investigation of tephra persistence on several western Chugach glaciers from a historic volcanic eruption. The main findings include:

- Central Brooks Range glaciers experienced considerable volume losses and area reduction over the period 1970/73-2001; additionally, low-elevation, elongated, and shallow sloped glaciers had more negative mass-balance rates than small, high-elevation, circular, steep glaciers.
- Eklutna Glacier in the western Chugach Mountains experienced a negative mass balance trend along with an increasing runoff trend from 1984-2019, results suggesting that peak water, i.e., the year when annual runoff amounts will start to decline, has not yet occurred.
- Volcanic tephra deposited on western Chugach glaciers from a volcanic eruption in 1992 has persisted there for multiple decades.

Chapter 2 uses digital elevation models (DEMs) that were reconstructed from historical USGS topographic maps (1970/1973) then differenced from a 2001 DEM to calculate volume changes and mean specific mass balance rates for 107 glaciers within the central Brooks Range, Alaska over the period 1970/1973 to 2001. The area-weighted mean balance rate was -0.54 ± 0.05 m w.e. a^{-1} (± uncertainty). The mass loss is consistent with observed increasing air temperatures and decreasing annual

precipitation at northern Alaska coastal weather stations during the study period. The correlation of multiple topographical indices with specific mass balance suggests that larger valley glaciers thinned more rapidly than smaller cirque glaciers, because the smaller glaciers have already retreated into topographically more sheltered sites. Proper co-registration prior to DEM differencing was found to be important for the 107 studied glaciers that are small, located in steep terrain, with a predominately northern aspect. Co-registration direction and magnitude varied largely between glaciers in the investigated domain. Since publication in 2013, new DEMs have become available from the U.S. Geological Survey (USGS) National Geospatial Program (NGP) via the Alaska Mapping Initiative (AMI). IfSAR DEMs (10 m spatial resolution) for the Central Brooks Range were captured in August 2013. Additional DEMs are available from the Polar Geospatial Center (PGC) at the University of Minnesota. These DEMs dates range from 2011 – 2017 at 2 m spatial resolution. Applying the same methods these more recent and higher spatial resolution data should be used to determine if the trend of Brooks Range glacier thinning and retreat continues. Updating glacier thinning and retreat results would identify possible increasing Arctic glacier wastage trends. The loss of Brooks Range glaciers will ultimately lead to decreased meltwater contributions to downstream rivers causing both ecological and recreational impacts.

Chapter 3 focuses on using a temperature index model, DETIM, that also includes surface albedo (Hock, 1999). Modelling results found that Eklutna Glacier experienced a substantial negative trend (-0.38 m w.e. decade^{-1}) in annual mean surface mass balance over the 1984-2019 study period. Mean annual cumulative melt increased 24% between the periods 1985-93 and 2011-19. We also found that multi-criteria

parameterization highlighted the flexibility and accuracy of DETIM as a distributed, temperature-index model useful in predicting discharge based on glacier melt. DETIM offers an ability to tune model parameters that reflect glacier processes. While we found fairly good agreement between observed and predicted discharge, improvements could include albedos that varied beyond the distinction between snow and ice to capture the role of red-snow algae and volcanic tephra common on Eklutna Glacier (Ganey and others, 2017). DETIM's flexibility also allows the possibility to include the role of elevation dependent warming (Pepin and others, 2015) to better parameterize variable and often inverted lapse rates. Additional modelling to include these spatial and temporal conditions may lead to better agreement with in-situ observations, particularly snow line and discharge. The shift from positive to negative mass balance, the increase in discharge as warming summers 'mine' the glacier's stored water, and the extended melt season all have implications for water managers who seek to maximize water resources for hydropower needs as glaciers retreat and thin under a warmer climate (Gaudard and others, 2013). Continued monitoring of both Eklutna Glacier mass balance and discharge as model input and validation will better inform predictive modeling of future peak water timing. Using future climate scenarios as model input, future peak water estimates would prove useful for Anchorage's resource managers.

Chapter 4 documents that tephra deposited during a 1992 volcanic eruption across the surfaces of seven investigated glaciers persisted for several decades. The observations were based on both aerial/satellite imagery and LandSat 8 surface reflectance bands. Our results demonstrate decadal persistence of tephra on glacier

surfaces. A thin (< 3 mm) layer of tephra enhances glacier melt and increases mass wastage (Berthier and others., 2010; Le Bris & Paul, 2015; Sass and others, 2017). Further mapping efforts of volcanic tephra would extend the long-term observations of tephra coverage while melt modelling using variable surface albedos would allow a more generalized interpretation of tephra impact. Understanding these impacts may help explain the more negative regional mass balance of western Chugach glaciers than found on other Alaskan glaciers (Berthier and others, 2010). Additionally, a better understanding of the impacts of tephra deposition on Eklutna Glacier surface melt would inform Anchorage water resource management decision as the glacier continues to thin and retreat.

This dissertation's results support observations of a continuing trend of glacier thinning and retreating due to a warming climate both in the Arctic and south-central Alaska. Continued monitoring of Eklutna Glacier's mass-balance and discharge would add to the limited number of long-term glacier monitoring programs in Alaska.

References

Berthier E, Schiefer E, Clarke GKC, Menounos B and Rémy F (2010) Contribution of Alaskan glaciers to sea-level rise derived from satellite imagery. *Nat. Geosci.* **3**(2), 92–95 (doi:10.1038/ngeo737)

Bieniek PA, Bhatt US, Thoman RL, Angeloff H, Partain J, Papineau J, Fritsch F, Holloway E, Walsh JE, Daly C, Shulski M, Hufford G, Hill DF, Calos S and Gens R (2012) Climate divisions for Alaska based on objective methods. *J. Appl. Meteorol. Climatol.* **51**(7), 1276–1289 (doi:10.1175/JAMC-D-11-0168.1)

Ganey GQ, Loso MG, Burgess AB and Dial RJ (2017) The role of microbes in snowmelt and radiative forcing on an Alaskan icefield. *Nat. Geosci.* **10**(10), 754–759 (doi:10.1038/NGEO3027)

Gaudard L, Gilli M and Romerio F (2013) Climate Change Impacts on Hydropower Management. *Water Resour. Manag.* **27**(15), 5143–5156 (doi:10.1007/s11269-013-0458-1)

Hock, R (1999). A distributed temperature-index ice- and snowmelt model including potential direct solar radiation. *J. Glaciol.*, **45** (149), 101-111. (doi:10.3189/S0022143000003087)

Pepin N, Bradley RS, Diaz HF, Baraer M, Caceres EB, Forsythe N, Fowler H, Greenwood G, Hashmi MZ, Liu XD, Miller JR, Ning L, Ohmura A, Palazzi E, Rangwala I, Schöner W, Severskiy I, Shahgedanova M, Wang MB, Williamson SN and Yang DQ (2015) Elevation-dependent warming in mountain regions of the world. *Nat. Clim. Chang.* **5**(5), 424–430 (doi:10.1038/nclimate2563)

Sass LC, Loso MG, Geck J, Thoms EE and Mcgrath D (2017) Geometry, mass balance and thinning at Eklutna Glacier, Alaska: An altitude-mass-balance feedback with implications for water resources. *J. Glaciol.* **63**(238), 343–354 (doi:10.1017/jog.2016.146)